PROTEASE ACTIVITY SENSORS FOR NONINVASIVE DIAGNOSIS AND MONITORING OF PULMONARY DISEASES

by

Jesse D. Kirkpatrick

B.S. Biological Engineering

Massachusetts Institute of Technology, 2015

SUBMITTED TO THE HARVARD-MIT DIVISION OF HEALTH SCIENCES AND TECHNOLOGY IN PARTIAL FULFILLMENT OF THE REQUIREMENTS FOR THE

DEGREE OF

DOCTOR OF PHILOSOPHY IN MEDICAL ENGINEERING AND MEDICAL PHYSICS

AT THE

MASSACHUSETTS INSTITUTE OF TECHNOLOGY

JUNE 2020

Signature of Author: _____

Harvard-MIT Division of Health Sciences and Technology

May 15, 2020

Certified by: _____

Sangeeta N. Bhatia, MD, PhD

Wilson Professor of Health Sciences and Technology &

Electrical Engineering and Computer Science, MIT

Thesis Supervisor

Accepted by: _____

Emery N. Brown, MD, PhD

Director, Harvard-MIT Program in Health Sciences and Technology

Professor of Computational Neuroscience and Health Sciences and Technology

PROTEASE ACTIVITY SENSORS FOR NONINVASIVE DIAGNOSIS AND MONITORING OF PULMONARY DISEASES

by
Jesse D. Kirkpatrick

Submitted to the Harvard-MIT Division of Health Sciences and Technology
On May 15, 2020 in Partial Fulfillment of the
Requirements for the Degree of Doctor of Philosophy in
Medical Engineering and Medical Physics

ABSTRACT

Effective disease management requires high quality and accurate information about disease state. As science and technology have evolved, the history and physical exam, once the foundations of the diagnostic workflow, have been supplemented with modalities that allow physicians to peer inside the body and acquire otherwise inaccessible information. To gain maximal information about a disease, a promising approach would be to administer a probe that can detect disease activity inside the body and emit a signal to the outside world. To this end, our group has developed "activity-based nanosensors", which detect dysregulated protease activity at the site of disease and release a reporter that can be measured in the urine. Because proteases are implicated in multiple diseases, including cancer, activity-based nanosensors have the potential to enable quantitative, noninvasive, and real-time monitoring of disease activity.

Respiratory diseases are leading causes of death and disability, owing in large part to the constant exposure of the lungs to the external environment. Though this accessibility makes the lungs vulnerable to carcinogens and pathogens, it also provides a unique diagnostic opportunity. In this thesis, we aimed to optimize activity-based nanosensors for lung disease sensing in two settings: early detection and treatment response monitoring. Finally, we sought to establish a generalizable pipeline to rationally design such tools for human disease.

We first delivered a multiplexed panel of sensors via intrapulmonary administration in two genetically engineered mouse models of lung adenocarcinoma. We found that our sensor panel diagnosed lung cancer in both models, detecting tumors as small as 2.8 mm^3 without false positives from benign lung inflammation. We then evaluated this approach in monitoring treatment response in mouse models of malignant and benign pulmonary disease. We observed dramatic treatment-induced shifts in pulmonary protease activity in both models, enabling rapid, noninvasive, and quantitative evaluation of drug response. Finally, we established a suite of *ex vivo* assays that enabled the bottom-up design of a protease-activated diagnostic probe, opening the door for translation to human disease. Collectively, this thesis provides a framework for the clinical development of activity-based nanosensors for pulmonary disease diagnosis and monitoring.

Thesis Supervisor: Sangeeta N. Bhatia, MD, PhD

Title: Wilson Professor of Health Sciences and Technology & Electrical Engineering and Computer Science

Table of Contents

ACKNOWLEDGMENTS

I have grown more during my PhD years than during any other period in my life, a direct result of the mentorship of Sangeeta Bhatia. Through your scientific guidance, you have provided me with the skills that I will need to one day become an independent investigator. Through your example, you have shown me that it is possible to achieve great success while still remaining strongly connected to core values like being kind, open, and true. And through your belief in me, you have given me the confidence to pursue highly ambitious personal and professional goals. You have been an inspiration and role model to me since I first heard of your work nine years ago, and I am grateful to have had (and to continue to have) the opportunity to learn from you.

I am indebted to the members of my thesis committee for selflessly agreeing to share their time and vast expertise to guide me along this scientific journey. Professor Lecia Sequist, you have been an incredible resource on all things clinical, helping me to understand what really matters for patients. You are the example that I will look to as I take my first steps into the medical world. Professor Richard Hynes, you have consistently pushed me to ask a question that can be daunting to a young engineer: "Why?" The biological questions that you encouraged me to pursue added a new dimension to my thesis work, and I am grateful to have benefited from your vast wealth of knowledge. Finally, thank you to Professor Daniel Anderson for chairing my committee, for encouraging me to consider the big picture, and for helping me to envision the path from bench to bedside.

I owe a huge debt of gratitude to the members of the Laboratory for Multiscale Regenerative Technology, whose collective supportiveness and positivity (in addition to its staggering brainpower) made me excited to come into work every day. First, to Jaideep Dudani, my lab "shepherd" who taught me much of what I know about how to do science. Your collaborative spirit, "just try it" mentality, and casual brilliance are qualities that I have sought to replicate since I first joined the lab and which have advanced my development as a scientist tremendously. To Andrew Warren—though we overlapped only briefly during your PhD, I was fortunate enough to continue to learn from you over Area 4 coffees, R scripts, and mass spec data spreadsheets in the years that followed. Andrew, thank you for encouraging me to take my learning into my own hands, but for always being available to give me guidance when I needed it. Thank you to Ava Soleimany for being my scientific partner throughout much of my PhD. You are a gifted scientist, a skilled communicator, and driven beyond belief. I continue to learn from your example every day. To Amanda Chen, we've been on this PhD journey together from the beginning, and I'm grateful to you for being my confidante and my 6 AM workout buddy. Melodi Anahtar, thank you being my musical soulmate, for late nights out in the streets of San Diego, and for always reminding me not to take life too seriously. Thank you to Carmen Martin-Alonso, for sharing my love of dance and for your consistent positivity. You've quickly become a scientific thought partner, and I'm excited to see how far your PhD years will take you. And to Susan Su, our UROP, for enriching our team with your eagerness to learn and contribute—and for making impressive progress on multiple projects in a short time. Finally, I am indebted to those in LMRT who keep the lab running as smoothly as it does. Thank you to Heather Fleming for the countless hours of manuscript edits, presentation practice, and for providing a listening ear when I needed advice. To Lian-Ee Ch'ng, for morning chats, and for keeping us all safe and well-stocked. To Sue Kangiser, for the therapeutic conversations about meditation and dance and for the desktop basketball hints

and tricks. And to Tarek Fadel, for your unbelievable optimism and positive energy. To all members of our lab family, thank you for making my PhD so special.

I have been fortunate enough to collaborate with extraordinarily talented scientists across MIT and beyond. Thank you to Peter Westcott, Tuomas Tammela, and Alex Jaeger for teaching me the ins and outs of lung cancer mouse models. To Mindy Bishop and Professor Max Shulaker, for our highly interdisciplinary collaboration, fueled by some delicious meals. And to Professor Elizabeth Henske, for introducing me to the rare disease that gave me my start as a PhD student. I am so deeply inspired by what you do.

Thank you to the mentors and advisors who have guided me along my path to becoming a card-carrying scientist. I am grateful to President Susan Hockfield, who was my freshman advisor and who has continued to help me make the right decisions for the past nine years. Thank you for helping me chart my academic trajectory by generously sharing your unparalleled perspective. Thank you also to Professor David Cohen, for providing your mentorship throughout my undergraduate years and for giving me the confidence to "take shots on goal" by boldly confronting research questions of deep personal significance. I had the privilege of engaging in a great diversity of research experiences prior to my entry into the HST program, each of which provided new insights that helped shape my perspective on science. Thank you to Professor Cynthia Levy, Professor Joseph Vacanti, Professor Maria Abreu, Professor Ram Sasisekharan, Professor Steven Freedman, Professor Chen Varol, and Professor Robert Langer.

My friends outside of the lab have enriched my PhD years by reminding me that there is more to life than achieving statistical significance. I discovered a passion for ballroom dance at the beginning of the second year of my PhD and I want to thank Anna Soong, my dance partner, for working and growing with me on this journey. Thank you to Roman Stolyarov, my first HST friend, who encouraged me to join this outstanding graduate program that has provided me with so much. I'm honored to be one half of the famed HST duo known as "Roman and Jesse". To Brandon Leshchinskiy, for Indian dinners, Sunday rounds, and thoughtful advice. To John Samuelsson and Avilash Cramer, for late-night chats at the kitchen table, Boston Burger Co, and always being on time with the rent. And to a lifelong friend, Ellery Altshuler, for childhood lemonade stands, posed action shots, and for paving the way toward our shared future careers in medicine.

To my brother Max—though we didn't manage to achieve our childhood career ambition of being "farmers in the same office", I'm grateful for our weekend visits back and forth between New York and Boston, our hours-long phone calls, and our unexpected time together in quarantine. Thank you for not being too cool to be best friends with your little bro. To my dad, Robert—thank you for showing me all that can be achieved with a strong work ethic and a drive for self-improvement. I hope to replicate this example for my own kids, one day. And to my mom, Myrna—you are my therapist, my life coach, my rock. Thank you for the endless supply of thoughtful advice, which has been my ground truth for all decisions, major and minor.

Finally, to my grandparents, who weren't here to see me graduate. Thank you for helping me to understand what really matters in life. This thesis is dedicated to you.

LIST OF FIGURES AND TABLES

CHAPTER 1. INTRODUCTION

1.1 The evolution of the diagnosis

Medical students learn that the process of diagnosis begins at first sight. How does the patient appear? Then, with the history and physical exam, ubiquitous staples of the medical workflow, a narrative begins to form and hypotheses are generated. This initial phase of the diagnostic workup, which relies primarily on external manifestations of disease, is remarkably similar to ancient practices. Greek physicians around the time of Hippocrates (c. 460 to c. 370 BC) emphasized the importance of undertaking a detailed history and physical examination *(1)*. Much like today, the history included a comprehensive review of systems—constitutional, cardiovascular, gastrointestinal, respiratory, genitourinary, among others—and symptoms were carefully recorded. The physical exam followed a similar framework used today, consisting of inspection, palpation, and auscultation (although the modern stethoscope would not be invented for another couple thousand years *(2)*).

However, even the most skilled clinician (in both ancient and modern times), would eventually reach the limits of the insights that physical examination and history-taking are able to provide. The signs and symptoms of disease can be confusing, contradictory, and nonspecific. The frustrations experienced by ancient clinicians relying exclusively on external manifestations of disease to inform diagnosis and treatment planning is exemplified by a quotation in the ancient Greek text *Prognosis*: “There is no point in seeking the name of any disease [for all] may be recognized by the same signs *(1)*.”

The development of modern diagnostic practices—from biochemical assays to colonoscopies—has revolutionized medicine. Today, the history and physical exam are but the first steps in the dynamic process of establishing a differential diagnosis, which is further refined with each piece of new information that is integrated into the clinical picture. As diagnostic

methods have become more and more sophisticated, an increasingly greater emphasis has been placed on identifying subclinical changes to an individual's health. In particular, the past several decades have seen a dramatic acceleration of efforts to 1) detect disease early and 2) predict and monitor disease progression and drug response.

The principle of medical screening is built on the notion that, for many diseases, the earlier an intervention can be administered, the better the patient will fare *(3)*. It is thought that this principle was first laid out by the British physician Horace Dobell, who, in 1861, proposed that healthy individuals should be routinely subjected to a history, physical exam, and series of laboratory tests to detect the "earliest evasive periods of defect in the physiological state *(2)*." Over time, this thinking has evolved and acquired more nuance; now, a screening test is only considered effective if it provides actionable information that will provide more benefit than cost. In cancer, the success of screening has been varied. Whereas there is little doubt that the Pap smear resulted in reduced mortality from cervical cancer *(3)*, prostate-specific antigen (PSA)-based screening for prostate cancer has been highly controversial due to the substantial risk of false positives and overdiagnosis *(4)*.

The benefits of lung cancer screening have recently been the subject of much debate. In the 1960s and 70s, multiple trials in the United States revealed no survival benefit in individuals screened with chest radiography *(5)*. However, screening of high-risk populations with low-dose computed tomography (LDCT) has recently emerged as a potentially viable strategy. In 2011, the National Lung Screening Trial (NLST) demonstrated a significant reduction in mortality in individuals screened with LDCT relative to those screened with chest radiography *(6)*. As a result, national guidelines in the US now recommend LDCT-based lung cancer screening in high-risk populations. However, the NLST also revealed that the vast majority (96%) of all detected nodules were false positives, and that many patients with benign disease subsequently underwent invasive

follow-up procedures that carry the risk of complications like pneumothorax *(6, 7)*. Additionally there are concerns that high cost and risks associated with radiation exposure may hamper a population-level implementation of such a screening approach *(5, 7, 8)*. As a result, despite its survival benefit, LDCT screening has not been widely adopted outside of the US *(9)*.

Once a diagnosis is established, existing diagnostic approaches (for both malignant and benign diseases) also often fail to accurately monitor disease progression and drug response. In lung cancer, the CT scan is the gold standard modality for assessing drug response *(10)*. However, with the exception of oncogene-addicted cancers treated with targeted therapy, response rate by CT does not reliably correlate with overall survival. This is especially problematic in patients treated with immunotherapy, who often experience a paradoxical increase in tumor size, likely due to infiltration of immune cells *(10)*. Relatedly, in lymphangioleiomyomatosis (LAM), which results in progressive lung function decline and, ultimately, lung failure, the lack of imaging or biochemical markers that correlate with overall survival has slowed drug development efforts *(11)*. Currently, assessment of drug response in LAM is performed via pulmonary function tests (PFTs), which are non-quantitative, effort-dependent, and change slowly in response to therapy. Though significant efforts have been dedicated to identifying predictive biomarkers of drug response in LAM *(12)*, no such marker exists today.

1.2 Beyond cells, proteins, and imaging: the new wave of molecular diagnostics

The limitations of existing biochemical, pathologic, and imaging tests for early detection and drug response monitoring have spurred enormous interest in identifying new diagnostic strategies. The emergence of highly sensitive nucleic acid detection modalities like polymerase chain reaction (PCR) presented one such opportunity. Elevated cell-free DNA levels were first reported in the serum of cancer patients in 1977 *(13)*. A slew of studies in the 1990s then revealed that cfDNA in

cancer patients harbored mutations that exactly matched those of the primary tumor, raising the prospect of a noninvasive "liquid biopsy" test for cancer. Since these seminal publications, researchers have sought to leverage ctDNA as a diagnostic and predictive biomarker of cancer. During the first decade of the 21st century, ctDNA emerged as a promising biomarkers to assess tumor dynamics, especially in the setting of treatment response in advanced cancers *(13)*. Foundational work from Diehl and colleagues in 2008 revealed that sequencing of patient tumors could reveal the presence of patient-specific mutations, which could then be used to generate patient-specific PCR assays for ctDNA profiling *(14)*. This study, and others like it, revealed that ctDNA could be used to assess residual disease after treatment and monitor for recurrence *(10)*.

The development of next generation sequencing raised the possibility that ctDNA might enable earlier detection of cancer. Because of the heterogeneity of cancer, early detection requires an unbiased approach that tests for large panels of cancer-specific mutations in cfDNA. Though the sensitivity of sequencing for individual mutations is lower than that of targeted methods like PCR, it provides far greater breadth of coverage *(15)*. Many studies have explored the use of both sequencing and targeted mutational profiling to enable detection of localized disease, and several companies (e.g. GRAIL, Thrive) have sprung from these efforts *(13, 15–18)*. However, the consistently suboptimal sensitivity of these methods for early-stage disease has raised grave doubts about the future of ctDNA as a screening tool. Multiple studies have revealed that the abundance of ctDNA scales with increased tumor burden and tumor stage *(19, 20)*. Furthermore, a substantial proportion of patients with stage I disease have no detectable ctDNA *(16, 20)*. Recent results from a large study sponsored by GRAIL demonstrated that the sensitivity of methylation sequencing of cfDNA was, on average, just 18% across the subset of patients with stage I cancer *(17)*. Using current sequencing strategies, it is estimated that clinically infeasible quantities of blood (~150 mL) would need to be collected in order to reliably detect stage I cancers *(20)*.

1.3 Protease activity has the potential to enable sensitive and specific diagnosis of disease

The limitations of imaging and blood biomarkers for early detection and monitoring of disease have spurred interest in developing mechanistically orthogonal diagnostic approaches. In order for a diagnostic to be effective in early detection of disease, it must be sensitive enough to detect small signals and specific enough to distinguish disease-associated signals from background. The ideal biomarker for assessing drug response would provide a rapid readout of disease dynamics and correlate with long-term outcomes. Activity-based diagnostics, which detect aberrant protease activity in disease, have emerged as a promising approach that may enable both early detection and drug response monitoring of disease *(21, 22)*.

Protease dysregulation is a hallmark of both benign and malignant disease. Liver fibrosis, for example, is characterized by an imbalance of metalloproteases and their inhibitors, which results in dysregulated matrix turnover and deposition *(23)*. Similarly, lung function decline in LAM is driven by protease-mediated alveolar destruction *(11)*. The role of protease dysregulation in cancer has long been appreciated, and recent efforts have revealed that proteases play a direct role in every hallmark of cancer *(22)*. Because proteases directly contribute to the hallmarks of cancer, measuring protease activity has the potential to enable highly specific detection of cancer. Furthermore, proteases harbor the ability to catalyze peptide cleavage events, a feature that can be leveraged to amplify their signal and thus increase the sensitivity of disease detection. Multiple groups have therefore sought to develop molecular probes that can be delivered to the site of disease, where local proteases catalyze cleavage events, yielding a change that is generally detectable by imaging *(21, 22)*.

Early examples of such probes made use of near-infrared (NIR) fluorescence imaging to visualize proteolytic activity in disease *(24, 25)*. These probes consist of quenched fluorophores

that fluoresce in the near-infrared range upon engagement with proteases at the disease site, and such probes are now in clinical development for intraoperative imaging of the tumor bed *(26)*. Activatable cell penetrating peptides (ACPPs), a related class of protease-activated imaging probes, consist of a polycationic cell penetrating peptide domain in complex with a polyanionic domain, linked together via a protease-cleavable substrate *(27)*. Proteolysis at the tumor site results in internalization of the cell penetrating peptide, as well as any attached cargo. ACPPs have demonstrated preclinical utility in *in vivo* imaging with both fluorescent and MRI readouts, and have entered into clinical development at Avelas Biosciences to enable enhanced intraoperative tumor visualization *(28–30)*.

Activity-based probes (ABPs) are a mechanistically orthogonal approach to imaging protease activity. Rather than relying on cleavage of a peptide substrate, ABPs leverage reactive warheads that can covalently bind to protease active sites *(31)*. A built-in recognition sequence can be designed to enhance ABP specificity for specific proteases. ABPs have emerged as useful tools for profiling active proteases *in vitro* because of their unique ability to covalently bind to the target protease, thus enabling mechanistic exploration of underlying protease dysregulation in disease and health *(31)*. Furthermore, ABPs can incorporate quenched fluorophores to enable *in vivo* visualization of protease dysregulation *(32)*.

The power of such imaging methods lies in their ability to directly visualize disease processes. Unfortunately, existing imaging methods suffer from very limited capacity for multiplexing *(33)*. In optical imaging, fluorophores with wavelengths shorter than ~750 nm suffer from very poor penetration through biological tissue and can be confounded by tissue autofluorescence *(34)*. Because of the heterogeneity of cancer, single-plex protease sensors have little chance of offering high enough sensitivity to enable reliable detection across a population. Furthermore, because protease activity is dysregulated in a number of benign diseases in addition

to cancer, single-plex sensors are susceptible to false positives from infection, sterile inflammation, or fibrosis, among other benign etiologies. Because of these sensitivity and specificity limitations, the clinical utility of such imaging approaches has largely been limited to use in patients with already established diagnoses of cancer, such as in patients undergoing surgical tumor resection.

1.4 Thesis Overview

The past few years have seen the emergence of a new class of activity-based diagnostics that aims to overcome the limitations of imaging by converting disease-associated protease activity into a urinary readout. These "activity-based nanosensors" (ABNs) are administered into the body and can reach the site of disease either by passive accumulation or by active targeting *(35–41)*. There, dysregulated proteases cleave peptides presented on the nanoparticle surface, which liberates a reporter molecule. This reporter molecule is designed to be small enough to rapidly re-enter the bloodstream and clear the body via renal filtration. This urinary reporter provides additional levers that can be tuned by engineering, and has variably been read out with ELISA *(36)*, colorimetric assays *(40)*, and mass spectrometry *(35)*.

At the initiation of this thesis, ABNs had been leveraged to enable disease detection in xenograft mouse models of cancer, as well as in models of benign disease like pneumonia *(39)*, liver fibrosis *(35)*, and thrombosis *(42, 43)*. All of these studies involved intravenous (or, in one case, subcutaneous *(43)*) administration of ABNs. By incorporating active targeting that relied on tumor expression of specific integrins, ABNs were able to detect tumors as small as 36 mm^3 in an orthotopic model of advanced ovarian cancer *(38)*. Furthermore, by leveraging orthogonal mass-barcoded reporter molecules, up to 20 ABNs had been multiplexed in a single mouse, but the integration of these multiplexed signals was limited to linear classifiers which were not evaluated prospectively (i.e. on independent test cohorts) *(35, 41)*. ABNs had been shown to enable

monitoring of treatment response in lung infection, but had not yet been evaluated in monitoring drug response in cancer or other noncommunicable lung diseases.

Because respiratory diseases are leading causes of death and disability in the world *(44)*, this thesis aimed to optimize ABNs for lung disease sensing. Specifically, we sought to leverage multiplexing, machine learning, and intrapulmonary delivery to develop ABNs that enable accurate detection and treatment response monitoring in clinically relevant mouse models of lung diseases. Furthermore, we aimed to develop tools to query protease activity in tissue samples, a key step toward understanding the biology of protease dysregulation in disease and enabling the rational design of activity-based diagnostics. In the first section, we combine multiplexing, intrapulmonary delivery, and machine learning in genetically engineered mouse models of lung cancer to enable detection of small, localized lung tumors. In the second section, we demonstrate that such an approach can enable noninvasive drug response monitoring in models of malignant and benign lung disease. Finally, in the third section, we establish methods to measure protease activity in biospecimens and demonstrate the bottom-up development of a protease-activated diagnostic probe. Collectively, this thesis represents a bridge toward clinical implementation of activity-based nanosensors for detection and monitoring of pulmonary diseases.

CHAPTER 2. DETECT LOCALIZED LUNG CANCER WITH HIGH SENSITIVITY AND SPECIFICITY

2.1 Introduction

Lung cancer is the most common cause of cancer-related death (25.3% of cancer deaths in the United States), with dismal 18.6% five-year survival rates *(45)*. Underlying this high mortality is the fact that 57% of lung cancer patients have distant spread of disease at the time of diagnosis *(45)*. Because patients with regional or localized disease have six- to 13-fold higher five-year survival rates than patients with distant metastases *(45)*, substantial effort has been dedicated to early detection of lung cancer. In the US, screening with low-dose computed tomography (LDCT) is recommended in high-risk patients (adults aged 55 to 80 years with a 30 pack-year smoking history *(5)*) and enabled a relative reduction in mortality of 20% when compared to chest radiography in the National Lung Screening Trial (NLST) *(6)*. However, in addition to expense *(8)* and risks associated with radiation exposure *(46)*, LDCT suffers from high false positive rates *(6)*, leading to a considerable burden of complications incurred during unnecessary follow-up procedures. Transthoracic needle biopsy, for example, is associated with a 15% rate of pneumothorax and a 6.6% rate of pneumothorax requiring chest drainage *(47)*. Overall, the risk of dying or suffering a major complication in a LDCT-screened patient with a benign nodule is 4.1 and 4.5 per 10,000, respectively *(46)*. As a result of these limitations, screening by LDCT has not been widely adopted outside of the US *(9)* and there is an urgent need to develop diagnostic tests that increase the effectiveness of lung cancer screening.

Great strides in molecular diagnostics have yielded promising approaches that may be used in conjunction with or as an alternative to LDCT for lung cancer screening. Circulating tumor DNA (ctDNA) has emerged as a promising tool for noninvasive molecular profiling of lung cancer *(13, 48)*. However, the presence of ctDNA scales with tumor burden and there are thus fundamental

sensitivity limits for early stage disease *(48, 49)*. In patients with a suspicious nodule identified by LDCT, transcriptional profiling of bronchial brushings can enhance the diagnostic sensitivity of bronchoscopy alone *(50)*, leveraging the "field of injury" that results from smoking and other environmental exposures. However, as with any invasive procedure, bronchoscopy carries the risk of attendant complications such as pneumothorax *(6, 46)*.

Rather than relying on imaging or the detection of endogenous biomarkers in circulation, we have developed a class of "activity-based nanosensors" that monitor for a disease state by detecting and amplifying the activity of aberrant proteases and which function as urinary reporters *(35–42)*. Protease activity is dysregulated in cancer, and proteases across all catalytic classes play a direct role in tumorigenesis *(22, 51)*. Activity-based nanosensors leverage dysregulated protease activity to overcome the insensitivity of previous biomarker assays, amplifying disease-associated signals generated in the tumor microenvironment and providing a concentrated urine-based readout. We have previously explored the sensitivity of this approach using mathematical modeling *(52)* and cell transplant models *(38)*. However, to drive accurate diagnosis in a heterogeneous disease, a diagnostic must also be highly specific. Here, we explored the potential to attain both sensitive and specific lung cancer detection by multiplexing 14 activity-based nanosensors in two immunocompetent, autochthonous mouse models driven by either *Kras*/*Trp53* (KP) mutations or *Eml4-Alk* (EA) fusion. Clinically, activity-based nanosensors may have utility as an alternative to invasive follow-up procedures in patients with positive LDCT findings.

2.2 Results

Aberrant protease expression is induced in a *Kras*- and *Trp53*-mutant mouse model of lung adenocarcinoma

Common driver mutations of non-small cell lung cancer (NSCLC) in humans include those that activate *KRAS* (10-30%) or inactivate *TP53* (50-70%) *(53)*. To examine the ability of activity-

based nanosensors to detect lung cancer in a relevant mouse model (Fig. 2.1), we selected a genetically driven model of adenocarcinoma that incorporates mutations in these genes.

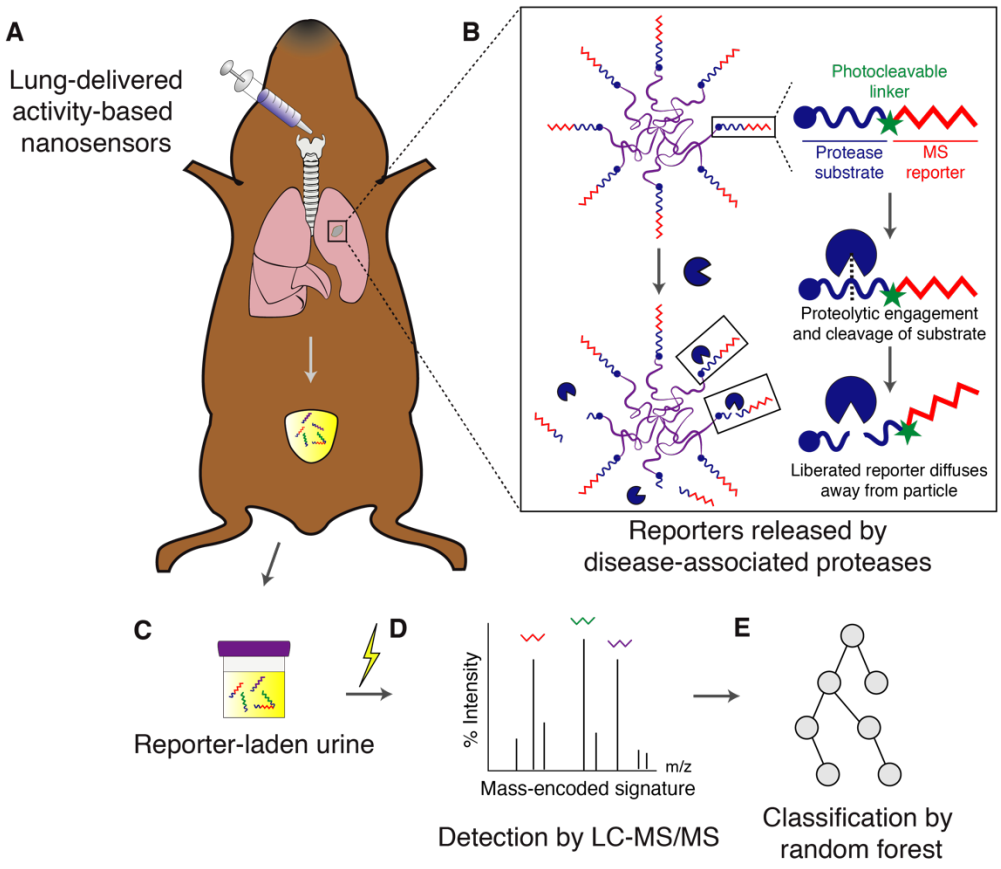

Figure 2.1. Study approach and overview. (**A**) Activity-based nanosensors are administered to mice by intratracheal instillation. (**B**) At the tumor periphery, disease-associated proteases cleave protease substrates, liberating mass-encoded (MS) reporters from the PEG scaffold. (**C**) These reporters are small enough to diffuse into the bloodstream and passively filter into the urine, where they are photocleaved to release attached substrate fragments, yielding free mass-encoded reporters. (**D**) These reporters can subsequently be quantified by LC-MS/MS. (**E**) Classification is performed on a training cohort of mice and subsequently applied to an independent test cohort to provide a positive or negative readout of malignancy.

This extensively characterized model uses intratracheal administration of a virus encoding Cre recombinase to activate mutant *Kras*^{G12D} and delete both copies of *Trp53* in the lungs (*Kras*$^{LSL\text{-}G12D/+}$;*Trp53*$^{fl/fl}$ (KP) mice; fig. 2.S1A), initiating tumors that closely recapitulate human disease progression from alveolar adenomatous hyperplasia (AAH) to grade IV adenocarcinoma (fig. 2.S1B) *(54)*.

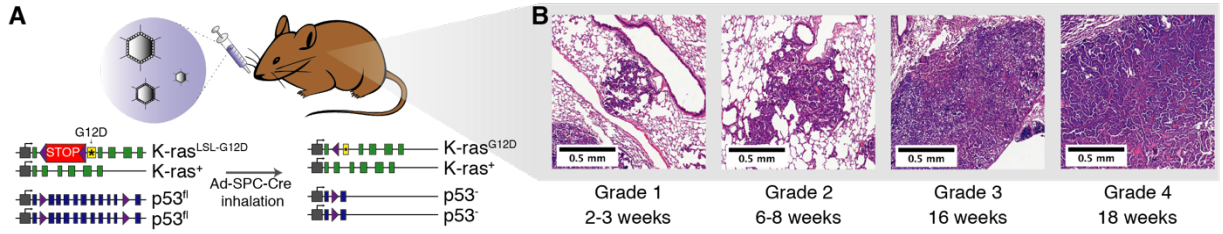

Figure 2.S1. KP model genetically and histologically recapitulates human lung adenocarcinoma. (**A**) Disease was induced in the KP model by intratracheal instillation of adenovirus expressing Cre recombinase under the control of the surfactant protein C (SPC) promoter, which resulted in activation of mutant *K-ras*^{G12D} and excision of both copies of *Trp53* in type II alveolar cells *(54)*. (**B**) Histologically, disease progressed from low grade dysplasia to invasive adenocarcinoma over 18-20 weeks (shown are representative lesions of each grade in a single, advanced-stage KP mouse).

We analyzed a recently published RNA-Seq dataset *(55)* that profiled KP tumors (n = 22) across disease stages, as well as *Kras*-mutant, *Trp53*-WT tumors (K, n = 3) to identify proteases that were upregulated in tumor cells relative to normal lung cells (Fig. 2.2A). Because this dataset profiled tumor cells sorted by flow cytometry and therefore failed to capture proteases contributed by microenvironmental immune and stromal cells, we supplemented this analysis with a bulk gene expression microarray dataset profiling K tumors *(56)*, which are transcriptionally similar to early-stage KP tumors and human lung adenomas *(55)*. We used significance analysis of microarrays (SAM) *(57)* to identify proteases with increased expression in K model tumors relative to normal lungs (Fig. 2.2B).

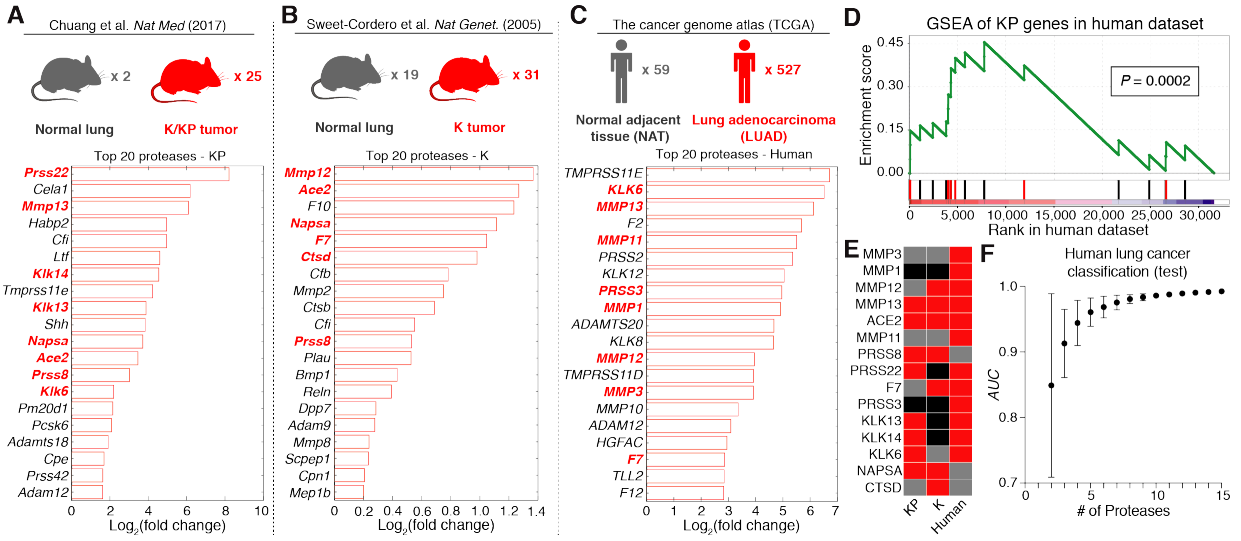

Figure 2.2. Proteases are upregulated in lung cancer and enable classification of human disease. (**A-C**) Existing mouse (A,B) and human (C) gene expression datasets were analyzed to identify extracellular endoproteases overexpressed in lung cancer. Protease genes in red were selected for the "LUAD protease panel". (**D**) GSEA was performed in the TCGA (human) dataset using orthologs of the top 20 overexpressed protease genes in KP tumors ($P = 0.0002$). Red bars are genes included in the "LUAD protease panel". (**E**) A set of 15 proteases was selected as the "LUAD protease panel". Red: $Fold_{Disease} > 1$, Grey: $Fold_{Disease} < 1$, where $Fold_{Disease}$ is gene expression in disease relative to control. Black: Not included in dataset. (**F**) GLM classification on the TCGA dataset using the 15 protease genes in the "LUAD protease panel" as features. AUC for the test cohort is shown as a function of the number of proteases included in the classifier ($n = 50$ combinations of protease genes for each point). Points are mean +/- SD.

Proteases overexpressed in the KP mouse model are relevant to human lung adenocarcinoma

To ensure that activity-based nanosensors were tuned to address human lung adenocarcinoma (LUAD)-associated proteases, we mined The Cancer Genome Atlas (TCGA) dataset *(58)* and analyzed expression of 168 human extracellular endoprotease genes in LUAD and normal adjacent tissue (Fig. 2.2C) *(59)*. Of the 20 most highly upregulated proteases, nine were metalloproteases, 11 were serine proteases, and several overlapped with proteases overexpressed in KP tumors (Fig. 2.2C, bottom). Indeed, we found using gene set enrichment analysis (GSEA) *(60)* that the top 20 overexpressed extracellular proteases in the KP model were significantly enriched in human LUAD ($P = 0.0002$) (Fig. 2.2D), suggesting that the proteolytic landscape of the KP model recapitulated that of human disease. We then performed receiver operating characteristic (ROC) analysis on RNA-Seq data curated by the Lung Genomics Research Consortium (LGRC) *(61)* and

found that proteases overexpressed in human LUAD were not increased in interstitial lung disease (ILD) or chronic obstructive pulmonary disease (COPD) (fig. 2.S2A). In contrast, classification efficiency in LUAD reached above 0.9 for eight out of ten proteases (fig. 2.S2B-D).

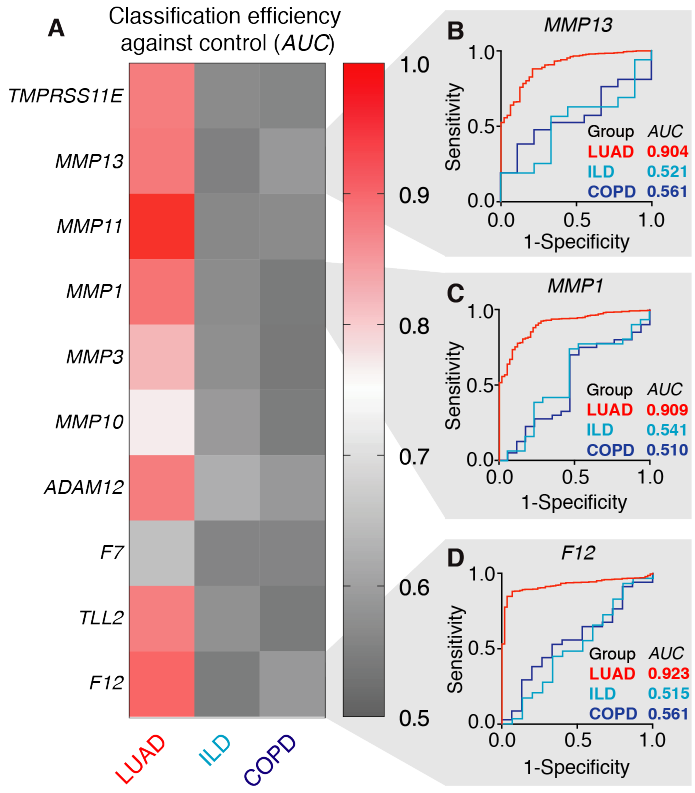

Figure 2.S2. Human LUAD-associated proteases are not overexpressed in benign lung diseases. (**A**) RNA-Seq data curated by the Lung Genomics Research Consortium (LGRC) was analyzed to assess the classification performance of human lung cancer-associated proteases in interstitial lung disease (ILD, n = 31) and chronic obstructive pulmonary disease (COPD, n = 41) against normal lung (n = 17). Of the top 20 overexpressed proteases in human LUAD, 10 were included in the LGRC dataset with FPKM values greater than zero for at least half of the samples. ROC analysis was performed for LUAD (from TCGA) and ILD and COPD (from LGRC) against their respective controls, using FPKM values for each protease. (**B-D**) ROC curves for individual proteases in the panel are shown.

A panel of proteases overexpressed in human and mouse lung adenocarcinoma enables classification of human disease

We next sought to nominate a set of proteases against which to build our nanosensor panel. We excluded any genes for which an active recombinant protease was unavailable, selected six to seven of the top 20 overexpressed genes from each dataset, removed duplicates, and arrived at a

"LUAD protease panel" of 15 protease genes (Fig. 2.2E, and indicated in bold red text in Fig. 2.2A-C). This panel included napsin A, a highly sensitive and specific immunohistochemical marker for human LUAD *(62)*, and several metalloproteases known to be expressed at the protein level in human LUAD *(63)*. To assess whether the expression of these 15 proteases enabled classification of LUAD from normal adjacent tissue, we built a generalized linear model (GLM) classifier using a subset of the TCGA gene expression data, applied it to an independent test cohort, and found that the area under the ROC curve (AUC) was 0.99 when all 15 proteases were used as features (Fig. 2.2F). Additionally, as assessed by GSEA, this 15-gene panel was significantly enriched in stage I LUAD (fig. 2.S3A, $P < 0.0001$), as well as all tested molecular subtypes of adenocarcinoma, including *KRAS*-mutant (fig. 2.S3B, $P < 0.0001$), *TP53*-mutant (fig. 2.S3C, $P = 0.0002$), *EGFR*-mutant (fig. 2.S3D, $P = 0.0004$), and *BRAF*-mutant (fig. 2.S3E, $P = 0.0002$) genetic subtypes. Last, we performed differential expression analysis of lung squamous cell carcinoma (LUSC) relative to normal adjacent tissue from the TCGA dataset and found significant enrichment of the same 15-protease panel by GSEA (fig. 2.S3F, $P = 0.0002$).

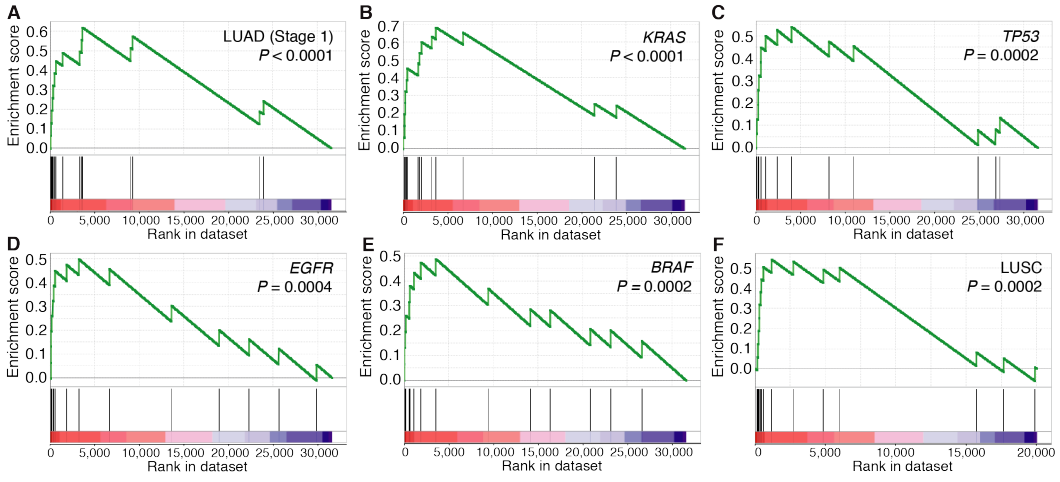

Figure 2.S3. LUAD protease panel genes are enriched across genetic and histological lung cancer subtypes. (**A-F**) GSEA plots showing enrichment of LUAD protease panel genes in stage I LUAD (A; $n_{LUAD} = 302$, $n_{NAT} = 29$; $P < 0.0001$), *KRAS*-mutant LUAD (B; $n_{LUAD} = 75$, $n_{NAT} = 58$; $P < 0.0001$), *TP53*-mutant LUAD (C; $n_{LUAD} = 64$, $n_{NAT} = 58$; $P = 0.0002$), *EGFR*-mutant LUAD (D; $n_{LUAD} = 28$, $n_{NAT} = 58$; $P = 0.0004$), *BRAF*-mutant LUAD (E; $n_{LUAD} = 17$, $n_{NAT} = 58$; $P = 0.0002$) and LUSC (F; $n_{LUSC} = 233$, $n_{NAT} = 17$; $P = 0.0002$).

Cleavage of multiplexed substrate panel follows class-specific patterns

We synthesized 14 fluorogenic peptide substrates (PPQ1-14, table 2.S1) that were known to encompass the cleavage preferences of metalloproteases, serine proteases, and aspartic proteases *(41)*.

Name	Fluorophore	Substrate
PPQ1	5FAM	GGPQGIWGQK(CPQ2)-PEG2-C
PPQ2	5FAM	GGPVGLIGK(CPQ2)-PEG2-C
PPQ3	5FAM	GGPVPLSLVMK(CPQ2)-PEG2-C
PPQ4	5FAM	GGPLGLRSWK(CPQ2)-PEG2-C
PPQ5	5FAM	GGPLGVRGKK(CPQ2)-PEG2-C
PPQ6	5FAM	GGfPRSGGGK(CPQ2)-PEG2-C
PPQ7	5FAM	GGLGPKGQTGK(CPQ2)-kk-PEG2-C
PPQ8	5FAM	GGGSGRSANAKG-K(CPQ2)-PEG2-GC
PPQ9	5FAM	GKPISLISSG-K(CPQ2)-PEG2-GC
PPQ10	5FAM	GILSRIVGGG-K(CPQ2)-PEG2-GC
PPQ11	5FAM	GSGSKIIGGG-K(CPQ2)-PEG2-GC
PPQ12	5FAM	GGPLGMRGG-K(CPQ2)-GC
PPQ13	5FAM	GP-(Cha)-G-Cys(Me)-HAG-K(CPQ2)-GC
PPQ14	5FAM	GAPFEMSAG-K(CPQ2)-GC

Table 2.S1. Reporter and substrate sequences for *in vitro* recombinant protease screen. 5FAM, 5-Carboxyfluorescein; CPQ2, quencher; PEG, polyethylene glycol; Cha, 3-Cyclohexylalanine; Cys(Me), methyl-cysteine; lowercase letters, *D*-amino acids.

We incubated each individual probe with each of the 15 proteases in the panel (Fig. 2.3A) and measured protease activity by monitoring fluorescence increase over time (Fig. 2.3B). Hierarchical clustering of fluorescence fold changes of each substrate revealed separation of proteases of different classes (Fig. 2.3C).

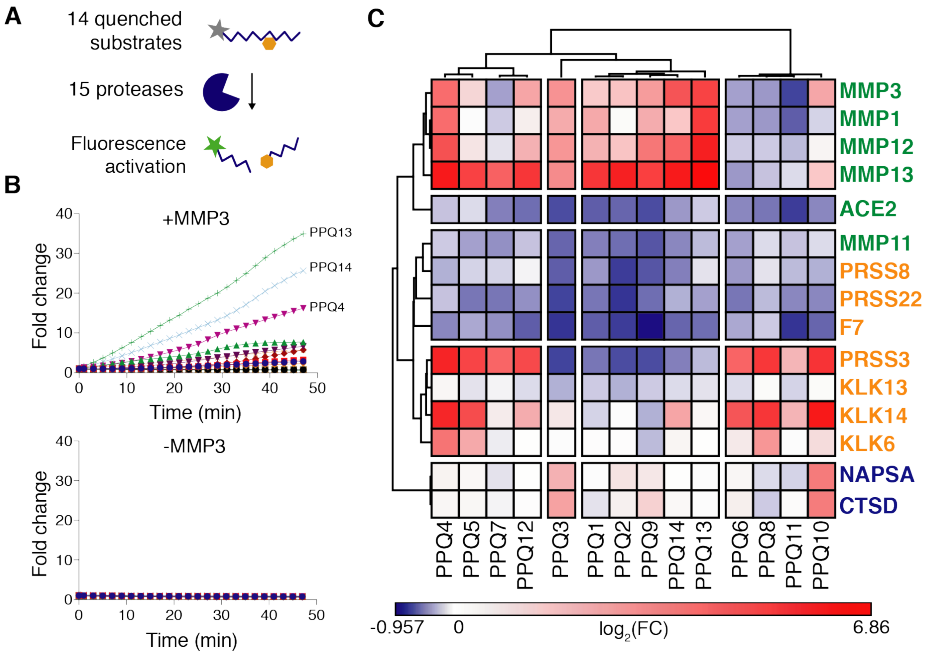

Figure 2.3: LUAD substrate panel cleavage patterns are driven by protease class. (**A**) All 15 proteases in the "LUAD protease panel" were screened against a panel of 14 Förster resonance energy transfer (FRET)-paired protease substrates and fluorescence activation was monitored over 45 minutes. (**B**) Kinetic fluorescence curves are shown for 14 FRET-paired substrates with (upper panel) and without (lower panel) addition of MMP3. (**C**) Fluorescence fold changes at 45 minutes (average of 2 replicates) were $\log_2$ transformed and hierarchical clustering was performed to cluster proteases (vertical) by their substrate specificities and substrates (horizontal) by their protease specificities. Proteases labeled in green, orange, or blue represent metallo-, serine, or aspartic proteases, respectively.

Whereas certain probes were cleaved selectively by individual classes of proteases, such as metalloproteases for PPQ2 and serine proteases for PPQ11, other probes were cleaved by proteases of multiple classes (fig. 2.S4). For example, in addition to being cleaved by metalloproteases, PPQ3 and PPQ12 were acted upon by aspartic proteases and serine proteases, respectively (fig. 2.S4). Overall, the dequenching panel results indicated that the set of 14 probes provided coverage of the cleavage profiles of all three protease families represented by the LUAD protease panel.

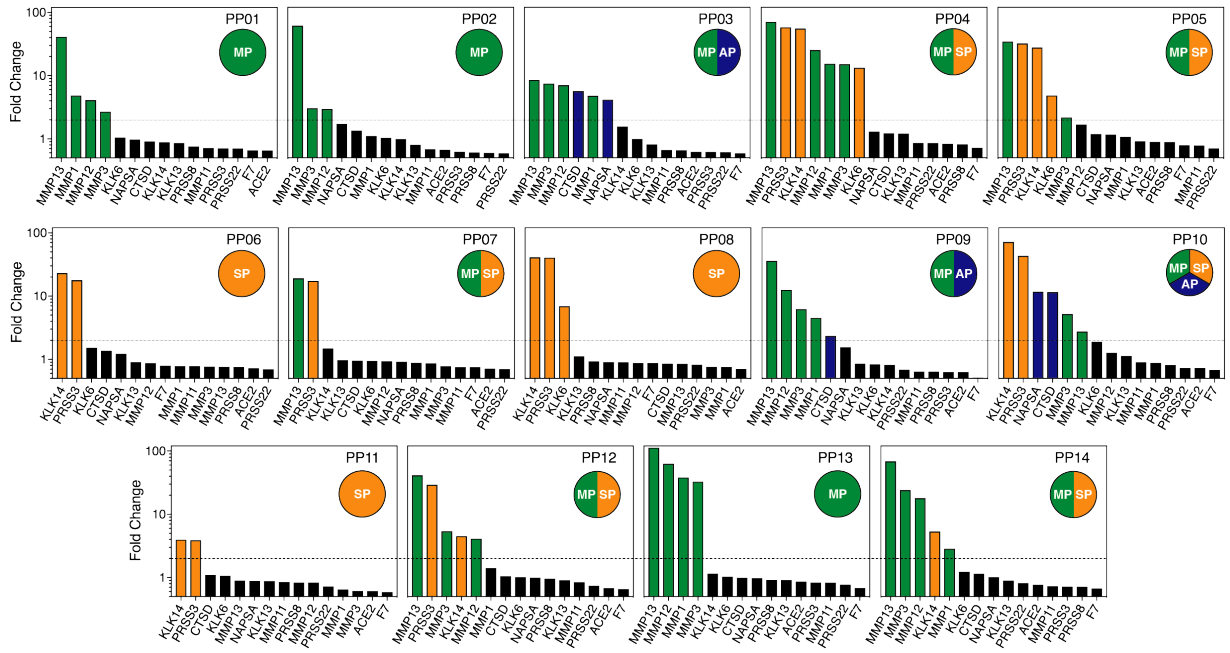

Figure 2.S4. Peptide substrates are cleaved by one or a combination of metallo-, serine, and aspartic proteases. Quantification of *in vitro* proteolytic cleavage of fluorogenic peptide substrates. Y axis represents fluorescence fold change after 45 minutes of incubation with recombinant protease and dotted line is at fold change = 2. Bars are colored according to the catalytic class of the protease (green, metalloprotease-specific; orange, serine protease-specific; blue, aspartic protease-specific).

Nanoparticles delivered into mouse airways distribute throughout the lung and reach the tumor periphery

To adapt the activity-based nanosensor platform for detection of localized lung cancer, we sought to circumvent background protease activity present in the blood and off-target organs by administering the nanosensors via localized intrapulmonary, rather than systemic intravenous, delivery. We built activity-based nanosensors using a 40 kDa eight-arm poly(ethylene glycol) (PEG-8_{40kDa}) nanoparticle coupled to protease substrates bearing terminal mass-encoded reporters (Fig. 2.1B). To assess biodistribution of the nanosensors following intrapulmonary delivery, we labeled the PEG-8_{40kDa} scaffold with near-infrared dye VivoTag750 (VT750), delivered the nanoparticles to mice by intratracheal (IT) intubation or intravenous (IV) injection, and collected organs after 60 minutes (Fig. 2.4A).

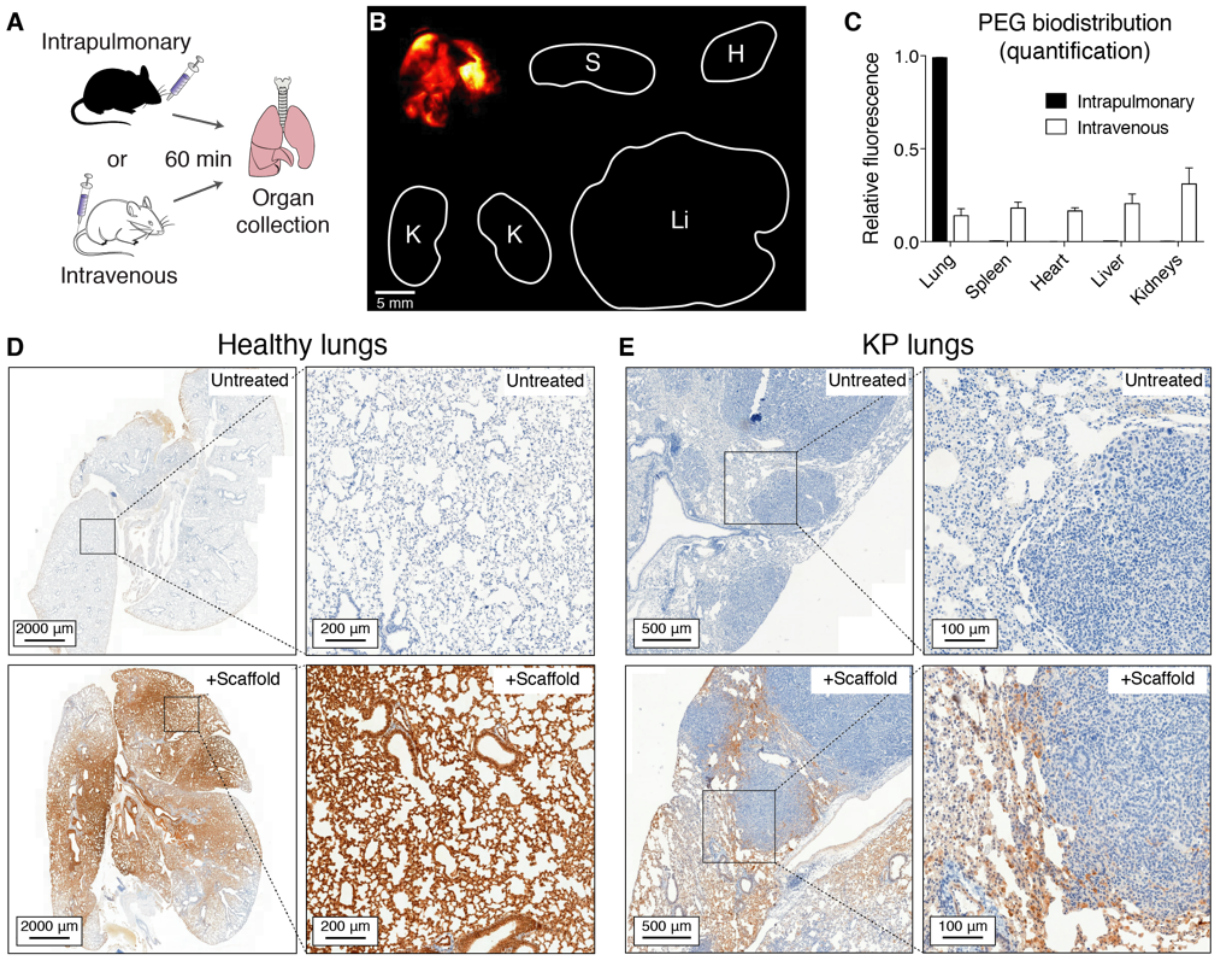

Figure 2.4: Intrapulmonary-administered nanoparticle scaffolds penetrate deep within the lung and reach the periphery of KP tumors. (**A**) Wild-type mice were treated IT or IV with VT750-labeled PEG-8_{40kDa} and biodistribution was assessed. (**B**) Fluorescent imaging of organs was performed 60 min post-IT delivery. Clockwise from top-left: lung, spleen, heart, liver, kidneys. (**C**) Organ-specific biodistribution was quantified (n = 4 each condition). Error bars represent SD. (**D**) Healthy mice were either untreated (above, n = 1) or treated with IT administration of biotin-labeled PEG scaffold (below, n = 2), followed by excision of lungs and immunohistochemical staining for biotin (brown). (**E**) Advanced-stage (16.5 week) KP mice were either untreated (top, n = 3) or treated with IT administration of biotin-labeled PEG scaffold (bottom, n = 3), followed by excision of lungs and immunohistochemical staining as in (D).

Fluorescence imaging revealed deep delivery of nanoparticles to all lung lobes in mice receiving IT particles, but negligible delivery to other organs (Fig. 2.4B-C). In contrast, only 14% of organ fluorescence was confined to the lung in the IV-delivered group. In the IT-treated mice, the lung half-life of PEG-8_{40kDa} was 6.3 days (fig. 2.S5).

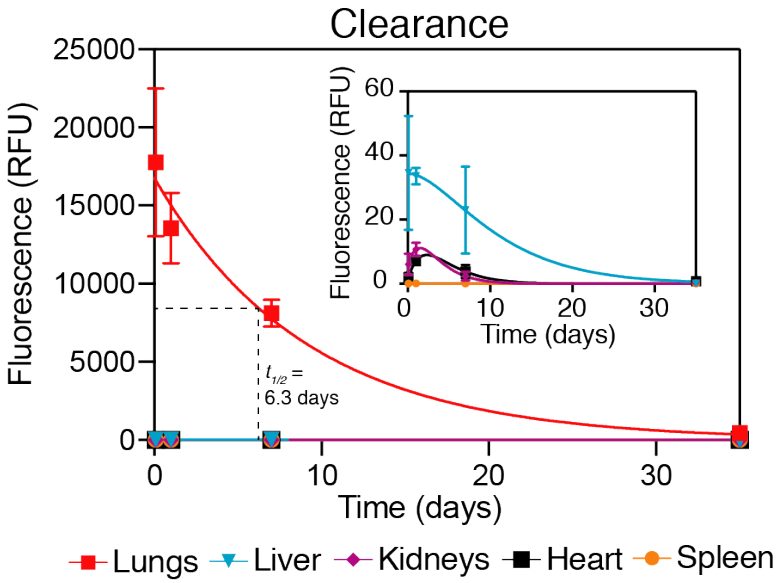

Figure 2.S5. Clearance of PEG-8_{40kDa} nanoparticles from lungs follows single phase exponential decay kinetics. Fluorescence of lungs, liver, kidneys, heart, and spleen of mice after intrapulmonary delivery of VT750-labeled PEG-8_{40kDa} (n = 5 per time point). Points are mean +/- SD. Lung clearance data was fit with nonlinear regression using single phase exponential decay ($t_{1/2}$ = 6.3 days, R^2 = 0.86). Inset: liver, kidneys, heart, and spleen fluorescence are presented on a smaller scale y-axis and were fit with nonlinear regression using two phase exponential growth and decay.

No toxicity was observed at either short (2 hours) or longer (24 hours and over 10 days) intervals after nanosensor administration in healthy control mice, as assessed by weight tracking (fig. 2.S6A) and histological assessment by a veterinary pathologist (fig. 2.S6B).

To assess microscopic distribution of the nanosensor scaffold within the lung, we labeled the PEG-8_{40kDa} scaffold with biotin and administered the nanoparticles to healthy mice by intratracheal instillation. Lungs were collected from mice 20-30 minutes post-IT delivery, fixed, and stained for biotin. Whereas lungs from untreated mice were negative for biotin (Fig. 2.4D, top), lungs from mice that received the scaffold demonstrated broad distribution of nanoparticles throughout the lung (Fig. 2.4D, bottom left), specifically within terminal alveoli (Fig. 2.4D, bottom right).

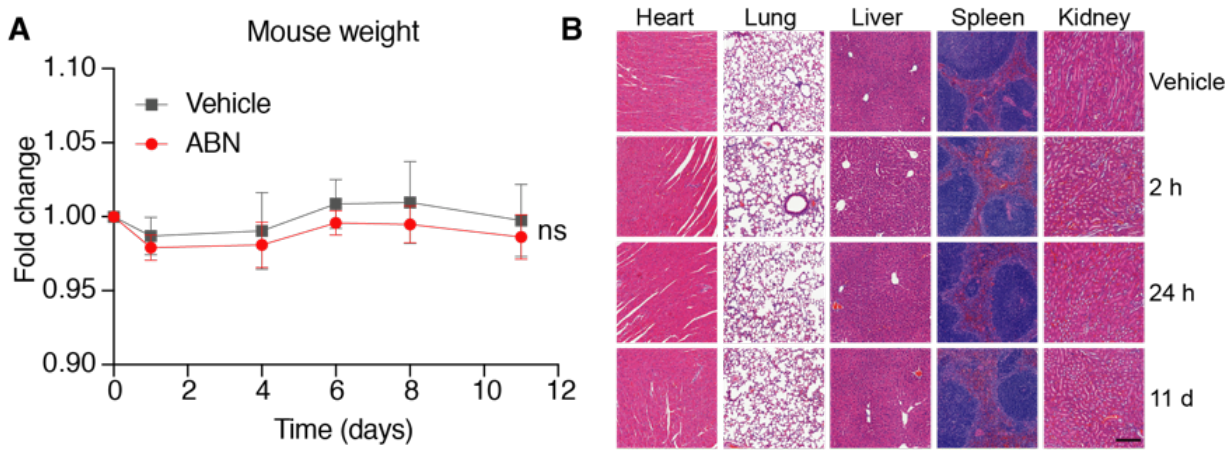

Figure 2.S6. No toxicity is observed in mice treated with intrapulmonary activity-based nanosensors. (**A**) Fold changes in mouse weights after treatment with either peptide-functionalized activity-based nanosensors (red; $n = 9$, days 0 to 1; $n = 6$, days 4 to 11) or mannitol buffer ('Vehicle'; grey; $n = 8$). (**B**) Representative H&E images of mouse organs at 2 hours, 1 day, and 11 days after intrapulmonary activity-based nanosensor treatment. Scale bar is 200 μm.

We then administered biotin-labeled PEG-8_{40kDa} scaffold in late-stage KP tumor-bearing mice by intratracheal intubation, to assess whether these particles were able to reach the site of disease. Again, whereas lungs from untreated KP mice were negative for biotin (Fig. 2.4E, top), lungs from KP mice that received intrapulmonary delivery of the biotinylated scaffold demonstrated presence of nanoparticles at the margins of tumors (Fig. 2.4E, bottom).

As a step toward developing a more clinically relevant delivery method, we also sought to characterize particle durability and biodistribution after aerosolization. We directly aerosolized our PEG carrier particles (fig. 2.S7A-B) and found no aggregation or changes in particle size distribution, as assessed by transmission electron microscopy (TEM) (fig. 2.S7C-D) and dynamic light scattering (DLS) (fig. 2.S7E). Furthermore, PEG-PPQ5 pre- and post-aerosolization was equally sensitive to *in vitro* cleavage by recombinant MMP13 (fig. 2.S7F).

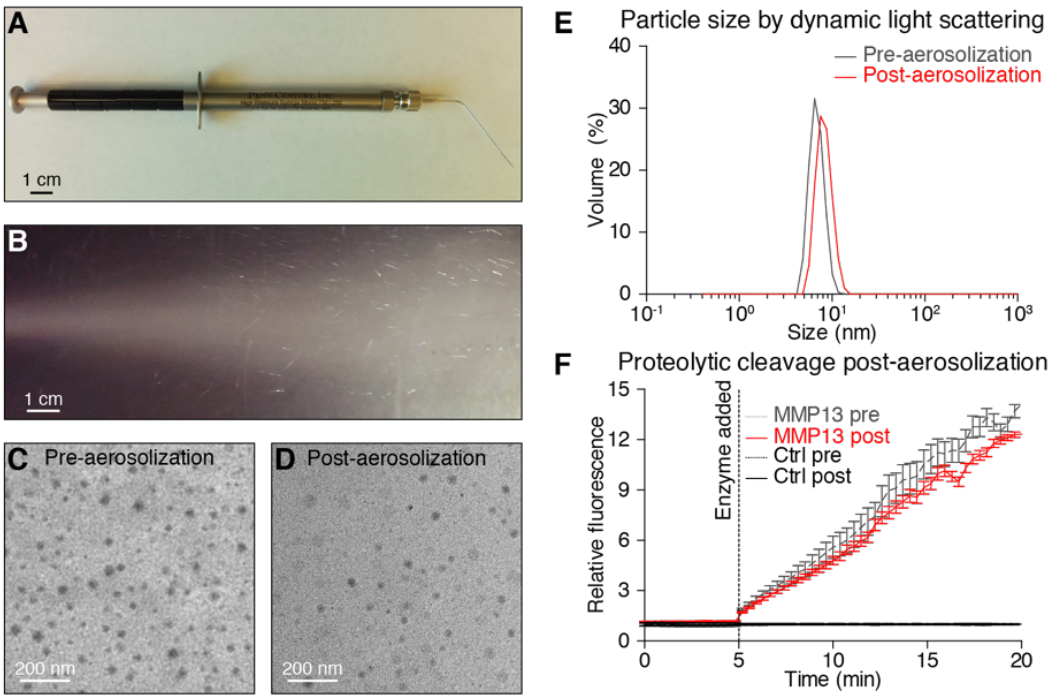

Figure 2.S7. Activity-based nanosensors are stable to aerosolization. (**A**) Device used for intratracheal administration of aerosolized nanosensors. (**B**) Aerosol produced from 50 μL of buffer. Scale for A and B is 1 cm. (**C, D**) TEM images of nanoparticle PEG-8_{40kDa} scaffold pre- (C) and post- (D) aerosolization. Scale is 200 nm. (**E**) Representative DLS quantification of particle sizes pre- and post-aerosolization of PEG-8_{40kDa} scaffold (n = 3). (**F**) Fluorescent dequenching by MMP13 of fluorogenic nanosensor PEG-PPQ5, pre (grey) (n = 4) and post (red) (n = 4) aerosolization. PEG-PPQ5 fluorescence change without addition of MMP13 is shown in black (n = 4).

Last, we functionalized the PEG nanoparticles with either a near-infrared dye for biodistribution studies or biotin for histological assessment and used pressure-driven aerosolization to perform intrapulmonary administration. Gross fluorescent visualization of VT750 revealed deep penetration throughout the lung and in all lobes (fig. 2.S8A), without distribution to other organs (fig. 2.S8B). Histological staining of fixed lungs collected from mice 10 minutes post-inhalation demonstrated no biotin staining in control lungs (fig. 2.S8C-D) but broad staining throughout the lung overall (fig. 2.S8E) and in terminal alveoli (fig. 2.S8F) in mice treated with aerosolized nanoparticles.

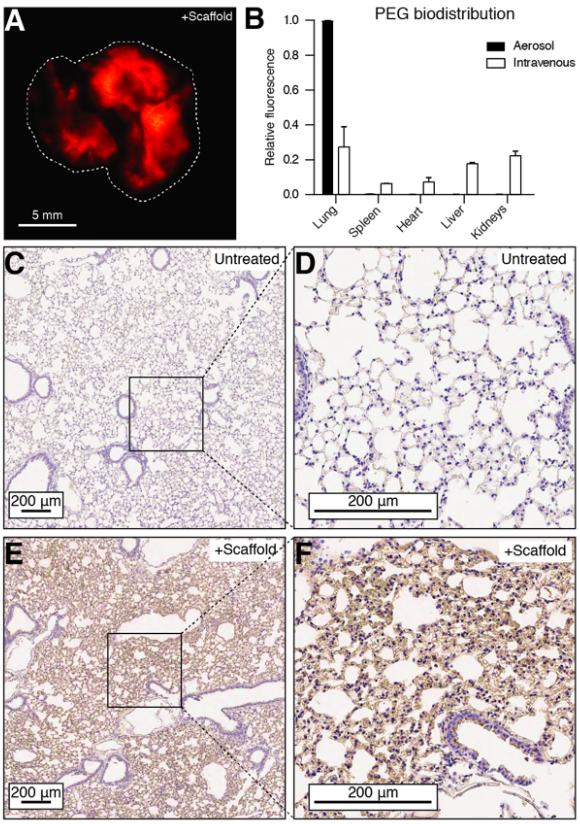

Figure 2.S8. Aerosolized nanoparticles penetrate deep within the lung and avoid distribution to off-target organs. (**A**) Representative image of lungs from a mouse treated with aerosolized fluorophore-labeled PEG-8_{40kDa}. Scale is 5 mm. (**B**) Organ-specific biodistribution of fluorophore-labeled PEG-8_{40kDa} 60 minutes after aerosol (red) (n = 2) or intravenous (grey) (n = 2) delivery. (**C-F**) Stained sections of untreated lungs (C-D) or lungs fixed 10 min post-aerosol delivery of biotin labeled PEG-8_{40kDa} (E-F). Scale bar for (C-F) is 200 µm.

Mass-encoded reporters filter from the lung to the urine via the blood and are detectable by mass spectrometry

To enable multiplexed detection of a broad spectrum of disease-associated proteases via a single *in vivo* administration of nanosensors, we conjugated each member of the LUAD substrate panel to a uniquely identifiable mass-encoded reporter (PP1-14; Table 2.1). As previously described *(35)*, we used variable labeling of the 14-mer glutamate-fibrinopeptide B (Glu-Fib) with stable isotope-labeled amino acids to uniquely barcode each of the 14 peptide substrates. Multiple reaction monitoring via a liquid chromatography triple quadrupole mass spectrometer (LC-

MS/MS) enabled quantitative assessment of urinary reporter concentration within a broad linear range (1-1000 ng/ml, fig. 2.S9A).

Name	Reporter	Photolabile Group	Substrate	Nanocarrier
PP01	e(+2G)(+6V)ndneeGFFsAr	ANP	GGPQGIWGQC	PEG_8-40kDa
PP02	eG(+6V)ndneeGF(+1F)s(+1A)r	ANP	GGPVGLIGC	PEG_8-40kDa
PP03	e(+3G)(+1V)ndneeGFFs(+4A)r	ANP	GGPVPLSLVMC	PEG_8-40kDa
PP04	e(+2G)Vndnee(+2G)FFs(+4A)r	ANP	GGPLGLRSWC	PEG_8-40kDa
PP05	eGVndnee(+3G)(+1F)Fs(+4A)r	ANP	GGPLGVRGKC	PEG_8-40kDa
PP06	e(+2G)(+6V)ndnee(+3G)(+1F)(+1F)s(+1A)r	ANP	GGfPRSGGGC	PEG_8-40kDa
PP07	eG(+6V)ndnee(+3G)(+1F)Fs(+4A)r	ANP	GGLGPKGQTGC	PEG_8-40kDa
PP08	e(+3G)(+1V)ndneeG(+10F)FsAr	ANP	GGGSGRSANAKGC	PEG_8-40kDa
PP09	eGVndneeGF(+10F)s(+4A)r	ANP	GGKPISLISSGC	PEG_8-40kDa
PP10	e(+2G)(+6V)ndneeG(+10F)(+1F)s(+1A)r	ANP	GGILSRIVGGGC	PEG_8-40kDa
PP11	e(+3G)(+1V)ndnee(+2G)(+10F)Fs(+4A)r	ANP	GGSGSKIIGGGC	PEG_8-40kDa
PP12	eGVndneeG(+10F)(+10F)sAr	ANP	GGPLGMRGGC	PEG_8-40kDa
PP13	e(+2G)(+6V)ndnee(+3G)(+10F)(+1F)s(+4A)r	ANP	GGP-(Cha)-G-Cys(Me)-HAGC	PEG_8-40kDa
PP14	e(+3G)(+1V)ndnee(+2G)(+10F)(+10F)sAr	ANP	GGAPFEMSAGC	PEG_8-40kDa

Table 2.1. Reporter and substrate sequences for *in vivo* urinary diagnostics. ANP (photocleavable linker), 3-Amino-3-(2-nitro-phenyl)propionic Acid; Cha, 3-Cyclohexylalanine; Cys(Me), methyl-cysteine; lowercase letters, D-amino acids

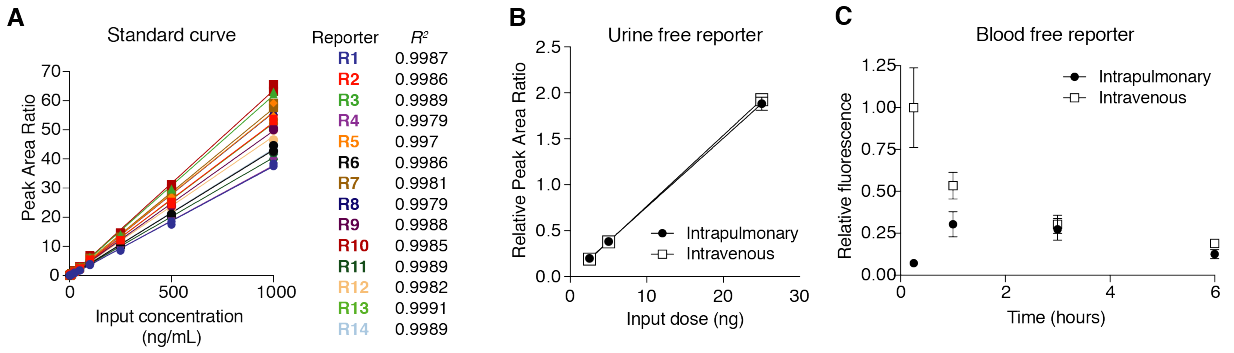

Figure 2.S9. Free reporters enter the bloodstream after pulmonary delivery and are detectable in the urine by mass spectrometry. (**A**) Glu-fib reporters were spiked into urine at concentrations ranging from 1 to 1000 ng/ml and LC-MS/MS was performed. Goodness of fit was assessed by linear regression and is given as Pearson's R^2. (**B**) Healthy mice (n = 4 each group) were administered MS-encoded free reporters (IT and IV) at doses ranging from 2.5 ng to 25 ng and urinary concentrations at 1 hour were assessed by LC-MS/MS ($slope_{IT}$ = 0.075 ng^{-1}, $slope_{IV}$ = 0.077 ng^{-1}). Geometric mean normalized peak area ratio is shown. Error bars represent SD. (**C**) Cy7-labeled free reporters were administered IT and IV and concentration in the blood was assessed over the following 6 hours (n = 4 each group). Error bars represent SD.

By administering mass-encoded free reporters by IT and IV administration, we found that urinary accumulation scaled linearly with input doses between 2.5 ng and 25 ng for both routes of delivery

($slope_{IT}$ = 0.075 ng^{-1}, $slope_{IV}$ = 0.077 ng^{-1}; fig. 2.S9B). Administering a Cy7-labeled version of Glu-Fib, we found characteristic single-exponential concentration decay following IV injection and a two-phase kinetic profile following IT administration (fig. 2.S9C), suggesting an initial phase of partitioning from the alveoli into the blood (peaking at 1 to 2 hours after delivery) followed by renal filtration from the blood.

	5 weeks		7.5 weeks		10.5 weeks	
Mouse	**Multiplicity**	**Volume (mm^3)**	**Multiplicity**	**Volume (mm^3)**	**Multiplicity**	**Volume (mm^3)**
KP1	0	0	1	0.5	1	0.5
KP2	0	0	0	0	3	5.2
KP3	1	1.8	3	2.8	6	13
KP4	3	2.8	3	6.5	6	27
KP5	0	0	0	0	5	17.8
KP6	0	0	6	4.4	6	22.7
KP7	2	4.7	4	7	4	16.8
KP8	0	0	2	1	Motion Artifact	Motion Artifact
KP9	0	0	2	4.7	3	42.6
KP10	0	0	0	0	3	16.8
KP11	0	0	2	4.7	2	4.7
KP12	1	0.5	1	1.8	8	43.9
MicroCT Sensitivity	**33.3%**		**75%**		**100%**	
V_{avg} (mm^3)	**0.775**		**2.78**		**19.2**	

Table 2.S2. Quantification of tumor burden in KP mice by microCT. V_{avg}, average tumor volume. MicroCT sensitivity is defined as the number of mice with detectable tumors divided by the total number of mice at each time point.

Activity-based nanosensor cleavage is dysregulated in lung cancer mouse models

We then sought to longitudinally monitor disease progression in KP mice with activity-based nanosensors and benchmark their diagnostic performance against micro-computed tomography (microCT). After initiating disease via intratracheal administration of adenovirus encoding Cre recombinase (fig. 2.S1A), we monitored tumor development by performing microCT at 5 weeks (KP_{5wk}), 7.5 weeks ($KP_{7.5wk}$), and 10.5 weeks ($KP_{10.5wk}$) after adenoviral induction (Fig. 2.5A, table

2.S2). The sensitivity of microCT at 100% specificity was 33.3% at 5 weeks, 75% at 7.5 weeks, and 100% at 10.5 weeks, and average tumor burden at these three time points was 0.775 mm^3, 2.78 mm^3, and 19.2 mm^3 (Fig. 2.5A, table 2.S2).

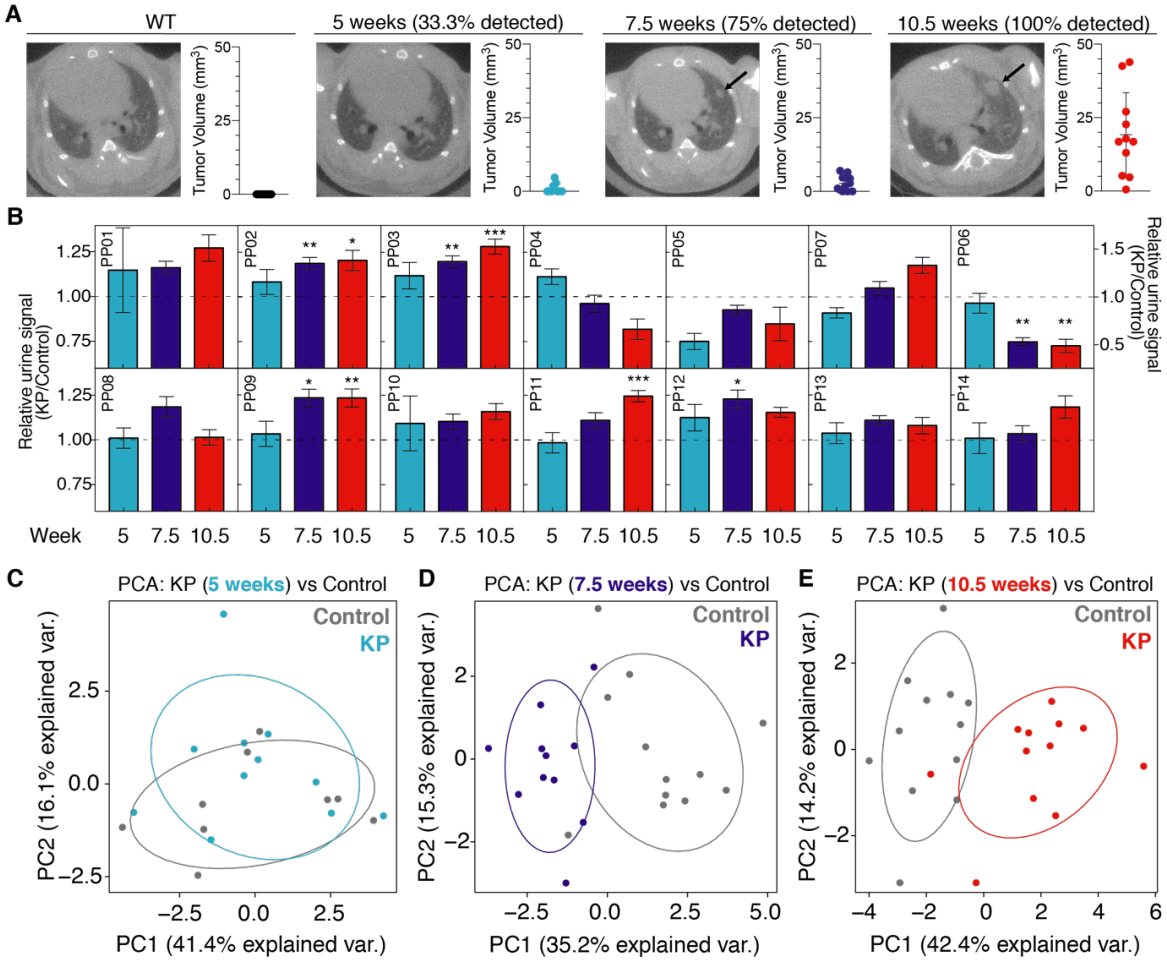

Figure 2.5: Activity-based nanosensors distinguish between diseased and healthy mice. (**A**) Tumor development was monitored by microCT in healthy (left, $n = 11$) and KP_{5wk} ($n = 12$), $KP_{7.5wk}$ ($n = 12$), and $KP_{10.5wk}$ ($n = 11$). Right three panels represent time series of a single mouse, with arrow indicating development of a single nodule over time. Quantification of tumor volume is shown to the right of each image, and percentage of mice with detectable tumors at each time point (% detected) is shown above each panel. (**B**) Urine output of activity-based nanosensors administered to KP and control animals at 5 weeks (KP: $n = 11$; Control: $n = 9$), 7.5 weeks (KP: $n = 11$; Control: $n = 12$), and 10.5 weeks (KP: $n = 12$; Control: $n = 12$) after tumor induction. For clarity, PP06 is presented on a larger scale y axis. * $P_{adj} < 0.05$, ** $P_{adj} < 0.01$, *** $P_{adj} < 0.001$ indicate significant differences from control by either two-tailed *t*-test with Holm-Sidak correction (for normally distributed reporters) or Mann-Whitney test with Bonferroni correction (for non-normal reporters). Error bars represent SEM. (**C-E**) PCA of mean normalized urinary reporters for KP mice and controls at 5 weeks (KP: $n = 11$; Control: $n = 9$) (C), 7.5 weeks (KP: $n = 11$; Control: $n = 12$) (D), and 10.5 weeks (KP: $n = 12$; Control: $n = 12$) (E).

To characterize activity-based nanosensor performance *in vivo* relative to microCT, we administered all 14 protease-sensitive nanoparticles to the lungs of KP mice and age- and sex-matched healthy controls at 5, 7.5, and 10.5 weeks after tumor initiation. Several reporters differentiated KP mice from healthy controls, with some reporter differences (for example PP03, PP11) becoming amplified over time (Fig. 2.5B). At 7.5 and 10.5 weeks, 5 out of 14 reporters were significantly different between KP and healthy mice ($P_{adj} < 0.05$), whereas none of the reporters differed at 5 weeks (fig. 2.S10).

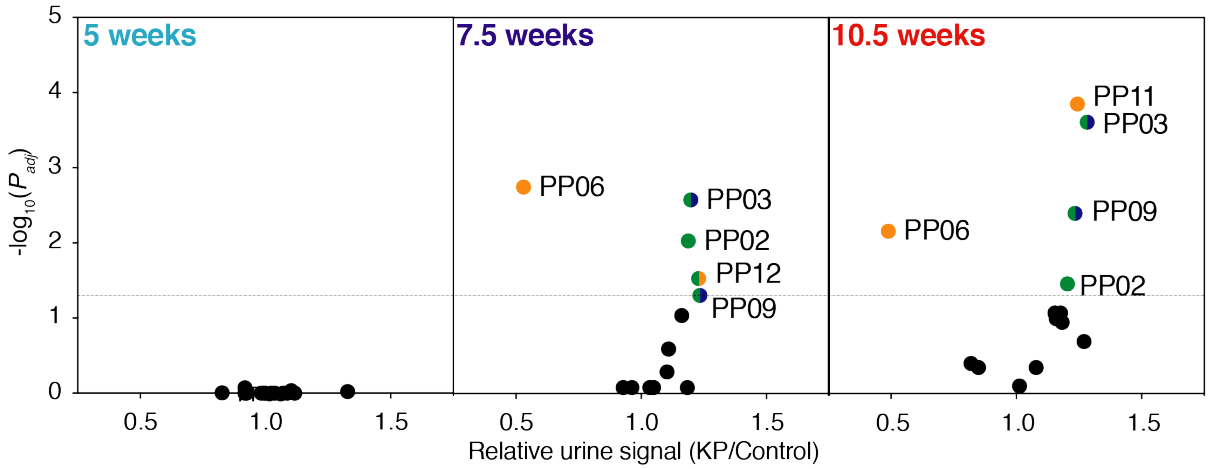

Figure 2.S10. Multiple reporters are differentially enriched in the urine of healthy mice and KP mice at 7.5 and 10.5 weeks. Mean normalized urinary reporter concentrations in KP mice and healthy mice were compared at 5 weeks (KP: $n = 11$; Control: $n = 9$), 7.5 weeks (KP: $n = 11$; Control: $n = 12$), and 10.5 weeks (KP: $n = 12$; Control: $n = 12$) after tumor induction and $-\log_{10}(P_{adj})$ was plotted against fold change between KP and control. Significance was calculated by either two-tailed *t*-test followed by adjustment for multiple hypotheses with Holm-Sidak correction (for normally distributed reporters) or Mann-Whitney test with Bonferroni correction (for non-normal reporters). Dotted line is at $P_{adj} = 0.05$. Significant reporters are color-coded according to the classes of protease that cleave their corresponding peptide substrates *in vitro* (fig. S4) (green, metalloprotease-specific; orange, serine protease-specific; blue, aspartic protease-specific).

In contrast, intratracheal administration of the same 14-plex panel to mice bearing flank xenograft tumors (average tumor volume of 448 mm^3) derived from a human colorectal cancer cell line yielded no differential urinary reporters between xenograft and control mice (fig. 2.S11A-B).

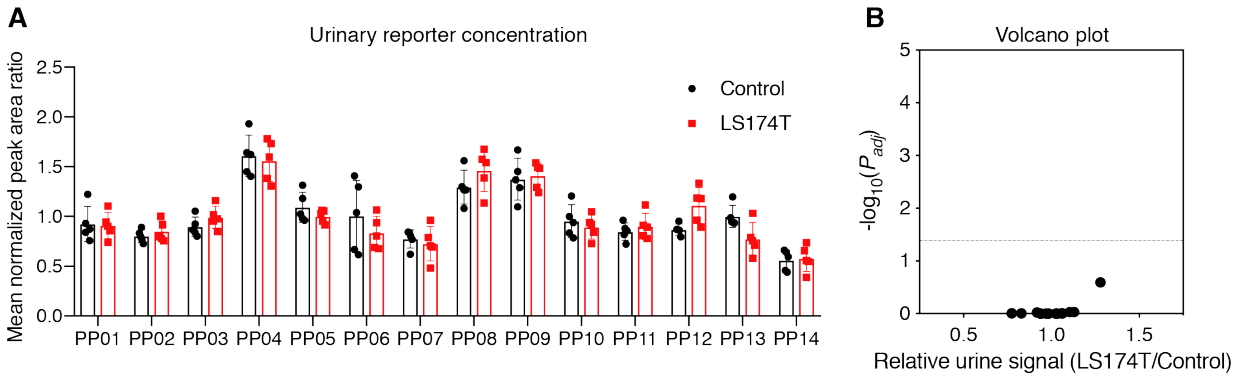

Figure 2.S11. Extrapulmonary disease is undetectable by intrapulmonary activity-based nanosensors. (A) Mean normalized urinary reporter output for healthy control mice (black, $n = 5$) or mice bearing flank LS174T tumors (red, $n = 5$). **(B)** Volcano plot shows no differential enrichment of any of the 14 reporters detected in the urine of diseased mice relative to healthy controls, as assessed by either two-tailed *t*-test followed by adjustment for multiple hypotheses with Holm-Sidak correction (for normally distributed reporters) or Mann-Whitney test with Bonferroni correction (for non-normal reporters).

Of the 5 reporters enriched in $KP_{7.5wk}$ urine, three (PP02, PP03, and PP09) were also enriched in $KP_{10.5wk}$ urine, and these sequences corresponded to peptides cleaved by metalloproteases or both metalloproteases and aspartic proteases *in vitro*. However, the most significantly enriched reporter in the urine of KP mice at 10.5 weeks (PP11; $P_{adj} = 0.0001$) corresponded to a peptide cleaved only by serine proteases *in vitro*. Unsupervised dimensionality reduction by principal component analysis (PCA) separated most KP and control mice at 7.5 and 10.5 weeks, but not at 5 weeks (Fig. 2.5C-E).

Though the KP model is a well-established, autochthonous model of lung adenocarcinoma, it only represents one subset of human disease. We sought to assess the generalizability of activity-based nanosensors to other genetic subtypes by leveraging the Eml4-Alk (EA) model *(64)*, an autochthonous model in which intrapulmonary administration of adenovirus encoding two short guide RNAs (sgRNAs) and Cas9 results in translocation and fusion of the *Eml4* and *Alk* genes, yielding lung adenocarcinoma that histologically resembles human disease. We administered the same panel of 14 nanosensors in EA mice 5 weeks, 7.5 weeks, and 10.5 weeks after adenoviral induction and found differential urinary reporter signatures at all three time points (fig. 2.S12A),

enabling separation of diseased mice from healthy controls at all three time points, as revealed by PCA (fig. 2.S12B). Notably, although several reporters were differentially enriched in the urine of both KP and EA mice, others were unique to one model; the consistent enrichment of PP01, a robust metalloprotease-specific nanosensor in EA mice but not in KP mice (fig. 2.S10) suggests differential regulation of a subset of metalloproteases in these two models.

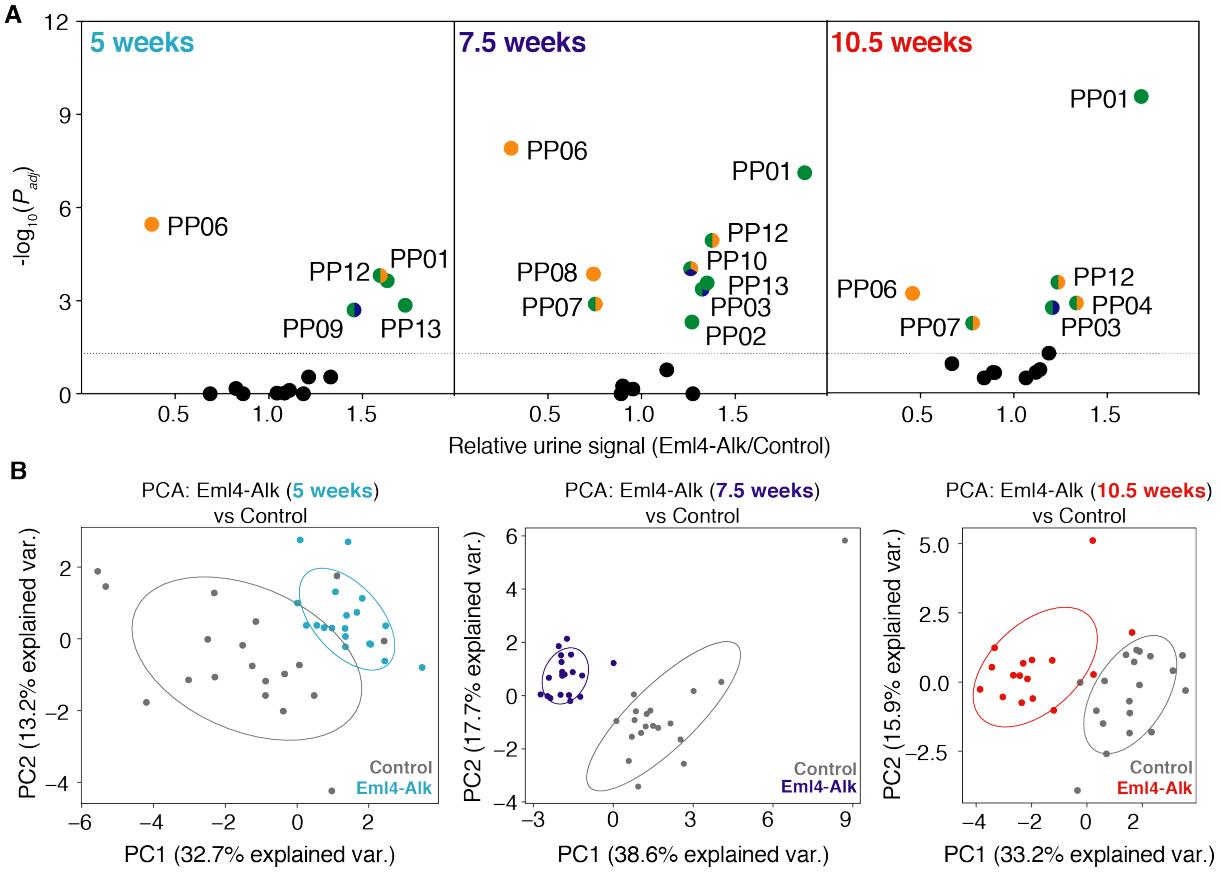

Figure 2.S12: Intrapulmonary activity-based nanosensors differentiate mice bearing Alk-driven lung cancer from healthy controls. (**A**) Mean normalized urinary reporter concentrations in EA mice and healthy mice were compared at 5 weeks (n = 19 each group) (left), 7.5 weeks (EA, n = 20; Control, n = 19) (middle) and 10.5 weeks (EA, n = 16; Control, n = 19) (right) after tumor induction and -$\log_{10}(P_{adj})$ was plotted against fold change between EA and control. Significance was calculated by either two-tailed t-test with Holm-Sidak correction (for normally distributed reporters) or Mann-Whitney test with Bonferroni correction (for non-normal reporters). Dotted line is at P_{adj} = 0.05. Significant reporters are color-coded according to the classes of protease that cleave their corresponding peptide substrates *in vitro* (fig. S4) (green, metalloprotease-specific; orange, serine protease-specific; blue, aspartic protease-specific). (**B**) PCA of urinary reporter output of EA mice and healthy controls at 5 weeks (n = 19 each group) (left), 7.5 weeks (EA, n = 20; Control, n = 19) (middle) and 10.5 weeks (EA, n = 16; Control, n = 19) (right) after tumor induction.

Activity-based nanosensor cleavage signatures are distinct in malignant and benign disease models

Existing lung cancer diagnostic modalities like LDCT suffer from high false positive rates, resulting in cost, anxiety, and morbidity to patients due to unnecessary invasive follow-up procedures *(46)*. We hypothesized that multiplexed measurements of pulmonary protease activity would enable discrimination of malignant from benign disease. To assess the specificity of activity-based nanosensors for lung cancer versus benign inflammatory disease, we leveraged a well-established model of lung inflammation, induced by intratracheal administration of lipopolysaccharide (LPS) *(65)*. We found that several reporters were differentially enriched in the urine of $KP_{7.5wk}$ mice (fig. 2.S13A) and $EA_{7.5wk}$ mice (fig. 2.S13B) relative to LPS-treated mice, enabling separation of KP, EA, LPS, and healthy mice by PCA (fig. 2.S13C).

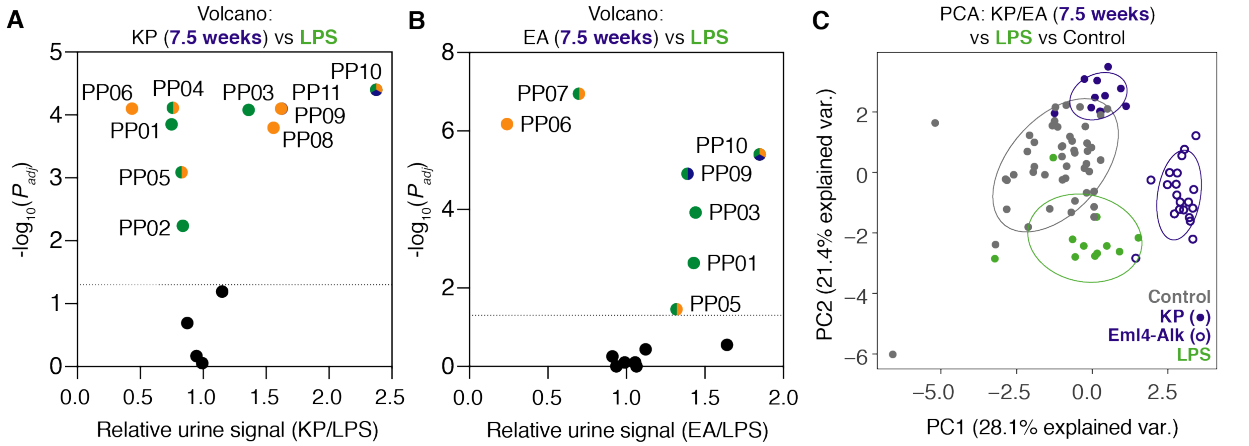

Figure 2.S13. Pulmonary activity-based nanosensor cleavage profile is distinct in lung cancer and benign lung inflammation. (**A-B**) Volcano plots of urinary reporter outputs from $KP_{7.5wk}$ (n = 11) (A) and $EA_{7.5wk}$ (n = 20) (B) mice relative to LPS-treated mice (n = 11), where -$\log_{10}(P_{adj})$ was plotted against fold change. Significance was calculated by either two-tailed t-test with Holm-Sidak correction (for normally distributed reporters) or Mann-Whitney test with Bonferroni correction (for non-normal reporters). Dotted line is at P_{adj} = 0.05. Significant reporters are color-coded according to the classes of protease that cleave their corresponding peptide substrates *in vitro* (fig. S4) (green, metalloprotease-specific; orange, serine protease-specific; blue, aspartic protease-specific). (**C**) PCA of urinary reporter outputs from $KP_{7.5wk}$ (n = 11), $EA_{7.5wk}$ (n = 20), and LPS (n = 11) mice, as well as healthy control mice from all three experiments (n = 47).

Machine learning classification enables sensitive and specific lung cancer detection

Having demonstrated that activity-based nanosensors enable detection of two autochthonous models of lung adenocarcinoma, with cleavage patterns that were distinct from LPS-induced lung inflammation, we leveraged machine learning to build a classifier that could be prospectively applied to enable disease diagnosis. We trained a random forest classifier *(66)* using the urinary reporter output from a subset of $KP_{7.5wk}$ (n = 6), $EA_{7.5wk}$ (n = 6), and healthy (n = 12) mice and tested its ability to classify each LUAD model from healthy control mice in an independent test cohort consisting of mice that were not included in classifier training (n = 5-31; see table 2.S3 for cohort compositions).

	5 weeks		7.5 weeks		10.5 weeks	
KP v. Healthy (Fig. 2.6A)	**Train**	**Test**	**Train**	**Test**	**Train**	**Test**
Healthy	0	9	12	6	0	12
KP	0	11	6	5	0	12
Eml4-Alk	0	0	6	0	0	0
Eml4-Alk v. Healthy (Fig. 2.6B)	**Train**	**Test**	**Train**	**Test**	**Train**	**Test**
Healthy	0	17	12	13	0	19
KP	0	0	6	0	0	0
Eml4-Alk	0	19	6	14	0	16
LUAD v. Healthy (Fig. 2.6C)	**Train**	**Test**	**Train**	**Test**	**Train**	**Test**
Healthy	0	26	12	19	0	31
KP	0	11	6	5	0	12
Eml4-Alk	0	19	6	14	0	16
LUAD v. Benign (Fig. 2.6D)	**Train**	**Test**	**Train**	**Test**	**Train**	**Test**
Healthy	0	0	12	19	0	0
KP	0	0	6	5	0	0
Eml4-Alk	0	0	6	14	0	0
LPS	0	0	6	5	0	0

Table 2.S3. Composition of training and test cohorts for random forest classification. Cohort numbers used to train and test random forest classifiers applied in Fig. 2.6A-C (KP v. Healthy, Eml4-Alk v. Healthy, LUAD v. Healthy) and Fig. 2.6D (LUAD v. Benign).

Area under the receiver operating characteristic curve analysis revealed robust classification of $KP_{7.5wk}$ and $KP_{10.5wk}$ ($AUC_{7.5wks}$ = 0.95; $AUC_{10.5wks}$ = 0.93) (Fig. 2.6A), as well as EA mice at all three time points (AUC_{5wks} = 0.96, $AUC_{7.5wks}$ = 0.98; $AUC_{10.5wks}$ = 0.93) (Fig. 2.6B). We also evaluated the classifier on a test cohort that combined both LUAD models (table 2.S3) and again found robust classification at 7.5 weeks and 10.5 weeks ($AUC_{7.5wks}$ = 0.97; $AUC_{10.5wks}$ = 0.93) (Fig. 2.6C). Finally, we sought to determine whether a classifier could be built to distinguish lung cancer-bearing mice from both healthy mice and mice with benign lung inflammation. We trained a second classifier incorporating $KP_{7.5wk}$, $EA_{7.5wk}$, LPS-treated, and healthy control mice (table 2.S3), applied it to an independent test cohort, and found that it performed with high accuracy in discriminating $KP_{7.5wk}$, $EA_{7.5wk}$, and a combination of the two (termed "$LUAD_{7.5wk}$") from healthy and LPS-treated mice (AUC_{KP} = 0.97; AUC_{EA} = 0.98; AUC_{LUAD} = 0.97) (Fig. 2.6D). Together, these data illustrate the power of multiplexed, lung-specific activity-based nanosensors for sensitive and specific detection of localized lung cancer.

2.3 Discussion

In this work, we present an advance toward clinical translation of a new class of biomarkers, activity-based nanosensors. We found that such multiplexed nanosensors, when delivered by intratracheal instillation, performed with specificity of 100% and sensitivity up to 95% for detection of localized disease in two autochthonous lung adenocarcinoma models representing *Kras*/*Trp53* and *Alk*-mutant disease. Furthermore, we found that LPS-induced lung inflammation did not result in false positives. Our approach overcomes the intrinsic sensitivity limitation of blood-based diagnostic assays for localized disease by profiling disease activity directly within the tumor microenvironment and providing multiple steps of signal amplification *(52)*. Using intratracheal instillation delivery, we further ensured that virtually all nanosensors reached the lung and bypassed nonspecific activation in off-target organs.

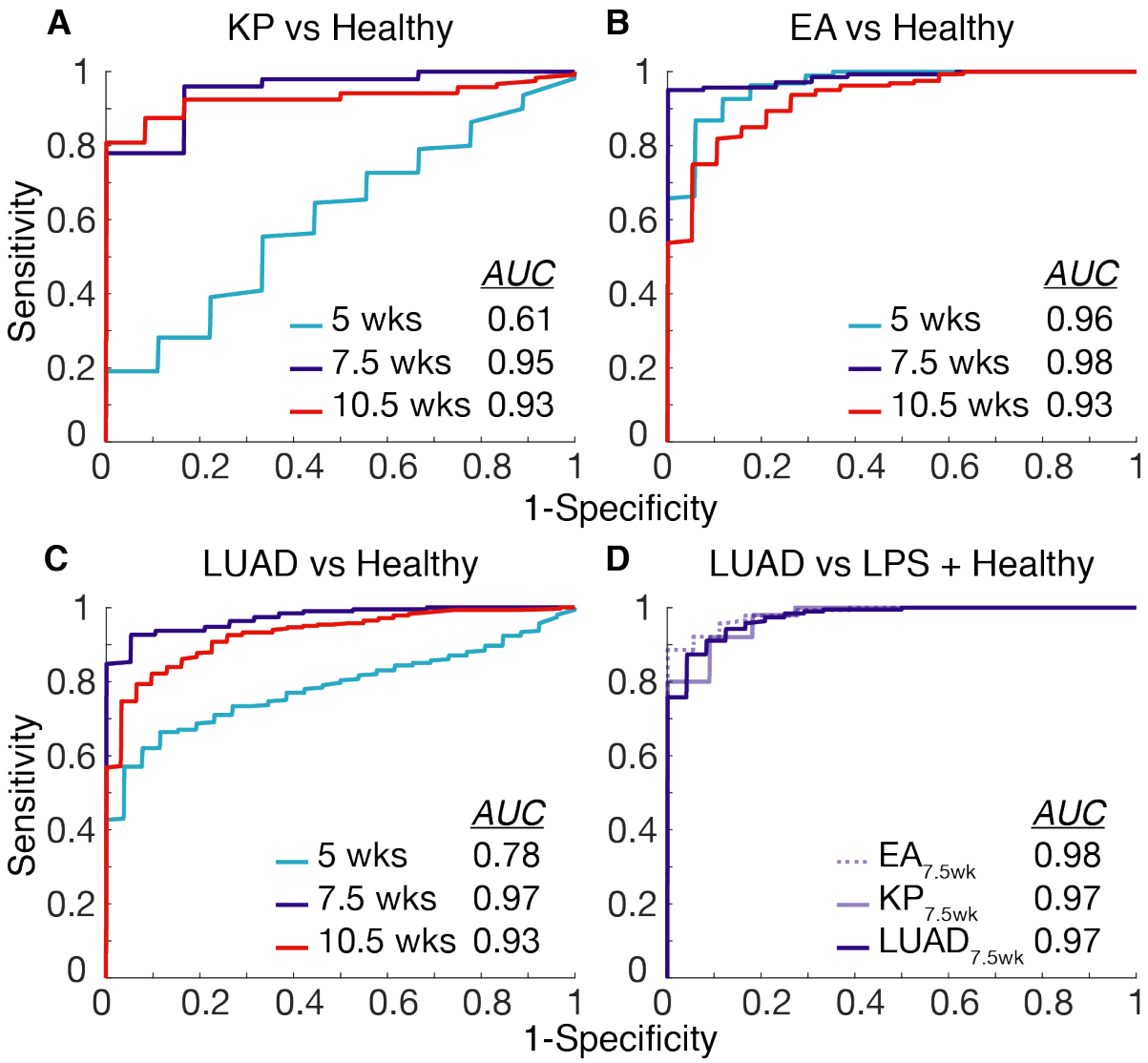

Figure 2.6: Machine learning enables sensitive and specific classification of two genetic subtypes of lung adenocarcinoma. (**A-C**) ROC curves showing performance of a single random forest classifier trained on urinary reporters from a subset of $KP_{7.5wk}$, $EA_{7.5wk}$, and healthy controls in discriminating an independent test cohort of KP (A), EA (B), or a combination of KP and EA (C) mice from healthy controls at all three time points. (**D**) ROC curve showing performance of a random forest classifier trained on urinary reporters from $KP_{7.5wk}$ and $EA_{7.5wk}$ mice vs. LPS and healthy control mice in discriminating an independent test cohort of $KP_{7.5wk}$, $EA_{7.5wk}$, and a combination of the two (termed "LUAD") from healthy and LPS-treated mice. All ROC curves are averages over 10 independent train/test trials and show the results in the test cohort. n = 5-31; details of cohort sample sizes are shown in table 2.S3.

This study represents a step toward clinical implementation of activity-based nanosensors for lung cancer testing, validating the efficacy of the tool in two autochthonous, immunocompetent models of localized lung adenocarcinoma. The use of genetically engineered mouse models

(GEMMs) offered several advantages over cell transplant models, including the ability to explore stage-specific differences, as well as proteolytic contributions from immune cells. Activity-based nanosensors detected disease as early as 7.5 weeks after initiating the KP model, when only grade 1 AAH and grade 2 adenomas are present *(54)*. Furthermore, though metalloprotease-sensitive nanosensors were, as expected, preferentially cleaved in KP mice at both 7.5 and 10.5 weeks, the activation of PP11 (a serine protease-sensitive substrate) in $KP_{10.5wk}$ mice could point to an unexpected role of serine protease activity in tumor progression at this disease stage. One hypothesis is that tumor-infiltrating immune cells, which secrete a multitude of serine proteases *(67)*, may contribute to nanosensor cleavage in $KP_{10.5wk}$ mice. Indeed, neutrophils are known to infiltrate KP tumors around 10 weeks after tumor induction *(68)*. The potential capacity of activity-based nanosensors to measure immune-mediated protease activity *(39)* raises the prospect of rapid, noninvasive, and longitudinal immunotherapy response monitoring.

Here, we report improved sensitivity of activity-based nanosensors relative to previous work by our group, as well as existing and emerging blood-based diagnostics for cancer. We found that our nanosensors could detect tumors in $KP_{7.5wk}$ mice, whose total tumor volumes were, on average, just 2.78 mm^3 —more than an order of magnitude smaller than our most sensitive method to date (36 mm^3 in an ovarian cancer model) *(38)*. By comparison, in the LS174T colorectal cancer xenograft model, ctDNA is detectable when tumor volumes reach 1,000 mm^3 *(69)*, carcinoembyonic antigen (CEA) is detectable around 135-330 mm^3 *(35, 69)*, and intravenously administered activity-based nanosensors have previously been shown to detect disease in this model around 130 mm^3 *(35)*. Last, in the autochthonous $Kras^{G12D}$-mutant "K" lung cancer model, ctDNA bearing the $Kras^{G12D}$ mutation was only detectable when average tumor volumes were 7.1 mm^3 *(70)*, even with collection of 2.5% of the total mouse blood volume—scaling to 125 ml in humans.

In the NLST, 96.4% of positive LDCT findings were false positives *(6, 46)*, and many of these patients went on to suffer major complications during invasive follow-up procedures *(8, 46)*. Therefore, there is a need to develop noninvasive diagnostic methods that can distinguish between lung cancer and benign lung disease. Here, we demonstrated the specificity of activity-based nanosensors for lung cancer, rather than benign lung inflammation, through multiplexing and machine learning. Though fewer than half of the 14 reporters were differentially enriched in the urine of KP mice and healthy controls, several more had diagnostic power in EA mice, and others were informative in the classification of malignant vs. inflammatory disease. As a result, we found that a pre-trained random forest classifier could distinguish between lung cancer-bearing mice (regardless of subtype) and benign disease controls. Though a clinical study would be necessary to directly assess the effectiveness of activity-based nanosensors in the setting of LDCT lung cancer screening, our results suggest that activity-based nanosensors may complement LDCT for discrimination of malignant lesions from benign disease.

Although this work represents a step toward translation of activity-based nanosensors for lung cancer detection, there are limitations that must be addressed prior to clinical implementation. In this work, we demonstrated the sensitivity and specificity of intrapulmonary activity-based nanosensors for localized lung cancer in two GEMMs of LUAD. Though the advantages of GEMMs over xenograft models in recapitulating human disease are numerous *(71)*, mouse models cannot fully capture the native oncogenic properties or heterogeneity found in human lung cancer and further in vivo validation is needed to confirm the generalizability of activity-based nanosensors to other lung cancer subtypes. Similarly, though activity-based nanosensors can discriminate between lung cancer and LPS-driven lung inflammation, it is possible that clinical lung cancer testing may be confounded by other benign lung disease etiologies or chronic exposure to tobacco smoke. Because of the inherent limitations of mouse models, clinical trials will be

necessary to fully validate the robustness of activity-based nanosensors in detecting lung cancer and distinguishing malignant from benign and extrapulmonary disease in humans. Last, the intrapulmonary delivery methods presented here must be optimized prior to clinical translation. Here, we delivered activity-based nanosensors by intratracheal intubation and demonstrated their stability after aerosolization. However, a clinically relevant intrapulmonary delivery method such as dry powder inhalation or nebulization will be required for clinical implementation.

In summary, intrapulmonary activity-based nanosensors perform with high sensitivity and specificity for detection of localized lung cancer in autochthonous mouse models, via a noninvasive urine test. To engineer these nanosensors, we leveraged analysis of lung adenocarcinoma gene expression datasets to nominate candidate proteases, screened these proteases *in vitro* against a panel of peptide substrates, and directly delivered nanosensors carrying these substrates into the lungs of mice. Activity-based nanosensors may have clinical utility as a rapid, safe, and cost-effective follow-up to LDCT, reducing the number of patients referred for invasive testing. With further optimization and validation studies, activity-based nanosensors may one day provide an accurate, noninvasive, and radiation-free strategy for lung cancer testing.

2.4 Materials and Methods

Study design

The goal of this study was to determine whether intrapulmonary administration of a multiplexed library of activity-based nanosensors could be used to sensitively and specifically detect lung cancer in autochthonous mouse models. All animal studies were approved by the Massachusetts Institute of Technology (MIT) committee on animal care (protocol 0417-025-20) and were conducted in compliance with institutional and national policies. Reporting was in compliance with Animal Research: Reporting In Vivo Experiments (ARRIVE) guidelines. Experiments involving intrapulmonary delivery of activity-based nanosensors in KP mice consisted of 12 KP

mice and 12 healthy control mice; experiments involving intrapulmonary delivery of activity-based nanosensors in EA mice consisted of 20 EA mice and 20 healthy control mice. These mice were monitored, by intratracheal nanosensor administration and microCT, at 5 weeks, 7.5 weeks, and 10.5 weeks after tumor induction. Sample size was selected to ensure a sample size greater than or equal to five for both training and test groups at each time point and for each treatment group. Urine samples with peak area ratio (PAR) values of zero for two or more analytes were excluded, as these samples represented failed nanosensor deliveries and would confound analysis. For differential expression analysis of protease genes in KP mice, genes for which neither normal lung sample was nonzero were excluded, as calculation of fold changes (Tumor/Normal) would otherwise yield undefined values. For ROC analysis in the LGRC dataset, genes for which greater than half of the samples had FPKM values of zero were excluded. During selection of KP and healthy control mice, investigators were blinded to all characteristics but age, sex, and genotype. For random forest classification, mice were randomly assigned to training and test cohorts using a randomly generated seed.

Statistical analysis

For RNA-seq data, binary classification using a generalized linear model was performed using the Caret package *(72)* in the R statistical environment *(73)*. Pre-specified training and testing cohorts were randomly assigned, with 75% and 25% of samples used for training and testing, respectively. For all urine experiments, PAR values were normalized to nanosensor stock concentrations and then mean normalized across all reporters in a given urine sample prior to further statistical analysis. To identify differential urinary reporters, all reporters were first tested for normality by Kolmogorov-Smirnov normality test with Dallal-Wilkinson-Lilliefor *P* value. All normally distributed reporters were subjected to unpaired two tailed *t*-test followed by correction for multiple hypotheses using the Holm-Sidak method, while non-normal reporters were subjected to

Mann-Whitney test with Bonferroni correction in GraphPad Prism 7.0. $P_{adj} < 0.05$ was considered significant. PCA was performed on mean normalized PAR values and implemented in MATLAB R2019b (Mathworks). For disease classification based on urinary activity-based nanosensor signatures, randomly assigned sets of paired data samples consisting of features (the mean-normalized PAR values) and labels (for example KP, EA) were used to train random forest *(66)* classifiers implemented with the TreeBagger class in MATLAB R2019b. Estimates of out-of-bag error were used for cross-validation, and trained classifiers were tested on randomly assigned, held-out, independent test cohorts. The specific composition of train-test cohorts is provided in table 2.S3. Ten independent train-test trials were run for each classification problem, and classification performance was evaluated with ROC statistics calculated in MATLAB. Classifier performance was reported as the mean accuracy and AUC across the ten independent trials.

Gene expression analysis

Human RNA-Seq data from The Cancer Genome Atlas (TCGA) Research Network *(58)* was downloaded from https://www.cancer.gov/tcga and human RNA-Seq data from the Lung Genomics Research Consortium (LGRC) *(61)* was downloaded from https://www.lung-genomics.org/research. The list of human extracellular protease genes was obtained from UniProt. Differential expression analysis on the TCGA data was performed using the DESeq2 differential expression library in the R statistical environment (Fig. 2.2C) *(59, 73)*. AUROC analysis was performed for the TCGA and LGRC datasets using FPKM values from disease samples (LUAD, ILD, and COPD) and their respective controls (NAT for LUAD, normal lung for ILD and COPD), using GraphPad Prism version 7.0a (fig. 2.S2). Genes in the LGRC dataset for which at least half of the samples had FPKM values greater than zero were included in the AUROC analysis, but all zero values were excluded. FPKM values for the KP model *(55)* were downloaded from Gene Expression Omnibus (GEO; GSE84447). Top 20 extracellular endoproteases were identified by

averaging FPKM values across all tumor bearing mice and dividing by the average FPKM values for normal mice (Fig. 2.2A). Genes for which neither of the two normal lung samples had nonzero FPKM values were excluded. Microarray counts for the K dataset *(56)* were downloaded from GEO (GSE49200). Gene expression fold changes were determined by performing quantitative significance analysis of microarrays (SAM) using the "Standard" regression method, 100 permutations, and 10 neighbors for k-nearest neighbors (KNN) classification (Fig. 2.2B) *(57)*.

Pre-ranked GSEA was performed on the LUAD and LUSC gene expression datasets from TCGA using a gene set containing the top 20 overexpressed proteases in the KP model (Fig. 2.2D) or the 15 genes of the LUAD protease panel (fig. 2.S3) *(55)*. The pre-ranked list of $\log_2$(Fold Change) was generated previously by DESeq2. A minimum of 10000 permutations by gene set were performed to calculate the *P* value. GSEA was performed via the GenePattern online software *(74)* and the GSEA desktop application using the "classic" scoring scheme.

Fluorogenic substrate characterization

Fluorogenic protease substrates were synthesized by CPC Scientific. Recombinant proteases were purchased from Enzo Life Sciences, R&D Systems, and Haematologic Technologies. For recombinant protease assays, fluorogenic substrates PPQ1-14 (1 μM final concentration) were incubated in 30 μL final volume in appropriate enzyme buffer, according to manufacturer specifications, with 12.5 nM recombinant enzyme at 37°C (Fig. 2.3). Proteolytic cleavage of substrates was quantified by increases in fluorescence over time by fluorimeter (Tecan Infinite M200 Pro). Enzyme cleavage rates were quantified as relative fluorescence increase over time normalized to fluorescence before addition of protease. Hierarchical clustering was performed in GENE-E (https://software.broadinstitute.org/GENE-E/, Broad Institute), using fluorescence fold changes at 45 minutes.

Intratracheal instillation and in vivo aerosolization studies

For all mouse experiments, anesthesia was induced by isoflurane inhalation (Zoetis), and mice were monitored during recovery. For intratracheal instillation studies, a volume of 50 µl was administered by passive inhalation following intratracheal intubation with a 22G flexible plastic catheter (Exel), as described elsewhere *(54)*. All aerosolization experiments used a MicroSprayer Aerosolizer – Model MSA-250-M (Penn-Century. Inc.) with a volume of 50 µl/mouse by placing the aerosolizer tip in the trachea immediately proximal to the carina and rapidly depressing the plunger.

Biodistribution studies

Biodistribution studies were performed in healthy male C57BL/6 mice. VT750-NHS Ester (PerkinElmer) was coupled to 8-arm 40 kDa PEG-amine (PEG-8_{40kDa}-amine, JenKem) at a 4:1 molar ratio, reacted overnight, and purified by spin filtration (Amicon Ultra centrifugal filter units, Sigma). Mice were lightly anesthetized via isoflurane inhalation, and PEG-8_{40kDa}-VT750 (50 µl volume, 5 µM concentration by VT750 absorbance) was administered by intratracheal instillation (Fig. 2.4B-C) or aerosolization (fig. 2.S8A-B). Mice in the IV cohort were intravenously administered an equal dose of PEG-8_{40kDa}-VT750. Animals were sacrificed by CO_2 asphyxiation at the indicated timepoints post-inhalation/injection and organs were removed for imaging (LICOR Odyssey). Organ fluorescence was quantified in Fiji *(75)* by manually outlining organs, using the "Measure" feature, and taking the mean intensity.

Blood for pharmacokinetics measurements was collected using retro-orbital bleeds with 15 µL glass capillary collection tubes. Blood was diluted in 40 µL phosphate buffered saline (PBS) with 5 mM ethylenediaminetetraacetic acid (EDTA) to prevent clotting, centrifuged for 5 min at 5,000 x g, and fluorescent reporter concentration was quantified in 384-well plates relative to standards (LICOR Odyssey) (fig. 2.S9C).

For immunohistochemical visualization of nanoparticles following IT administration, EZ-Link NHS-Biotin (Thermo Scientific) was coupled to PEG-8_{40kDa}-amine at a 2:1 molar ratio and reacted overnight, followed by spin filtration (Amicon Ultra centrifugal filter units, Sigma). Pulmonary delivery of PEG-8_{40kDa}-biotin (50 µl volume, 10 µM concentration) was performed by intratracheal instillation (Fig. 2.4D-E) or aerosolization (fig. 2.S8C-F). Fixation was performed 10-30 minutes later by inflating lungs with 10% formalin. Lungs were excised, fixed in 10% formalin at 4°C overnight, and embedded in paraffin blocks. 5 µm tissue slices were stained for biotin using the streptavidin-HRP ABC kit (Vector Labs) with 3,3′-Diaminobenzidine (DAB). Slides were scanned using the 20x objective of the Pannoramic 250 Flash III whole slide scanner (3DHistech).

In vitro aerosolization studies

Analysis of nanoparticle stability and protease cleavage susceptibility following aerosolization used 0.1 µm-filtered 250 µM PEG-8_{40kDa} scaffold (fig. 2.S7B-E) or 5 µM PPQ5 PEG-8_{40kDa} nanosensors (fig. 2.S7F). Protease cleavage assays of aerosolized nanoparticles used 50 nM of recombinant human MMP13 (Enzo).

Toxicity studies

Activity-based nanosensor constructs (GluFib-Substrate-PEG-8_{40kDa}) were synthesized by CPC Scientific. Activity-based nanosensors were dosed (50 µL total volume, 20 µM concentration per nanosensor in mannitol buffer (0.28 M mannitol, 5 mM sodium phosphate monobasic, 15 mM sodium phosphate dibasic, pH 7.0-7.5)) by intratracheal instillation into healthy male C57BL/6 mice. The mass of each mouse was monitored for 11 days post-administration and compared with masses of control mice administered mannitol buffer. Heart, lung, liver, spleen, and kidney tissues were collected from the mice at 2 h, 24 h, or 11 days post-administration, fixed in 10% formalin,

paraffin embedded, stained with haematoxylin and eosin, and then examined by a veterinary pathologist (Dr. Roderick Bronson).

Clearance studies

VT750-NHS Ester (PerkinElmer) was coupled to 8-arm 40 kDa PEG-amine (PEG-8_{40kDa}-amine, JenKem) at a 4:1 molar ratio, reacted overnight, and purified by spin filtration (Amicon Ultra centrifugal filter units, Sigma). Mice were lightly anesthetized via isoflurane inhalation, and PEG-8_{40kDa}-VT750 (50 µl volume, 20 µM concentration by VT750 absorbance) was administered by intratracheal instillation (fig. 2.S5). Animals were sacrificed by CO_2 asphyxiation at the indicated timepoints and organs were removed for imaging (LICOR Odyssey). Organ fluorescence was quantified in Fiji *(75)* by manually outlining organs, using the "Measure" feature, and taking the mean intensity. Kinetic data was fit using nonlinear regression in GraphPad 8.0 (Prism). Lung data was fit to an exponential decay model ($Y=Y_0e^{(-Kt)}$; Y, fluorescence; Y_0, initial fluorescence; K, rate constant; t, time), and all other organ data was fit to a two-phase growth and decay model ($Y=A1e^{(-t/B1)}+A2e^{(-t/B2)}$; Y, fluorescence; t, time; A1/A2/B1/B2, constants).

KP lung adenocarcinoma model

KP tumors were initiated by intratracheal administration of 50 µL of adenovirus-SPC-Cre (2.5 x 10^8 plaque-forming units (PFU) in Opti-MEM with 10 mM calcium chloride ($CaCl_2$)) in male B6/SV129 *Kras*$^{LSL\text{-}G12D/+}$; *Trp53*$^{fl/fl}$ (KP) mice (between 18 and 30 weeks old) under isoflurane anesthesia *(54)*. Control cohorts consisted of age and sex-matched mice that did not undergo intratracheal administration of adenovirus. Tumor growth was monitored by microCT imaging (General Electric) and was scored by a blinded radiation oncologist (Dr. Justin Voog) (table 2.S2) using MicroView (Parallax Innovations). Tumor volumes were calculated by using the ROI sphere/elliptical tool. Tumor-bearing mice and age-matched controls were administered activity-

based nanosensor constructs via intratracheal intubation at 5, 7.5, and 10.5 weeks after tumor induction.

EA lung adenocarcinoma model

Tumors were initiated in male C57BL/6 mice between 6 and 10 weeks old as described previously *(64)*, by intratracheal administration of 50 μL adenovirus expressing the Ad-EA vector (Viraquest, 1.5 x 10^8 PFU in Opti-MEM with 10 mM $CaCl_2$). Control cohorts consisted of age and sex-matched mice that did not undergo intratracheal administration of adenovirus. Tumor-bearing mice and age-matched controls were administered activity-based nanosensor constructs via intratracheal intubation at 5, 7.5, and 10.5 weeks after tumor induction.

Colorectal cancer xenograft model

For xenograft studies, LS174T (ATCC CL-188) cells were cultured in Eagle's Minimal Essential Medium (EMEM, ATCC) supplemented with 10% (v/v) FBS (Gibco) and 1% (v/v) penicillin-streptomycin (CellGro). Cells were passaged and harvested for inoculation when confluence reached 80%. Female NCR nude mice (4-5 weeks, Taconic) were injected bilaterally with 3 x 10^6 LS174T cells, resuspended in Opti-MEM (ThermoFisher), per flank. Ten days after inoculation, tumor-bearing mice and age-matched controls were administered activity-based nanosensor constructs via intratracheal intubation.

Lipopolysaccharide (LPS) model

Lung inflammation was induced in 18 to 20 week-old male C57BL/6 mice via intratracheal administration of 0.3 mg of LPS (Sigma Aldrich) in 50 μl water, under isoflurane anesthesia. LPS-treated mice and age and sex-matched healthy controls were administered activity-based nanosensors 3 days after LPS induction.

In vivo characterization of activity-based nanosensors

All activity-based nanosensor experiments were performed in the morning and in accordance with institutional guidelines. Nanosensors (GluFib-Substrate-PEG-8_{40kDa}) for urinary experiments were synthesized by CPC Scientific. Nanosensors were dosed (50 μL total volume, 20 μM concentration per nanosensor) in mannitol buffer (0.28 M mannitol, 5 mM sodium phosphate monobasic, 15 mM sodium phosphate dibasic, pH 7.0-7.5) by intratracheal intubation, as described above, immediately followed by a subcutaneous injection of PBS (200 μl) to increase urine production. Bladders were voided 60 minutes after nanosensor administration, and all urine produced 60-120 min after administration was collected using custom tubes in which the animals rest upon 96-well plates that capture urine. Urine was pooled and frozen at -80°C until analysis by LC-MS/MS.

LC-MS/MS reporter quantification

LC-MS/MS was performed by Syneos Health using a Sciex 6500 triple quadrupole instrument. Briefly, urine samples were treated with ultraviolet (UV) irradiation to photocleave the 3-Amino-3-(2-nitro-phenyl)propionic Acid (ANP) linker and liberate the Glu-Fib reporter from residual peptide fragments. Samples were extracted by solid-phase extraction and analyzed by multiple reaction monitoring by LC-MS/MS to quantify concentration of each Glu-Fib mass variant. Analyte quantities were normalized to a spiked-in internal standard and concentrations were calculated from a standard curve using PAR to the internal standard. Mean normalization was performed on PAR values to account for mouse-to-mouse differences in activity-based nanosensor inhalation efficiency and urine concentration.

2.5 Acknowledgments

We thank J.S. Dudani for assistance with experimental design; R. Zhao and M. Anahtar for technical assistance; A. Mancino (Syneos Health) for performing mass spectrometry; and the Koch Institute Swanson Biotechnology Center, specifically the Bioinformatics & Computing core, the Histology core, and the Preclinical Modeling, Imaging, and Testing core.

2.6 Author contributions

Jesse D. Kirkpatrick (J.D.K.), Andrew D. Warren (A.D.W.), and Sangeeta N. Bhatia (S.N.B.) initiated and designed the study. J.D.K., A.D.W., and Ava P. Soleimany (A.P.S.) performed experiments. A.P.S. and J.D.K. performed statistical analysis. Peter M.K. Westcott (P.M.K.W.) generated animal models. Justin C. Voog (J.C.V.) performed microCT analysis. J.D.K. and Carmen Martin-Alonso (C.M.-A.) performed transcriptomic analysis. S.N.B., Tyler Jacks (T.J.), Heather E. Fleming (H.E.F.), and Tuomas Tammela (T.T.) supervised the research. J.D.K., A.D.W., and S.N.B. wrote the first draft of the manuscript. H.E.F. assisted in the preparation of the manuscript. All authors contributed to writing and editing subsequent drafts of the manuscript and approved the final manuscript.

This chapter references material from:

J. D. Kirkpatrick*, A. D. Warren*, A. P. Soleimany*, P. M. K. Westcott, J. C. Voog, C. Martin-Alonso, H. E. Fleming, T. Tammela, T. Jacks, S. N. Bhatia, Urinary detection of lung cancer in mice via noninvasive pulmonary protease profiling. *Sci. Transl. Med.* **12**, eaaw0262 (2020).
*: Equal contribution

CHAPTER 3. REAL-TIME MONITORING OF DRUG RESPONSE IN PULMONARY DISEASES

3.1 Introduction

Quantitative biomarkers of disease progression and treatment response remain a high priority for both benign and malignant pulmonary diseases. Lymphangioleiomyomatosis (LAM), a rare benign lung disease that primarily affects premenopausal women, is characterized by cystic lung destruction and, ultimately, lung failure *(11)*. Consistent with the role of mTOR in this disease process, rapamycin has emerged as the gold standard treatment modality for patients with LAM *(76, 77)*. However, rapamycin treatment is not curative and is associated with side effects that reduce quality of life *(77, 78)*. New drugs are needed for LAM and several are in clinical trials. Currently, pulmonary function tests, including forced expiration volume in 1 second (FEV_1), are the standard method of monitoring disease burden and response to therapy *(79)*. Unfortunately, FEV_1 is an imperfect biomarker because it is non-quantitative, effort-dependent, and slow to respond to therapy, hindering the pace of clinical trials. Similarly, quantitative biomarkers are need to monitor response to therapy in lung cancer. Currently, the gold-standard modality for monitoring drug response in lung cancer is computed tomography (CT). However, with the exception of oncogene-addicted cancers treated with targeted therapy, response rate by CT does not reliably correlate with overall survival *(10)*. This is especially problematic in patients treated with immunotherapy, who often experience a paradoxical increase in tumor size, likely due to infiltration of immune cells *(10)*.

Given the limitations of existing tools for monitoring drug response in lung disease, various additional blood biomarkers and imaging tools have been explored. Serum VEGF-D levels are increased in most patients with LAM *(12)* and were found to decrease significantly after treatment with rapamycin in the Multicenter International Lymphangioleiomyomatosis Efficacy and Safety

of Sirolimus (MILES) trial *(12, 77)*. Unfortunately, VEGF-D response at 6 months did not correlate with FEV_1 response at 12 months, suggesting that VEGF-D concentrations may not accurately reflect clinical response in LAM patients. Because of the limitations of VEGF-D, additional biomarkers that are predictive of clinical response have been pursued in LAM. A recent study revealed 32 circulating biomarkers, including VEGF-D, that changed significantly in the serum of LAM patients treated with a combination of rapamycin and hydroxychloroquine *(80)*. However, no analyte changes by week 3 of treatment were found to correlate with FEV_1 changes over the 24-week study duration, again suggesting that serum biomarkers do not accurately predict clinical response to treatment in patients with LAM. Finally, high resolution computed tomography (HRCT), the gold-standard diagnostic modality in LAM, has been investigated as a candidate tool for monitoring therapeutic response *(81)*. However, initial evidence suggests that cysts do not change in response to rapamycin treatment, raising doubts about the value of serial monitoring of LAM patients with CT. In lung cancer, the most promising non-imaging candidate biomarker for monitoring treatment response is circulating tumor DNA (ctDNA) *(10)*. ctDNA has been shown to correlate with tumor burden in the context of lung cancer treatment response and tumor progression *(10)*. Furthermore, ctDNA can enable noninvasive mutational profiling, allowing for the discovery of new mutations that may arise in response to therapy. However, ctDNA-based tests are limited by sensitivity, as a large proportion of cancer patients have undetectable levels of ctDNA in the blood *(10, 17)*.

Instead of relying on correlative blood biomarkers or imaging methods, our group has developed a new class of diagnostic nanoparticles, termed “activity-based nanosensors”, that directly read out disease activity *in vivo (35, 41, 82)*. Short, 8-12mer peptide substrates are conjugated to a nanoparticle and administered into the body. Upon cleavage of peptide substrates by dysregulated proteases at the disease site, barcoded products are cleared into the urine, where

they can be detected by mass spectrometry (MS). By appending each substrate with a unique reporter, multiple substrates can be tested simultaneously. We have sought to leverage the unique accessibility of the lungs by leveraging intrapulmonary, rather than intravenous, delivery of activity-based nanosensors to enable disease detection and treatment response monitoring in mouse models of LAM and *Alk*-mutant lung cancer. In both of these models, we found that activity-based nanosensors enabled longitudinal monitoring of disease development and rapid detection of drug response. Collectively, these results support the clinical development of activity-based nanosensors for monitoring progression and treatment response in lung disease.

3.2 Results

Tsc2-deficiency induces protease dysregulation

LAM is driven by neoplastic cells deficient in tuberous sclerosis complex (TSC) 1 or 2 that are thought to grow aberrantly in an unknown primary organ and metastasize to the lung. There, LAM cells aberrantly secrete proteases (predominantly matrix metalloproteinases (MMPs) 2 and 9 and cathepsin K), which are believed to contribute directly to lung degradation and cyst formation *(11)*. We therefore sought to establish a mouse model that captured the protease dysregulation that is characteristic of LAM. We first established a cell line (termed "105K") from a *Tsc2*-null renal tumor that spontaneously formed in a *Tsc2*$^{wt/-}$ mouse. These tumors were found to overexpress MMP2, MMP9, and CTSK relative to normal kidney tissue by immunofluorescence (Fig. 3.1A). Accordingly, we found that 105K cells secreted MMP2 *in vitro* and that expression was significantly abrogated by reintroduction of *Tsc2* ($P = 0.0022$) (Fig. 3.1B). We also observed expression of pro, but not active CTSK in 105K cell lysates, while no CTSK expression was observed in normal mouse kidney or lung lysates (Fig. 3.1C).

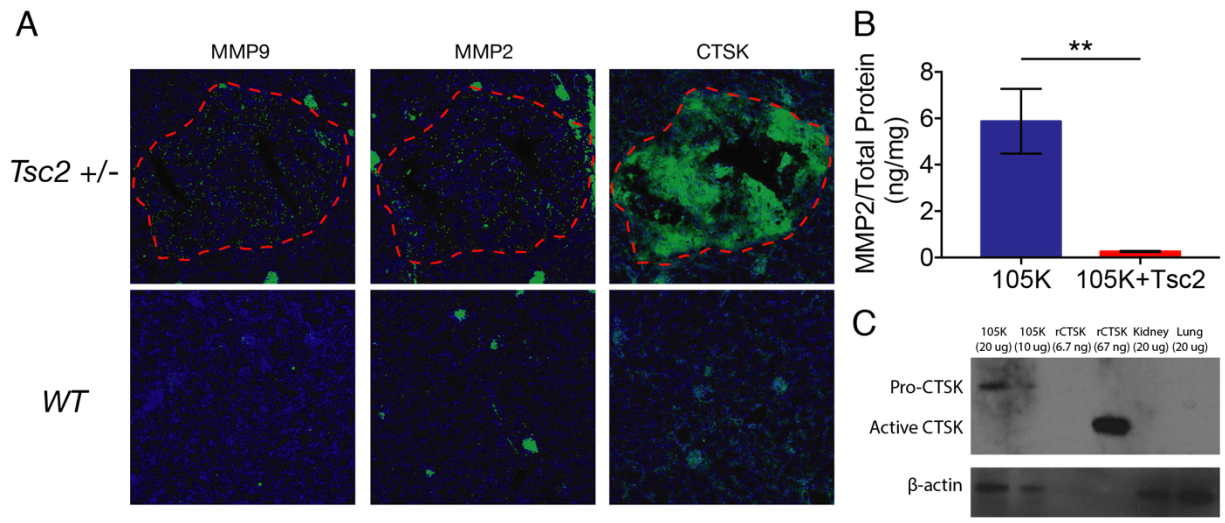

Figure 3.1: *Tsc2* deficiency results in aberrant protease expression. A) Immunofluorescence staining (green) of MMP9, MMP2, and CTSK in lesions (outlined in red) that formed spontaneously in the kidneys of $Tsc2^{wt/-}$ mice (top) compared to kidneys from healthy control mice (bottom). B) Expression of MMP2 in conditioned media from 105K cells and 105K cells with lentiviral reintroduction of *Tsc2*, relative to total protein (n = 3). $^{**}P < 0.01$. C) Western blot against mouse cathepsin K in 105K cell lysates, recombinant mouse cathepsin K, and healthy mouse kidney and lung. β-actin immunostaining is shown for each sample.

Tsc2-null cells are responsive to rapamycin in vitro and in vivo

We then sought to assess responsiveness to rapamycin, the first-line therapy in patients with LAM. We treated 105K cells with rapamycin *in vitro* and found that their growth was slowed in a dose-dependent manner (Fig. 3.2A).

To enable *in vivo* tracking of disease burden, we performed lentiviral transduction of 105K cells with a luciferase expression cassette, performed selection with puromycin, and observed GFP expression in 105K cells *in vitro*. We then performed tail vein injection of $5x10^5$ 105K cells in nude mice and monitored luciferase expression by IVIS. We found that 105K cells seeded the lungs and formed tumors, as assessed by IVIS (Fig. 3.2B). To assess the efficacy of rapamycin *in vivo*, we treated mice with rapamycin (1 mg/kg) either immediately after 105K cell inoculation ("Early Rap") or 20 days after inoculation ("Late Rap"). We observed no disease in mice treated with rapamycin at day 0 and almost complete regression of disease within 8 days in mice treated at day 20 (Fig. 3.2C-D).

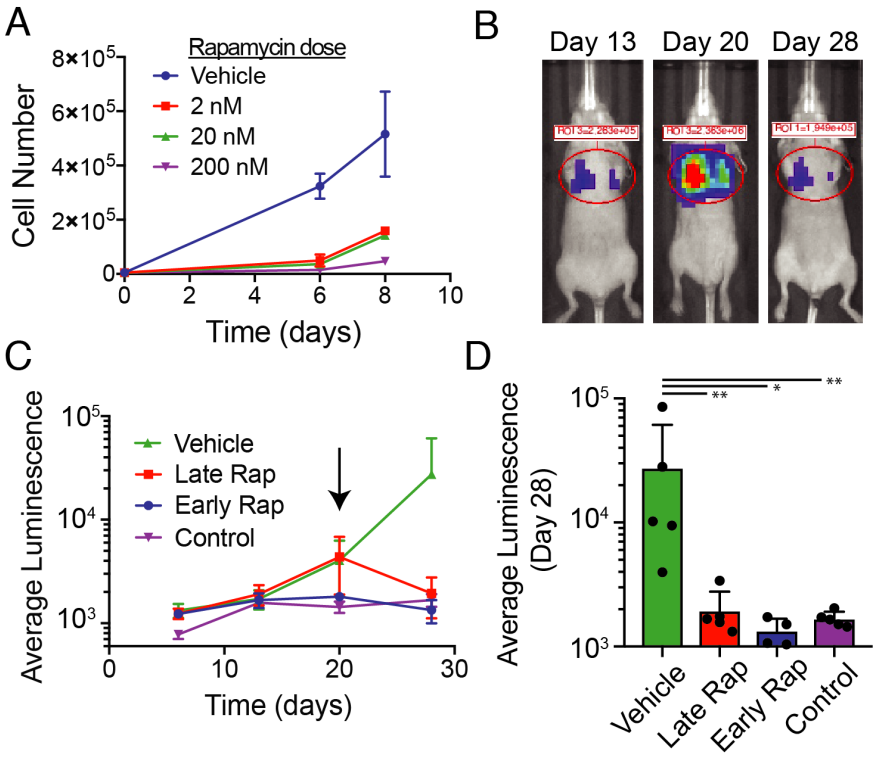

Figure 3.2: LAM cells are responsive to rapamycin in vitro and in vivo. A) Cell growth over time is shown for 105K cells treated with various doses of rapamycin or vehicle (ethanol) (n = 2 each time point). B) Representative IVIS images of LAM mice treated with 1 mg/kg rapamycin 20 days after intravenous injection of 105K cells. C) Quantification of lung luminescence in healthy control mice ("Control"), LAM mice treated with vehicle from day 20 ("Vehicle"), rapamycin from day 20 ("Late Rap"), or rapamycin from day 0 ("Early Rap") (n = 4 to 5 per group). Arrow denotes the time at which rapamycin was initiated in the "Late Rap" group. D) Quantification of lung luminescence at day 28. $*P < 0.05$, $**P < 0.01$ by Mann-Whitney test. Error bars are SD.

Activity-based nanosensors detect dysregulated pulmonary protease activity, enabling detection of LAM in mice

Having established a mouse model of LAM, assessed its responsiveness to rapamycin, and characterized its proteolytic landscape, we next sought to develop activity-based nanosensors tuned to detect these proteases. We first selected a panel of peptide substrates that we had previously found to be cleavable by proteases across multiple classes, and had enabled detection of lung cancer in two autochthonous mouse models *(82)*. To enable multiplexed protease activity measurement *in vivo*, each of these 14 substrates were uniquely labeled a mass-encoded reporter

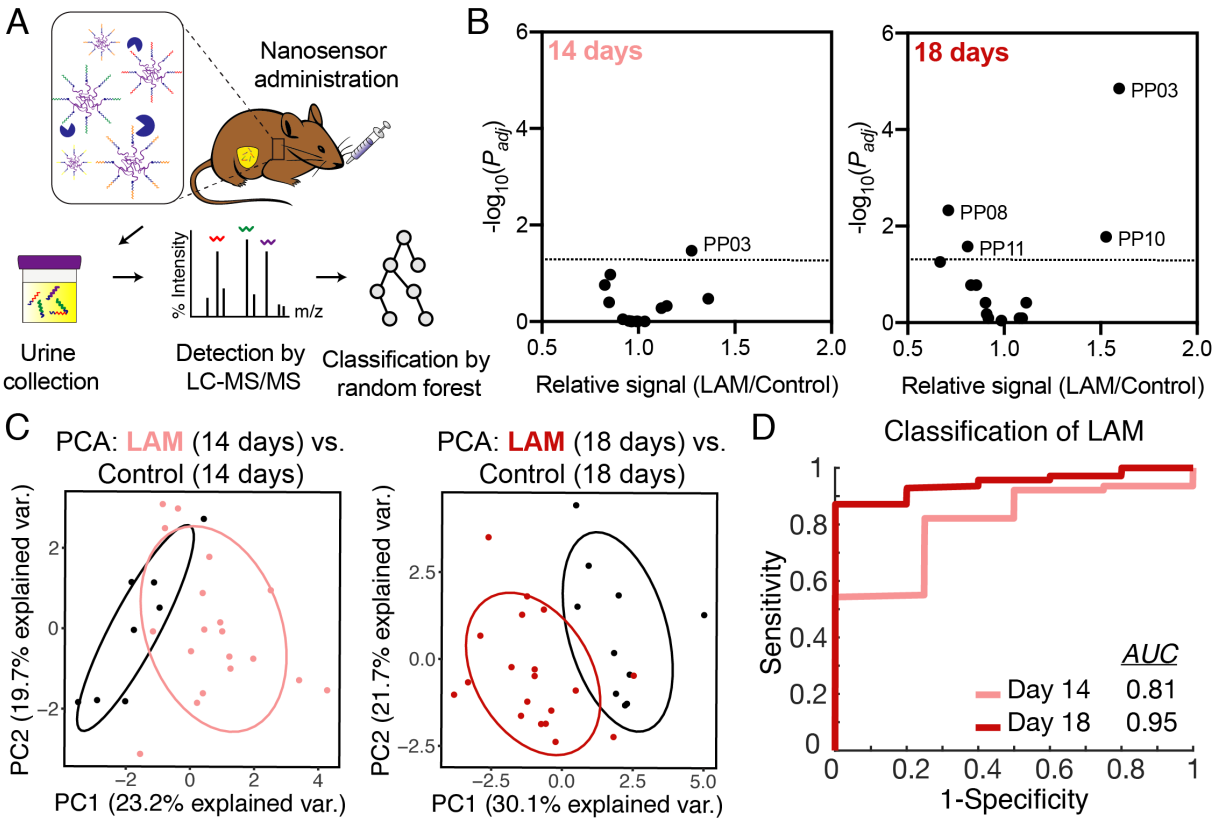

Figure 3.3: Activity-based nanosensors discriminate LAM mice from healthy controls. A) Schematic of approach. B) Mean normalized urinary reporter concentrations in LAM mice and healthy controls were compared at 14 days (LAM: n = 19; Control: n = 9) and 18 days (LAM: n = 19; Control: n = 10) after disease induction and -$\log_{10}(P_{adj})$ was plotted against fold change between LAM and control. Significance was calculated by two-tailed t-test followed by adjustment for multiple hypotheses with Holm-Sidak correction. Dotted line is at P_{adj} = 0.05. C) PCA of urinary reporter output of LAM mice and healthy controls at 14 days and 18 days after disease induction. D) A random forest classifier was trained on urinary reporters from a subset of LAM mice and healthy controls at both 14 and 18 days. ROC curves show performance of this classifier in discriminating LAM mice from healthy controls in an independent test cohort.

molecule and conjugated to 40 kDa 8-arm poly (ethylene glycol) nanoparticles, as previously described *(82)*. This 14-plex nanosensors panel was then administered by intratracheal instillation in LAM mice 14 days and 18 days after disease induction (Fig. 3.3A). All urine produced from 1 to 2 hours after nanoparticle administration was collected and mass spectrometry was performed. At 14 days, we observed significantly increased pulmonary protease activity against a single nanosensor, PP03, in LAM mice relative to healthy controls (P_{adj} = 0.034) (Fig. 3.3B, left). Intriguingly, at 18 days, cleavage of PP03 was further increased in LAM mice (P_{adj} = 1.4x10^{-5})

and PP10 cleavage was also significantly increased (P_{adj} = 0.017) (Fig. 3.3B, right). On the basis of these differentially cleaved nanosensors, we observed separation of LAM and healthy mice by unsupervised dimensionality reduction with principal component analysis (PCA) at both tested time points (Fig. 3.3C). Finally, we trained a random forest classifier using a subset of LAM mice and healthy controls at both time points and tested its ability to accurately classify mice in an independent cohort. We found that the classifier distinguished LAM mice from healthy controls as early as day 14 (AUC = 0.81) and that classification was nearly perfect at 18 days (AUC = 0.95) (Fig. 3.3D). Our results suggest that activity-based nanosensors can measure disease-specific protease dysregulation in a mouse model of LAM, enabling accurate disease detection.

Activity-based nanosensors enable rapid treatment response monitoring in LAM

Though FEV_1 is the gold standard for assessing treatment response in LAM, this metric is effort-dependent and suffers from long lag times that limit its clinical utility. We therefore sought to assess whether activity-based nanosensors could enable objective, quantitative, and, most importantly, rapid assessment of treatment response in LAM. We therefore began treating LAM mice with rapamycin 18 days after disease induction and monitored their pulmonary protease activity with activity-based nanosensors at both day 20 and day 26, 2 and 8 days after rapamycin induction, respectively. We found that both PP10 and PP03 returned to baseline within just two days after treatment induction (P_{adj} = N.S. from control) (Fig. 3.4A). Intriguingly, we also observed a transient increase above baseline in cleavage of PP04 (P_{adj} = 0.0012 from control) and PP13 (P_{adj} = 0.0042 from control) after rapamycin treatment (Fig. 3.4A). Overall, the cleavage of 9/14 nanosensors was significantly altered by treatment with rapamycin, suggesting a profound shift in the pulmonary proteolytic landscape (Fig. 3.4B). By PCA, we observed that nanosensor cleavage patterns in LAM mice became progressively more distinct from healthy controls during disease

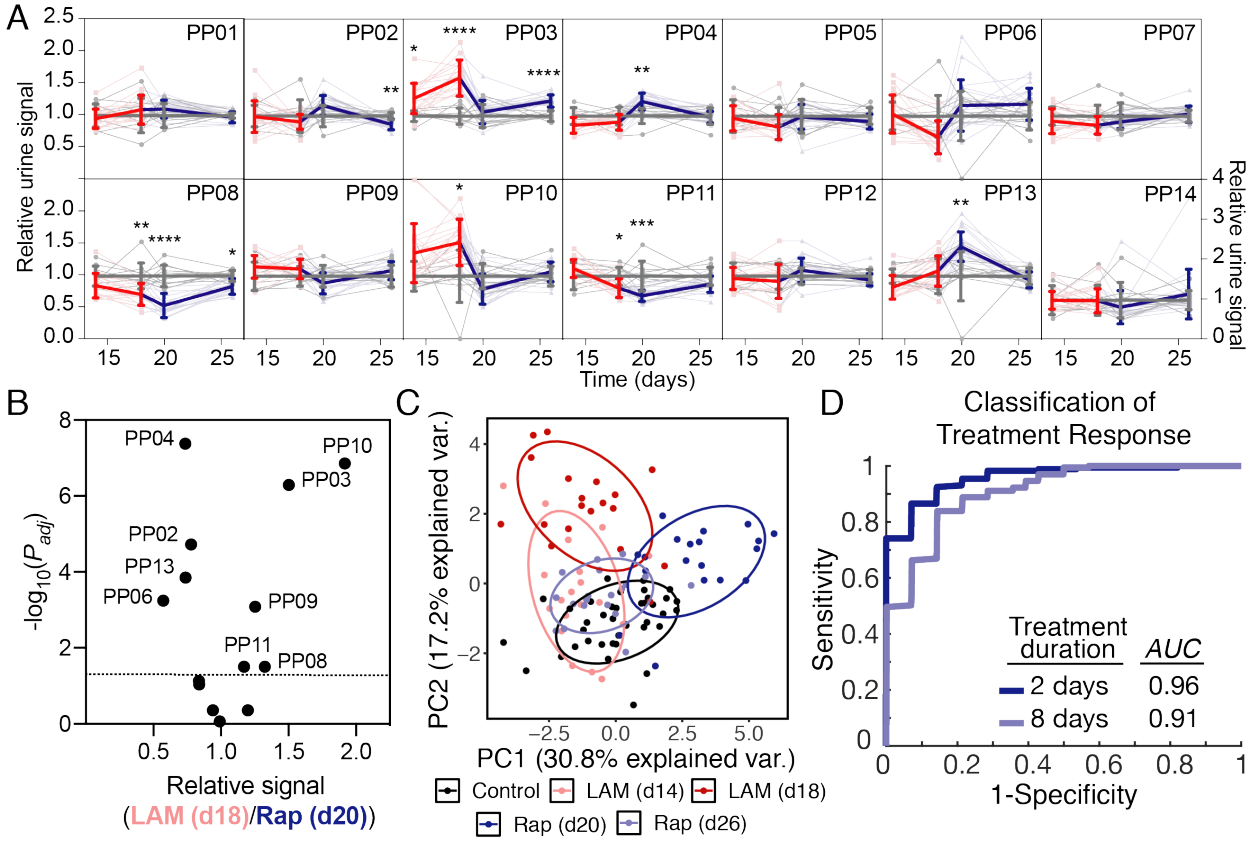

Figure 3.4: Activity-based nanosensors enable rapid assessment of drug response in LAM. A) Control-normalized urinary reporter signal for each of the 14 ABNs. Transparent lines show ABN trajectories of each mouse over time, while opaque lines are averages over all mice. Red lines represent LAM mice prior to rapamycin treatment and blue lines represent LAM mice treated with 3 mg/kg rapamycin (3-4 times per week). Grey lines represent healthy control mice. *$P < 0.05$, **$P < 0.01$, ***$P < 0.001$, ****$P < 0.0001$ from control. Error bars are SD. For clarity, PP14 is presented on a larger scale y axis. B) Volcano plot showing the significance ($-\log_{10}P_{adj}$) and fold change of each urinary reporter in LAM mice 18 days after 105K cell injection ("LAM (d18)") relative to LAM mice after 2 days of rapamycin treatment ("Rap (d20)"). Dotted line is at $P_{adj} = 0.05$. C) Mean normalized urinary reporter concentrations were normalized to matched controls at each time point and subjected to PCA. D) A random forest classifier was trained on urinary reporters from a subset of LAM mice at d18 and rapamycin-treated mice at both 20 and 26 days (2 days and 8 days after rapamycin initiation, respectively). ROC curves show performance of this classifier in discriminating rapamycin-treated mice from untreated LAM mice in an independent test cohort.

progression, but gradually became more similar to controls after rapamycin treatment (Fig. 3.4C). Finally, we trained a random forest classifier using a subset of LAM mice at day 18 and rapamycin-treated mice at days 20 and 26 and tested its ability to accurately classify treated mice in an independent cohort. We found that the classifier accurately detected treatment response at both

tested time points, with the strongest classification just two days after treatment induction (*AUC* = 0.96) (Fig. 3.4D).

Protease activity is dysregulated in an Alk-mutant model of lung adenocarcinoma

Lung adenocarcinoma in humans is frequently driven by mutations in receptor tyrosine kinases, including ALK. To model these mutations in mice, we selected a recently described model (Eml4-Alk, or EA) in which intrapulmonary administration of adenovirus encoding two short guide RNAs (sgRNAs) and Cas9 results in translocation and fusion of the *Eml4* and *Alk* genes, yielding lung adenocarcinoma that histologically resembles human disease *(64)*. We analyzed a recent gene expression dataset that revealed differential expression of multiple protease and protease inhibitor genes in EA tumors relative to healthy lungs *(83)*, suggesting that protease activity was significantly dysregulated downstream of oncogenic ALK signaling (Fig. 3.5).

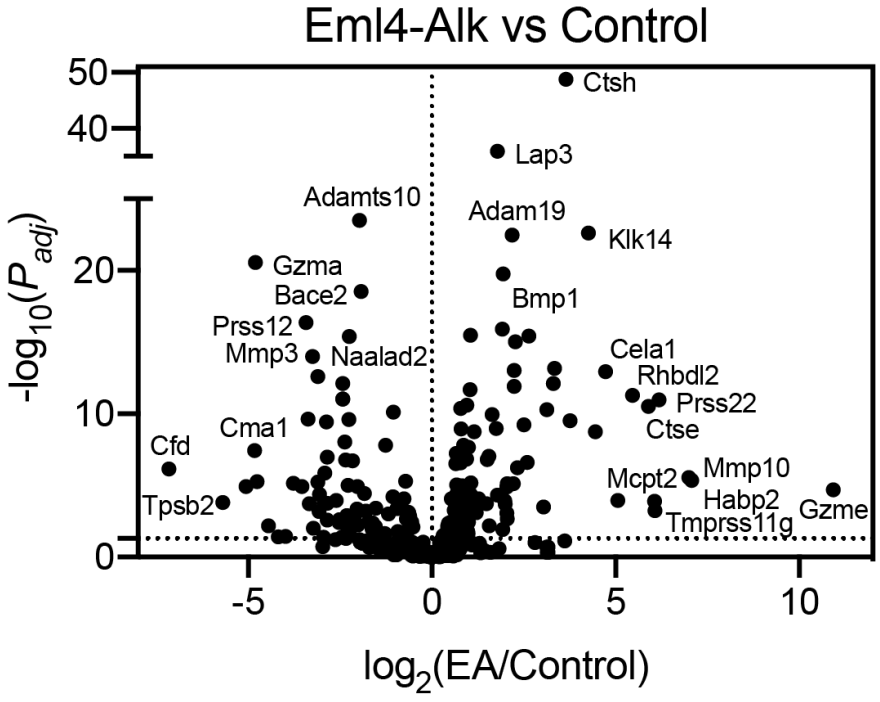

Figure 3.5: Multiple proteases are differentially expressed in *Alk*-mutant lung tumors. An existing RNA-Seq dataset profiling EA tumors *(83)* was analyzed for differentially expressed protease genes using the DESeq2 library. $\log_2$ fold change between EA tumors and healthy lungs is plotted against $-\log_{10}(P_{adj})$ for each protease gene.

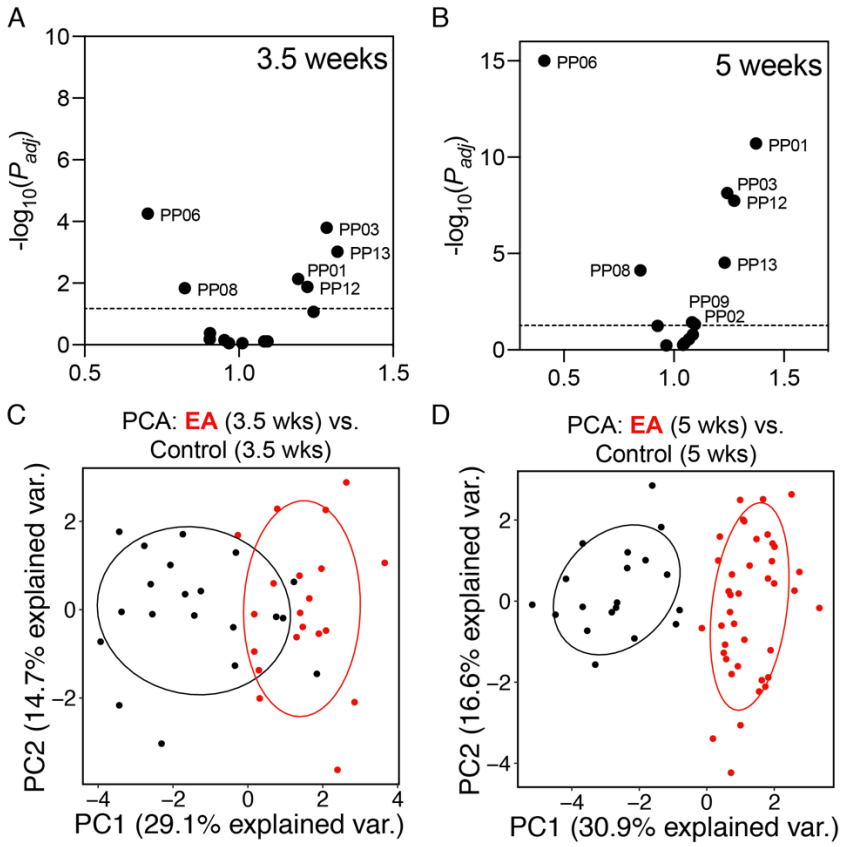

Figure 3.6: Activity-based nanosensors detect dysregulated protease activity in *Alk*-mutant lung cancer. A-B) Mean normalized urinary reporter concentrations in EA mice and healthy controls were compared at 3.5 weeks (EA: $n = 20$; Control: $n = 20$) (A) and 5 weeks (EA: $n = 40$; Control: $n = 19$) (B) after tumor induction and $-\log_{10}(P_{adj})$ was plotted against fold change between EA and control. Significance was calculated by two-tailed *t*-test followed by adjustment for multiple hypotheses with Holm-Sidak correction. Dotted line is at $P_{adj} = 0.05$. C-D) PCA of urinary reporter output of EA mice and healthy controls at 3.5 weeks (C) and 5 weeks (D) after tumor induction.

Activity-based nanosensors enable detection of Alk-mutant lung adenocarcinoma

To enable multiplexed detection of protease activity *in vivo*, we performed intratracheal instillation of the 14-plex activity-based nanosensor panel in EA mice and healthy controls 3.5 weeks and 5 weeks after adenoviral induction and collected all urine generated between 1 and 2 hours after administration. We found that at 3.5 weeks ($EA_{3.5wks}$) and 5 weeks (EA_{5wks}) after tumor induction, 6 and 8 nanosensors, respectively were differentially cleaved by pulmonary proteases in EA and healthy control mice (Fig. 3.6A-B). All 6 of the significantly different sensors in $EA_{3.5wk}$ mice remained significant in EA_{5wk} mice, demonstrating the reproducibility of activity-based

nanosensors and suggesting persistent mutant ALK signaling over time. The most significantly enriched reporters in EA urine at both time points corresponded to nanosensors that were primarily cleaved by metalloproteases in vitro *(82)*, suggesting increased pulmonary metalloprotease activity downstream of oncogenic ALK signaling. In contrast, the two reporters that were most significantly decreased in EA urine were cleaved exclusively by serine proteases in vitro *(82)*. PCA revealed separation of disease and healthy mice at both tested time points (Fig. 3.6C-D)

Monitoring of drug response in Alk-mutant lung adenocarcinoma

To test the hypothesis that pulmonary protease dysregulation in the EA model was driven by oncogenic ALK signaling, we treated mice with alectinib, which specifically inhibits ALK and has emerged as the first-line targeted therapy for patients with *ALK*-mutant lung adenocarcinoma *(84, 85)*. We began daily oral gavage of alectinib or vehicle in EA_{5wk} mice and monitored pulmonary protease activity via intratracheal instillation of activity-based nanosensors at 5.5 weeks, 6 weeks, and 7 weeks after disease induction, or 3 days, 1 week, and 2 weeks after treatment initiation, respectively.

We found that alectinib treatment dramatically altered pulmonary protease activity within 3 days after treatment initiation, with some disease-associated probes like PP01 returning to baseline levels (Fig. 3.7A). Additionally, we observed transiently increased cleavage of PP04 in alectinib-treated mice, mirroring observations made in rapamycin-treated LAM mice (Fig. 3.4A). Unsupervised clustering by principal component analysis (PCA) revealed increased divergence of vehicle-treated mice from healthy controls over time (Fig. 3.7B). In contrast, alectinib treatment resulted in tighter clustering with healthy controls (Fig. 3.7B). Finally we trained a random forest classifier that accurately distinguished pre-treatment from alectinib-treated mice at 3 days, 7 days, and 14 days after initiation of therapy (Fig. 3.7C)

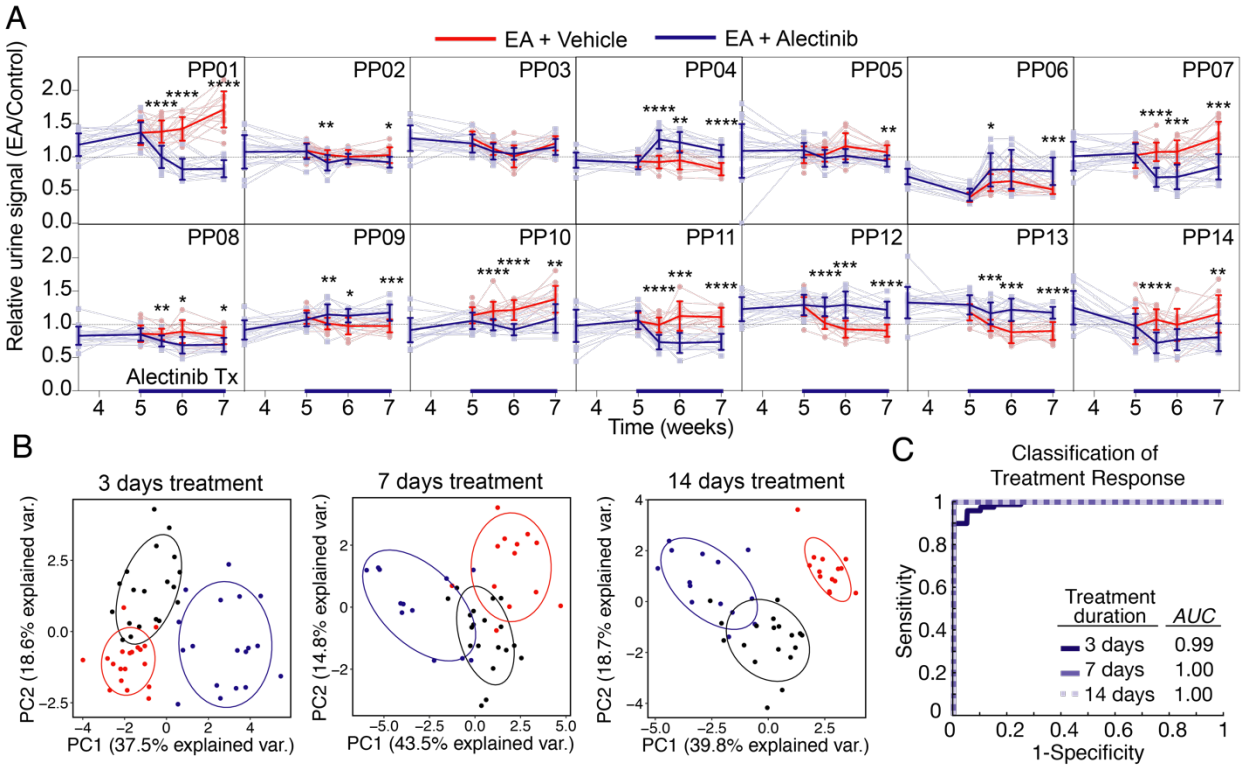

Figure 3.7: Longitudinal monitoring of drug response in *Alk*-mutant lung adenocarcinoma reveals dynamic shifts in the pulmonary protease landscape. A) EA mice were monitored with ABNs during disease development and treatment response with alectinib. Control-normalized urinary reporter signal are shown for each of the 14 ABNs. Transparent lines show ABN trajectories of each mouse over time, while opaque lines are averages over all mice in each treatment group. Red lines represent vehicle-treated EA mice and blue lines represent mice treated with daily alectinib from week 5 after tumor induction. *$P <$ 0.05, **$P < 0.01$, ***$P < 0.001$, ****$P < 0.0001$ between alectinib-treated and vehicle-treated mice. Error bars are SD. B) PCA was performed on mean normalized urinary ABN signals from EA (red), alectinib-treated (blue), and healthy control mice (black) at 3 days (left), 7 days (center) and 14 days (right) after initiation of alectinib treatment. C) ROC curve showing accuracy of a random forest classifier in distinguishing pre-treatment from alectinib-treated EA mice at all three time points.

3.3 Discussion

In this work, we demonstrate the utility of activity-based nanosensors for monitoring progression and treatment response in mouse models of benign and malignant lung disease. In LAM, we found that a multiplexed panel of sensors enabled classification of disease, driven primarily by increased pulmonary protease activity two sensors, PP03 and PP10. Furthermore, we found that this protease activity returned to baseline just two days after treatment initiation, enabling near-perfect classification of treatment response. In *Alk*-driven lung adenocarcinoma, we found that several sensors, including PP01, PP07, and PP10 tracked with tumor burden and that all three returned to baseline within three days after initiation of targeted therapy.

LAM treatment response monitoring via *in vivo* measurements of protease activity offers several advantages over other surrogate endpoints like serum biomarkers, imaging, and clinical response. In LAM, pulmonary protease dysregulation is known to contribute directly to lung degradation, which ultimately results in pulmonary function decline and lung failure *(11)*. Therefore, measuring protease activity at the site of disease may offer the most direct means of assessing disease activity and predicting long-term outcomes. In contrast, biomarkers found in the blood are inherently correlative, as evidenced by the lack of concordance between changes in serum biomarker concentrations and long-term clinical outcomes in patients with LAM *(12)*. Though imaging methods like HRCT enable direct visualization of cyst volume, which correlates with pulmonary function, these findings do not appear to reverse in response to treatment *(86)*. Furthermore, longitudinal monitoring with HRCT is impractical due to expense and risks associated with long-term radiation exposure. Finally, pulmonary function testing is the gold-standard method for determining pulmonary function, but its utility is limited in treatment response monitoring because of technical variability and long lag times *(11)*. Although a clinical study would be necessary to fully validate their utility in predicting functional response, activity-based

nanosensors may offer the most direct and rapidly responsive method of reading out disease activity and treatment efficacy in LAM.

This work also provides proof-of-principle evidence that activity-based nanosensors can enable treatment response monitoring in lung cancer. Management of patients with lung cancer requires accurate and timely information about disease state. CT scanning, the gold standard treatment response monitoring modality, provides only a single snapshot in time and may not accurately reflect true disease burden (for example, in patients treated with immunotherapy) *(10)*. Furthermore, the generalizability of circulating biomarkers like ctDNA is limited by the fact that some patients will have no detectable tumor-derived DNA in the blood. Activity-based nanosensors may represent a new paradigm in lung cancer treatment response monitoring, providing a dynamic readout of disease *activity*, rather than the static snapshots that can be achieved by existing imaging and blood-based diagnostic tools.

Our work also reveals new insights into the biology of disease progression and rapamycin response in our mouse model of LAM. *In vitro*, PP03 and PP10, the two nanosensors preferentially cleaved in LAM mice, are cleaved by napsin A and cathepsin D at low pH *(82)*. Though recent work has revealed a potential role of mTOR-mediated extracellular acidification in LAM *(87)*, this phenomenon has never been directly observed *in vivo*. Notably, we found that treatment with rapamycin resulted in a rapid return to baseline of both PP03 and PP10, consistent with findings that rapamycin treatment inhibits extracellular acidification *(87)*. Finally, we observed transiently increased cleavage of multiple nanosensors following rapamycin treatment. PP04, the sensor with the most significant increase in cleavage following treatment of LAM mice with rapamycin, was also the most significantly increased sensor in EA mice treated with alectinib, suggesting shared mechanisms of drug response in these two models. Though further studies will be necessary to elucidate the mechanism underlying this transiently increased protease activity, our results

highlight the power of activity-based nanosensors to longitudinally monitor disease and treatment-associated biology *in vivo*.

This work establishes activity-based nanosensors as a new paradigm for monitoring progression and treatment response in benign and malignant lung diseases, but several limitations must be addressed prior to clinical adoption. The orthotopic LAM mouse model described here utilized primary *Tsc2*-deficient cells, thereby offering advantages over models that utilized cell lines that were serially passaged through mice to increase aggressiveness *(88)*. However, mouse models cannot fully capture all of the clinical features and heterogeneity of human LAM. Furthermore, though we demonstrate that pulmonary cleavage of activity-based nanosensors rapidly responds to treatment with rapamycin (in LAM) and alectinib (in *Alk*-mutant lung cancer), we did not assess whether these changes corresponded to long-term functional outcomes in our mouse models. Clinical trials will be necessary to assess the utility of activity-based nanosensors in predicting long-term response to therapy. Finally, we delivered activity-based nanosensors via intratracheal instillation, but a clinically compatible delivery method like dry powder inhalation or nebulization will be required for use in humans.

In summary, we have demonstrated the utility of activity-based nanosensors in monitoring progression and treatment response in mouse models of benign and malignant lung disease. Clinically, activity-based nanosensors may enable rapid assessment of treatment response in patients treated with clinically approved (e.g. rapamycin, alectinib) or experimental therapies. By enabling real-time monitoring of disease activity, activity-based nanosensors may dramatically increase the pace of clinical trials and provide accurate and timely information to guide lung disease management.

3.4 Materials and Methods

Immunofluorescence staining

Fresh frozen, OCT-embedded kidneys from *Tsc2*$^{wt/-}$ and WT mice were kindly provided by E. Henske (Brigham and Women's Hospital). Sections were stained with primary antibodies against mouse MMP9 (Abcam, ab137867, 1:250 dilution in block buffer), MMP2 (Abcam, ab37150, 1:200 dilution in block buffer), and CTSK (Abcam, ab19027, 1:250 dilution in block buffer) for 2.5 hours at RT.

ELISA for MMP2

105K cells, a primary line derived from kidney lesions in *Tsc2*$^{wt/-}$ mice, and 105K cells with lentiviral reintroduction of *Tsc2* (105k+Tsc2) were kindly provided by E. Henske. 105K and 105K+Tsc2 cells were cultured in Dulbecco's modified Eagle medium supplemented with 10% fetal bovine serum and 1% penicillin– streptomycin. Secreted levels of MMP2 were measured by ELISA, according to the manufacturer's protocol (R&D Systems). All measurements were normalized to total protein in the supernatant, as assessed by Bradford assay.

Western blot for CTSK

105K cells were lysed in RIPA buffer supplemented with protease inhibitors. Normal kidney and lung were harvested from healthy mice, snap frozen in liquid nitrogen, and subsequently homogenized in ice cold RIPA buffer with protease inhibitors. Recombinant active mouse cathepsin K (Biovision) was used as a positive control. Samples were loaded into NuPAGE Bis-Tris Mini Gels (Invitrogen) and western blot was performed. Membranes were subsequently stained for cathepsin K (ab19027, Abcam, 1:1000 in 5% milk) and β-actin (ab8227, Abcam, 1:1000 in 5% milk).

Rapamycin dose response in 105K cells

105K cells were plated at 5,000 cells/well in 24-well plates and treated with either vehicle or rapamycin (LC Labs) at 2 nM, 20 nM, or 200 nM. Cells were trypsinized and counted at each time point.

In vivo LAM model

To enable longitudinal tracking of disease burden, 105K cells were transduced with a lentivirus encoding for luciferase and a puromycin selection cassette (LP-hLUC-Lv201-0200, Genecopoeia), followed by selection with puromycin (1 ug/mL). To establish an *in vivo* LAM model, female nude mice (3-4 weeks old) were injected intravenously with $5x10^5$ luciferized 105K cells. Disease burden was monitored by subcutaneously administering 100 uL of a 30 mg/mL solution of D-Luciferin (GoldBio) in PBS and performing IVIS imaging 10 to 25 mins later. For *in vivo* administration, rapamycin was prepared in a vehicle containing 0.25% PEG-200 and 0.25% Tween-80. LAM mice were treated with intraperitoneal injections of either rapamycin (1 mg/kg) or vehicle 3-4 times per week and were monitored by IVIS.

In vivo disease monitoring with activity-based nanosensors

All activity-based nanosensor experiments were performed in the morning and in accordance with institutional guidelines. Nanosensors (GluFib-Substrate-PEG-8_{40kDa}) for urinary experiments were synthesized by CPC Scientific. Nanosensors were dosed (50 µL total volume, 20 µM concentration per nanosensor) in mannitol buffer (0.28 M mannitol, 5 mM sodium phosphate monobasic, 15 mM sodium phosphate dibasic, pH 7.0-7.5) by intratracheal instillation, immediately followed by a subcutaneous injection of PBS (200 µl) to increase urine production. Bladders were voided 60 minutes after nanosensor administration, and all urine produced 60-120 min after administration was collected using custom tubes in which the animals rest upon 96-well plates that capture urine. Urine from each mouse was pooled and frozen at -80°C until analysis by LC-MS/MS.

LC-MS/MS reporter quantification

LC-MS/MS was performed by Syneos Health using a Sciex 6500 triple quadrupole instrument. Briefly, urine samples were treated with ultraviolet (UV) irradiation to photocleave the 3-Amino-3-(2-nitro-phenyl)propionic Acid (ANP) linker and liberate the Glu-Fib reporter from residual peptide fragments. Samples were extracted by solid-phase extraction and analyzed by multiple reaction monitoring by LC-MS/MS to quantify concentration of each Glu-Fib mass variant. Analyte quantities were normalized to a spiked-in internal standard and concentrations were calculated from a standard curve using PAR to the internal standard. Mean normalization was performed on PAR values to account for mouse-to-mouse differences in activity-based nanosensor inhalation efficiency and urine concentration.

Statistical analysis

For all urine experiments, PAR values were normalized to nanosensor stock concentrations and then mean normalized across all reporters in a given urine sample before further statistical analysis. To identify differential urinary reporters, all reporters were analyzed by unpaired two-tailed *t* test, followed by correction for multiple hypotheses using the Holm-Sidak method in GraphPad Prism 7.0. $P_{adj} < 0.05$ was considered significant. PCA was performed on mean-normalized PAR values and implemented in R using the ggplot2 package. For disease classification based on urinary activity-based nanosensor signatures, randomly assigned sets of paired data samples consisting of features (the mean-normalized PAR values) and labels (for example, LAM d18 and Rap d20) were used to train random forest classifiers implemented with the TreeBagger class in MATLAB R2019b. Estimates of out-of-bag error were used for cross-validation, and trained classifiers were tested on randomly assigned, held-out, independent test cohorts. Ten independent train-test trials were run for each classification problem, and classification performance was evaluated with ROC statistics calculated in MATLAB. Classifier

performance was reported as the mean accuracy and AUC across the 10 independent trials. RNA-Seq data for the EA model was downloaded from GEO (GSE139347) *(83)*. The list of mouse protease genes was obtained from UniProt. Differential expression analysis was performed using the DESeq2 differential expression library in the R statistical environment.

EA lung adenocarcinoma model

Tumors were initiated in male C57BL/6 mice between 6 and 10 weeks old as described previously *(64)*, by intratracheal administration of 50 μL adenovirus expressing the Ad-EA vector (Viraquest, 1.5 x 10^8 PFU in Opti-MEM with 10 mM $CaCl_2$). Control cohorts consisted of age and sex-matched mice that did not undergo intratracheal administration of adenovirus. Alectinib (MedChemExpress) was prepared in vehicle containing 0.02 N hydrochloric acid, 10% dimethylsulfoxide, 10% Cremophor EL, 15% PEG400, and 15% 2-hydroxypropyl-b-cyclodextrin and sterile filtered with 0.2 um syringe filters prior to *in vivo* administration. Mice were treated with daily oral gavage of alectinib (20 mg/kg) or vehicle.

3.5 Author contributions

Jesse D. Kirkpatrick (J.D.K.) and Sangeeta N. Bhatia (S.N.B.) initiated and designed study components related to LAM. J.D.K., Ava P. Soleimany (A.P.S.), and S.N.B initiated and designed study components related to the Eml4-Alk model. J.D.K. and A.P.S. performed experiments and statistical analysis. Jaideep S. Dudani (J.S.D.) assisted with experimental design related to LAM. Hilaire Lam (H.L.), Tina Liu (T.L.), Carmen Priolo (C.P.), and Elizabeth Henske (E.H.) supplied reagents and assisted with experimental design related to LAM. S.N.B and E.H. supervised the research.

CHAPTER 4. ESTABLISHING AN INTEGRATED PIPELINE TO DEVELOP PROTEASE-ACTIVATED DIAGNOSTICS

4.1 Introduction

Protease activity is dysregulated across multiple disease states, including cancer, fibrosis, and infection. In cancer, matrix metalloproteinases (MMPs) are one of several classes of enzymes known to degrade the extracellular matrix, enabling tumor invasion, neoangiogenesis, and metastasis *(89)*. As a result of this dysregulation, proteases have long been considered as a potential diagnostic and therapeutic target of cancer. The past decade has seen the emergence of new classes of "activity-based" diagnostics *(40, 82, 90–95)* and therapeutics *(96–101)*, which are specifically activated in response to proteases dysregulated in cancer. For example, probodies are a novel class of activity-based therapeutics consisting of a tumor-targeting antibody masked via a protease-cleavable linker *(96)*, which improves tumor specificity and reduces off-target toxicity. Likewise, activity-based diagnostics have demonstrated promise both pre-clinically and clinically, leveraging protease dysregulation in cancer to improve imaging specificity or intraoperative evaluation of tumor margins *(29, 30, 91–93, 102, 103)*. Protease-activated diagnostics and therapeutics typically leverage peptide linkers that are designed to be cleaved by disease-associated proteases. However, development of these technologies is currently hindered by a dearth of methods to dissect protease activity in human disease *(104)*. Recent clinical studies have indicated that masked probodies incorporating such linkers show suboptimal activation efficiency within the tumor microenvironment, further motivating the need for modular tools to profile protease activity *ex vivo* to improve design *(105)*. Therefore, development of protease-responsive diagnostics and therapeutics would be dramatically accelerated by high throughput and modular methods to identify peptide substrates that are maximally cleaved by disease-associated proteases and minimally degraded in off-target tissues. Furthermore, the ability to localize these cleavage

events *in situ* (i.e., in a tissue section) would enable finer dissection of disease-associated protease biology, such as cell type-specific protease dysregulation. Finally, to accelerate translation, these methods must be compatible with clinically-available biospecimens, such as biofluids or biopsy cores.

Several methods have been developed with the aim of measuring protease activity in biospecimens, but these methods generally lack the modularity, spatial resolution, or clinical compatibility to warrant their use in discovering disease-responsive peptide substrates. Proteome-derived substrates have been quantified via mass spectrometry to discover endogenous cleavage products in cell protein extracts *(106–108)* and serum *(109)*. However, this method is limited to the discovery of natural substrates, which cannot be readily translated to protease-activated diagnostics or therapeutics because they may lack specificity, rely on tertiary structure for proper presentation, or suffer from slow cleavage kinetics *(104)*. Recent approaches leveraging synthetic substrates have used droplet-based microfluidics *(110)* or highly multiplexed peptide libraries *(111, 112)* to profile protease activity in patient-derived biospecimens. However, these assays do not provide insight on spatial localization of protease activity within the tissue and have not been shown to directly yield peptides that can be incorporated into activatable diagnostics or therapeutics for *in vivo* use. *In situ* zymography has long been the gold standard for visualizing protease activity in tissue sections *(113)*, but this method is limited to visualizing the activity of proteases against natural cleavage sites in gelatin and therefore lacks the modularity to enable discovery of disease-specific peptide substrates. Activity-based probes (ABPs) leverage reactive warheads that covalently bind to protease active sites, enabling detection of active proteases *in vivo* and *ex vivo (92, 114)*. However, because ABPs detect protease activity via covalent binding rather than substrate cleavage, they are less compatible with proteases of certain catalytic classes,

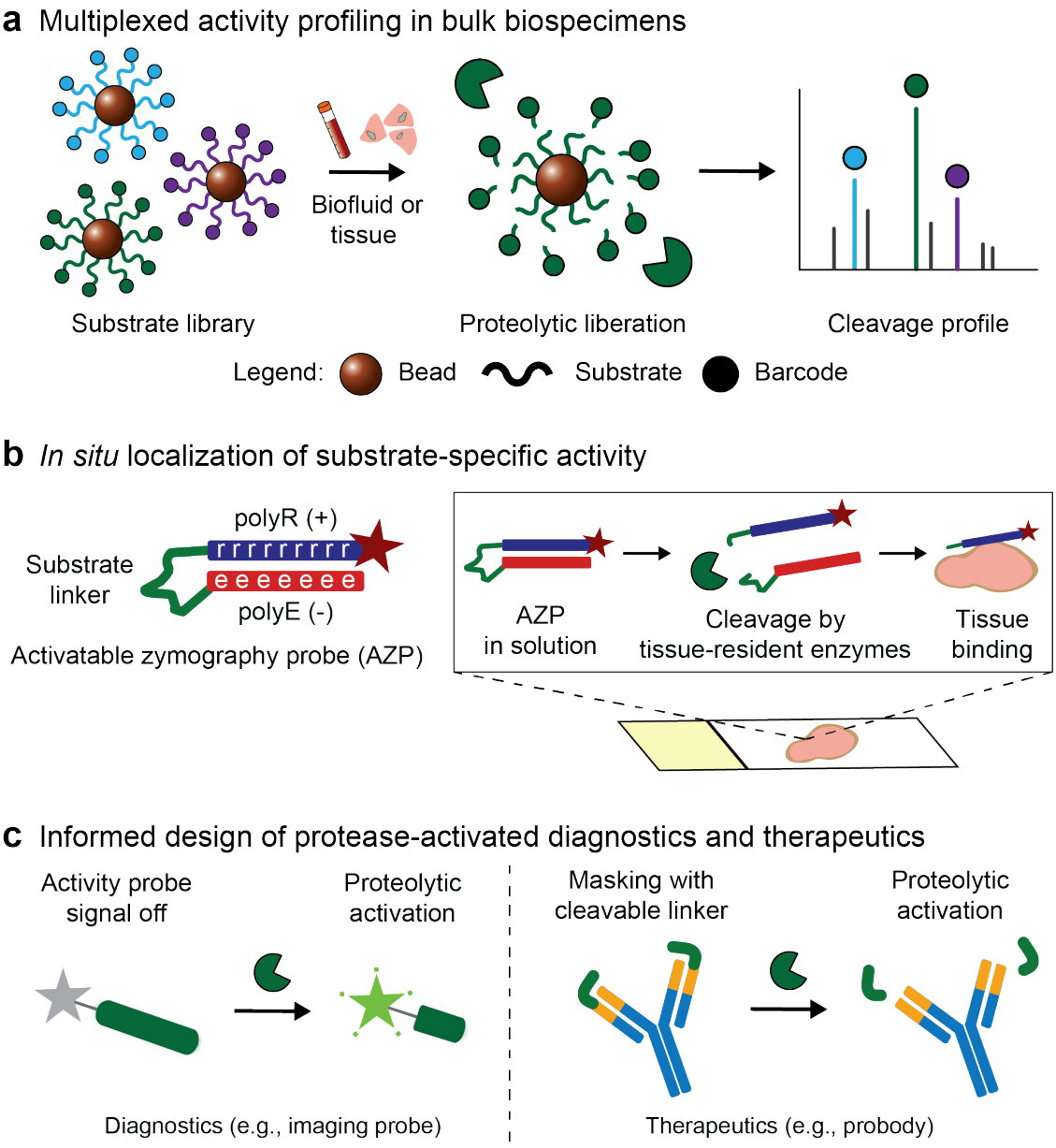

Figure 4.1. Approach and overview. (a) Multiplexed protease activity profiling with barcoded substrate libraries. Uniquely barcoded protease-cleavable peptide substrates are coupled to magnetic beads. Multiplexed bead complexes are incubated with recombinant enzymes or biospecimens. Substrate-specific proteolysis liberates barcodes, which can be isolated via magnetic pull-down of beads and quantified to measure substrate cleavage. (b) Activatable zymography probes (AZPs). AZPs consist of a poly-arginine domain (polyR, blue) carrying a tag (e.g., fluorophore; maroon star) linked to a poly-glutamic acid domain (polyE, red) via a protease-cleavable linker (green). Upon application to frozen tissue sections, AZPs are cleaved by tissue-resident enzymes, liberating the tagged polyR which then binds the tissue. Microscopy enables *in situ* localization of substrate-specific protease activity. (c) Disease-responsive peptide substrates nominated from *ex vivo* activity profiling can be directly incorporated into protease-activated diagnostics, e.g., *in vivo* imaging probes, or therapeutics, e.g., probodies, proteolytically-activated antibodies that require linker cleavage for target binding, for *in vivo* evaluation.

and profiling with ABPs has not been used to identify peptide substrates that can be directly incorporated into activatable diagnostics and therapeutics *(92)*.

We therefore built a modular toolkit to identify and validate disease-responsive peptide substrates (Fig. 4.1, Table 4.S1). To this end, we developed two cleavage-based approaches for measuring protease activity in tissues, including both a multiplexed assay using barcoded synthetic peptide substrates and a modular *in situ* activity assay (Fig. 4.1, Table 4.S1), and applied these methods to prostate cancer (PCa) models and samples. This novel integration of multiplexed substrate screens that nominate lead substrates with cleavage-based zymography assays that validate candidate probes *in situ* presents a new framework relevant to both discovery and engineering efforts that seek to understand and leverage protease dysregulation. To validate our approach, we evaluated the ability of these tools to inform the bottom-up design of protease-activatable agents in a clinically-relevant model of disease. We performed a multiplexed screen and discovered a single peptide that was specifically cleaved by disease-associated proteases in a genetically-engineered mouse model (GEMM) of PCa. This peptide was then translated into an activatable zymography probe (AZP) to localize protease activity *in situ*, and was ultimately incorporated into a protease-activated probe that selectively accumulated in diseased mouse prostates *in vivo*. Together, these assays constitute an integrated toolkit for measuring and localizing protease activity against synthetic peptide substrates directly in biospecimens. In applying our tools to a PCa GEMM, we demonstrate that substrates discovered and validated through these assays can be directly translated into an *in vivo* protease-activated diagnostic, accelerating the design, build, and test cycle. We envision that these methods will facilitate design of protease-activatable diagnostics and therapeutics and advance understanding of protease dysregulation in human disease.

Table 4.S1. Strategies for profiling protease activity *ex vivo*.

Assay type	Sample type	Throughput	Spatial information	Applications
Cleavage of fluorogenic substrates	Recombinant enzymes, tissue homogenates, biofluids	Single probe per reaction volume	No; bulk assay	Measure substrate cleavage kinetics in real time
Pooled screen with barcoded substrates	Recombinant enzymes, tissue homogenates, biofluids	Many probes per reaction volume	No; bulk assay	Identify lead probes from substrate library
In situ localization with AZPs	Fresh frozen tissue sections	Small numbers of probes per tissue	Yes	Characterize lead probes across tissue sections Study protease biology

4.2 Results

Synthetic peptide substrates read out tumor-associated protease activity ex vivo

We first sought to assess whether tumor-associated protease activity could be read out by monitoring the cleavage of synthetic peptide substrates *ex vivo*. As a proof of concept, we established flank xenogafts of two human PCa cell lines, including an aggressive, undifferentiated line (PC3) derived from a bone metastasis and a less aggressive line (22Rv1) derived from a primary tumor. We incubated homogenates of these two xenografts, as well as of healthy mouse prostate, with a panel of quenched fluorescent peptide substrates and measured protease activity by monitoring fluorescence increase over time (Fig. 4.S1a-b). Multiple substrates were differentially cleaved by each of the two xenograft types, relative to normal prostate tissue (Fig. 4.S1c). Further, several substrates exhibited distinct cleavage patterns in homogenates from more (PC3) versus less (22Rv1) aggressive tumors (Fig. 4.S1c), which separated clearly on the basis of

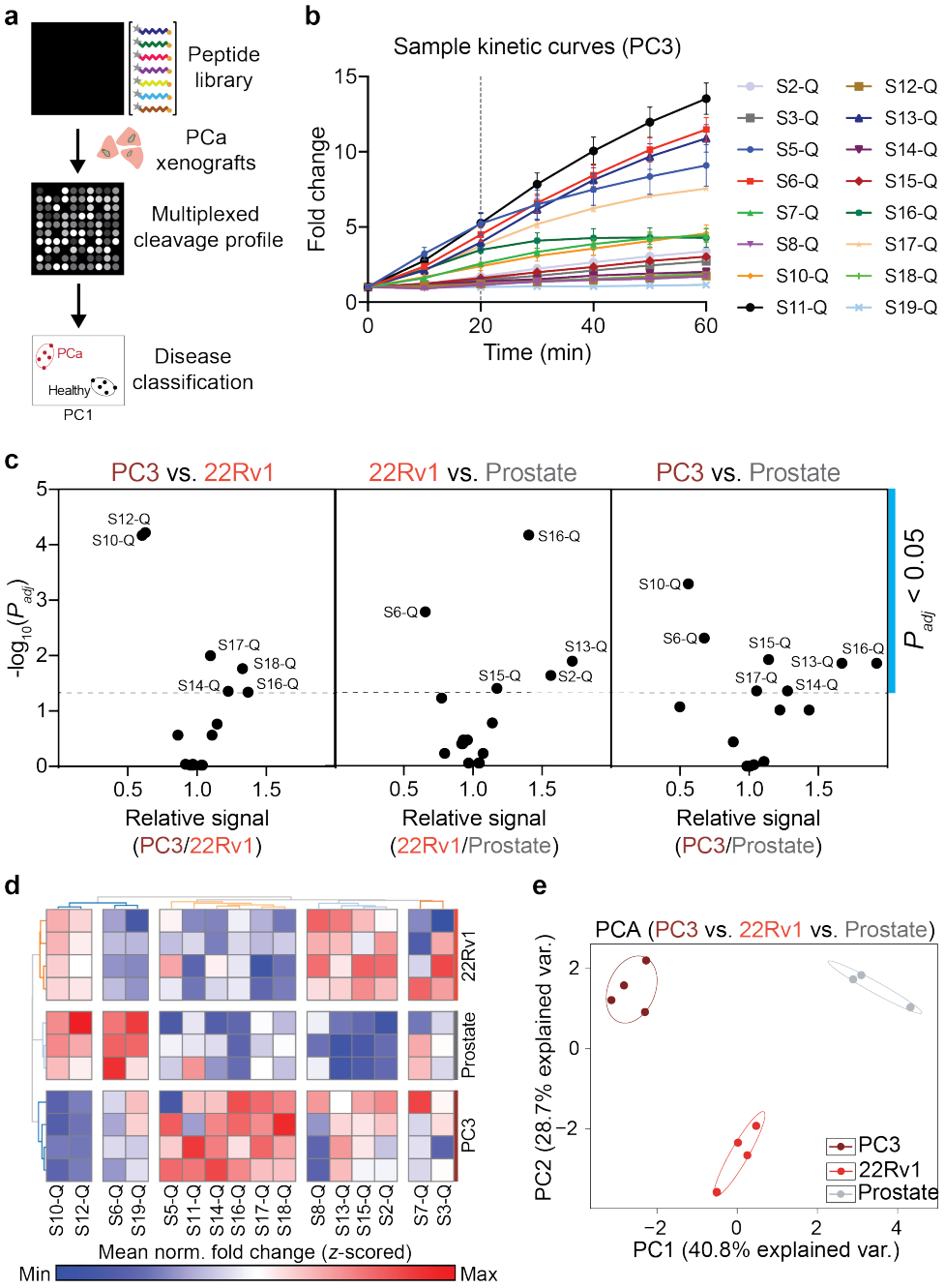

Figure 4.S1. Multiplexed protease activity measurements in tissue specimens enable PCa classification. (a) Schematic of cleavage screen using panel of FRET-paired peptide substrates against homogenates of PC3 xenografts ($n = 4$), 22Rv1 xenografts ($n = 4$), and healthy mouse prostates ($n = 3$). (b) Kinetic fluorescence curves for panel of 16 FRET-paired substrates incubated with PC3 tumor homogenates. Each line represents a distinct substrate ($n = 4$; mean ± s.d.). (c) Fluorescence fold changes after 20 minutes were mean normalized across all peptides for each sample, and two-tailed *t*-test followed by adjustment for multiple hypotheses using the Holm-Sidak method was used to identify peptides that were differentially cleaved between PC3 and 22Rv1 (left), 22Rv1 and healthy prostate (center), and PC3 and healthy prostate (right). $-\log_{10}(P_{adj})$ is plotted as a function of fold change. Dotted line is at $P_{adj} = 0.05$. (d) Hierarchical clustering of *z*-scores of mean normalized cleavage product concentrations (calculated from fluorescence fold changes at 20 minutes) was used to identify distinct substrate cleavage patterns differentiating the three tissue types. (e) PCA of cleavage data in (d).

hierarchical clustering (Fig. 4.S1d) and principal component analysis (PCA) (Fig. 4.S1e) of these cleavage data. Consistent with this activity-based assay, proteomic analysis revealed that the abundance of several proteases (Fig. 4.S2a) and inhibitors (Fig. 4.S2b) were differentially expressed in the two xenografts.

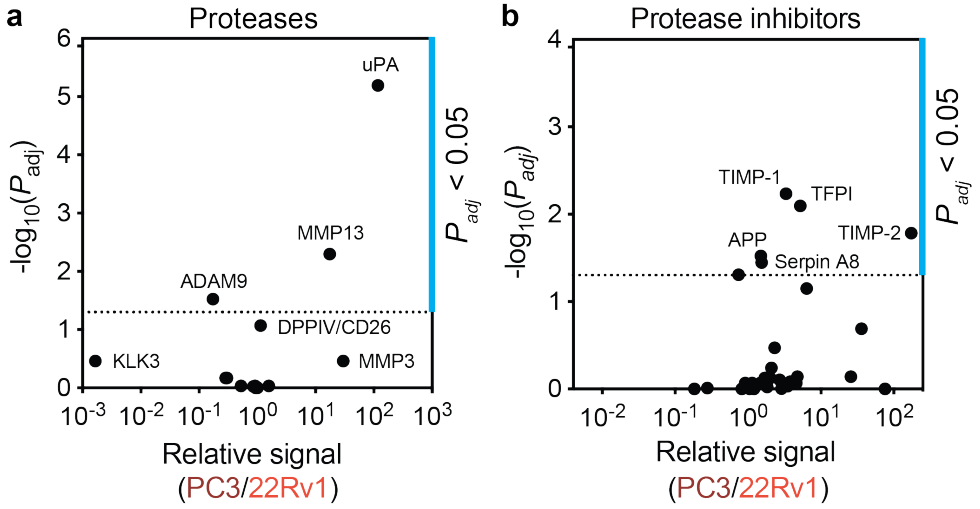

Figure 4.S2. Proteomic profiling in tumor homogenates distinguishes more and less aggressive tumor types. (a, b) Protease (a) and protease inhibitor (b) abundance in homogenates of more (PC3, $n = 3$) and less (22Rv1, $n = 3$) aggressive prostate cancer xenografts was quantified using a multiplex antibody array. Volcano plots show fold changes in analyte abundance between PC3 ($n = 3$) and 22Rv1 ($n = 3$) xenograft homogenates (x-axis) and $-\log_{10}(P_{adj})$ (y-axis). Significance was calculated by two-tailed *t*-test followed by adjustment for multiple hypotheses using the Holm-Sidak method. Dotted line is at $P_{adj} = 0.05$.

Protease specificity mapping with barcoded peptide substrates

Although the fluorescence assay enabled discrimination of PC3, 22Rv1, and healthy prostate homogenates, it required large quantities of analyte and was limited in throughput, as bulk enzyme activity against each substrate was assayed in a separate reaction volume (Table 4.S1). Scalable methods for multiplexed substrate screening in biospecimens could be used to identify lead peptides for eventual incorporation into protease-activated diagnostics and therapeutics.

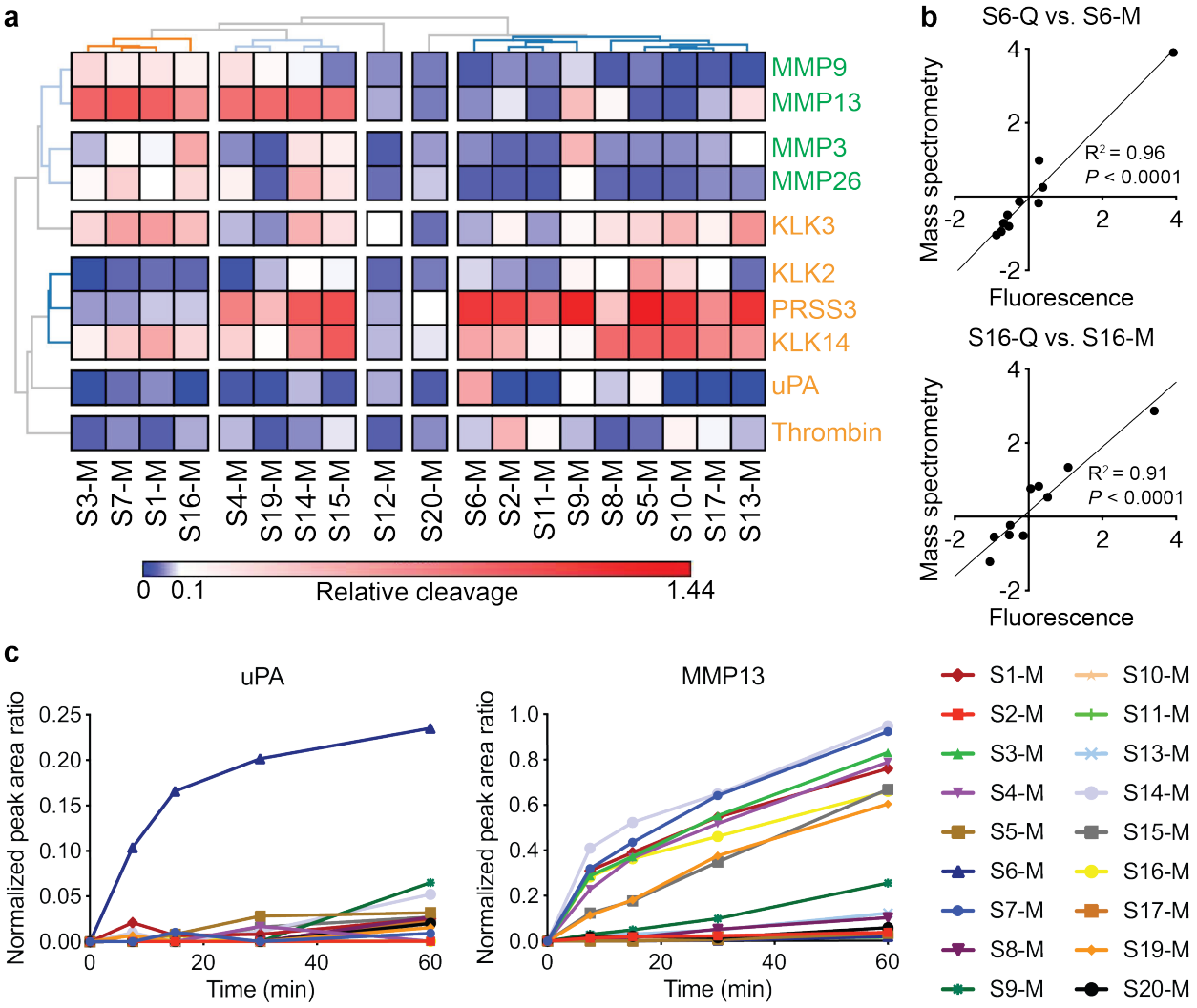

Figure 4.2. Protease activity profiling with barcoded substrate libraries. (a) Heat map showing *in vitro* cleavage of mass-barcoded substrates (x-axis) by selected recombinant proteases (y-axis; metalloproteinases, green; serine proteases, yellow). Cleavage products were quantified by mass spectrometry and unsupervised hierarchical clustering was performed. (b) Correlation of relative substrate cleavage *z*-scores for serine protease substrate S6-Q/S6-M (quenched/mass encoded, respectively) and metalloproteinase substrate S16-Q/S16-M (quenched/mass encoded, respectively), as measured by fluorescence with quenched substrates (x-axis) and mass spectrometry with bead-conjugated substrates (y-axis). (c) Kinetics of substrate cleavage obtained from mass-barcoded library screen for the serine protease uPA (left) and the metalloproteinase MMP13 (right) as representative examples. Kinetics were assessed via quantification of liberated barcodes isolated via magnetic separation at various time points after addition of protease, followed by mass spectrometry quantification. Lines represent means of two technical replicates.

Therefore, we developed a method to measure cleavage of a multiplexed panel of peptides in a single reaction volume, which could eventually be scaled up to enable screening of hundreds or thousands of peptide substrates simultaneously (Fig. 4.1a). As a proof of concept, we selected a panel of 18 peptides previously found by our group to be recognized and cleaved by a diverse array of metallo- and serine proteases that are dysregulated in PCa, *(41)* and appended each peptide with a unique, mass-encoded reporter molecule. We coupled these barcoded substrates to magnetic beads via a non-cleavable poly(ethylene glycol) (PEG) linker and incubated the bead cocktail with each of 10 recombinant proteases to assay their individual cleavage patterns. Beads were pulled down via magnetic separation, and liberated reporter molecules that remained in the supernatant were measured by mass spectrometry, enabling quantification of substrate cleavage by each protease. Unsupervised hierarchical clustering of the cleavage data revealed distinct substrate specificities of the screened metallo- and serine proteases (Fig. 4.2a). Furthermore, we found that the cleavage scores measured through the multiplexed bead screen correlated with those from a screen of fluorescently-quenched versions of the same substrates incubated individually with the same selected collection of recombinant proteases *(41)* (Fig. 4.2b; Fig. 4.S3). Cleavage kinetics were assessed by performing magnetic separation at multiple time intervals following addition of protease and quantifying the liberated reporters by mass spectrometry (Fig. 4.2c; Fig. 4.S4). Taken together, these results indicate that the multiplexed bead assay can be used to faithfully query cleavage specificities and kinetics of target proteases against a barcoded library of peptide substrates.

In situ labeling of protease activity with activatable zymography probes

The multiplexed bead assay can be used to generate substrate specificity maps and to identify peptide substrates cleaved by proteases within a complex matrix, but this method lacks spatial

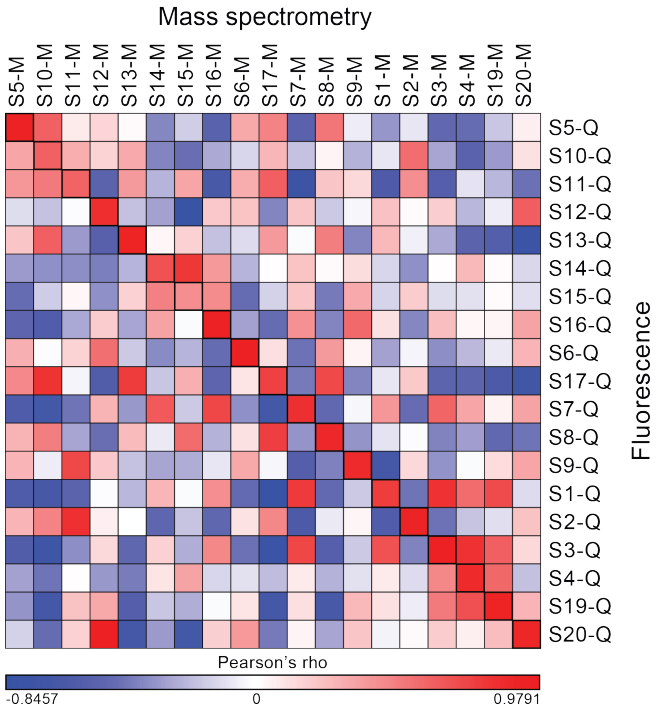

Figure 4.S3. Correlation of cleavage profiles of mass barcoded and FRET-paired peptide substrates. Correlation of FRET-paired free peptide cleavage to mass-barcoded peptides conjugated to the surface of magnetic beads, calculated as Pearson's rho across all proteases using cleavage *z*-scores.

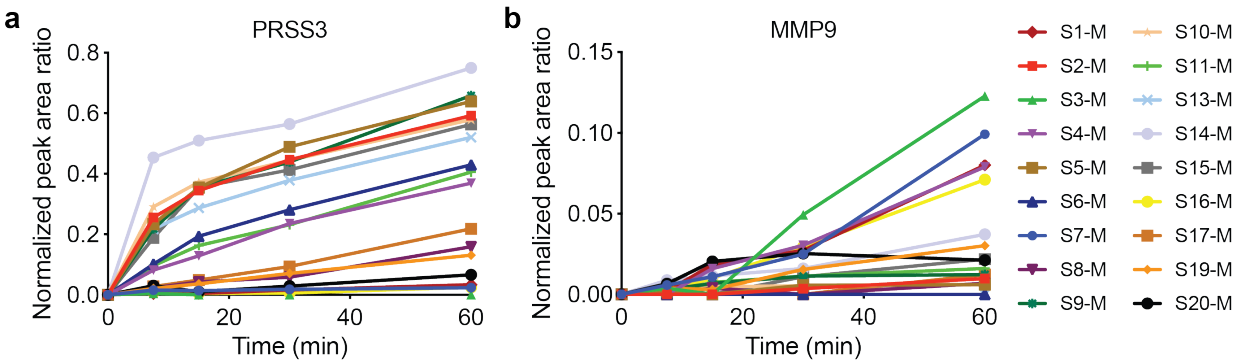

Figure 4.S4. Profiling cleavage kinetics using mass-barcoded bead library. Kinetics of substrate cleavage obtained from mass-barcoded library screen for the serine protease PRSS3 (a) and the metalloproteinase MMP9 (b). Kinetics were assessed via quantification of liberated barcodes isolated via magnetic separation at various time points after addition of protease, followed by mass spectrometry quantification with LC-MS/MS. Lines represent means of two independent measurements.

resolution (Table 4.S1). *In situ* labeling of protease activity offers several advantages, including the opportunity to elucidate the spatial distribution of protease activity within a tissue (e.g., at the invasive front of a tumor) and to colocalize protease activity with cell type-specific markers (Table 4.S1). Drawing from previous work using cell-penetrating peptides *(27, 29, 30)*, we hypothesized that peptides that consist of a cationic poly-arginine (polyR) domain complexed to an anionic poly-glutamic acid (polyE) domain via a protease-cleavable linker could enable *in situ* labeling of protease activity on tissue sections (Fig. 4.1b). Specifically, we reasoned that degradation of the protease-cleavable linker component of these activatable zymography probes (AZPs) would liberate the fluorophore-labeled polyR, which could then electrostatically interact with negatively-charged molecules in the tissue, enabling localization by microscopy.

We first validated this technique on a tissue type with a known spatial distribution of protease expression. Since colon epithelial cells secrete serine proteases *(115)* including urokinase plasminogen activator (uPA) *(116)*, we synthesized a Cy5-labeled serine protease-cleavable AZP, termed S6-Z, and applied it to fresh-frozen sections of normal mouse colon (Fig. 4.3a). Fluorescence signal from S6-Z was detected in the epithelial regions of the colon, and a free polyR was used as a binding control (Fig. 4.3b). No signal was observed on colon tissue incubated with the non-cleavable, *d*-stereoisomer version of the probe, termed dS6-Z, which indicated that proteolytic processing was required to activate the probe. Furthermore, this spatially-resolved S6-Z labeling was abrogated by addition of the serine protease inhibitor 4-(2-aminoethyl)benzenesulfonyl fluoride hydrochloride (AEBSF; Fig. 4.3b).

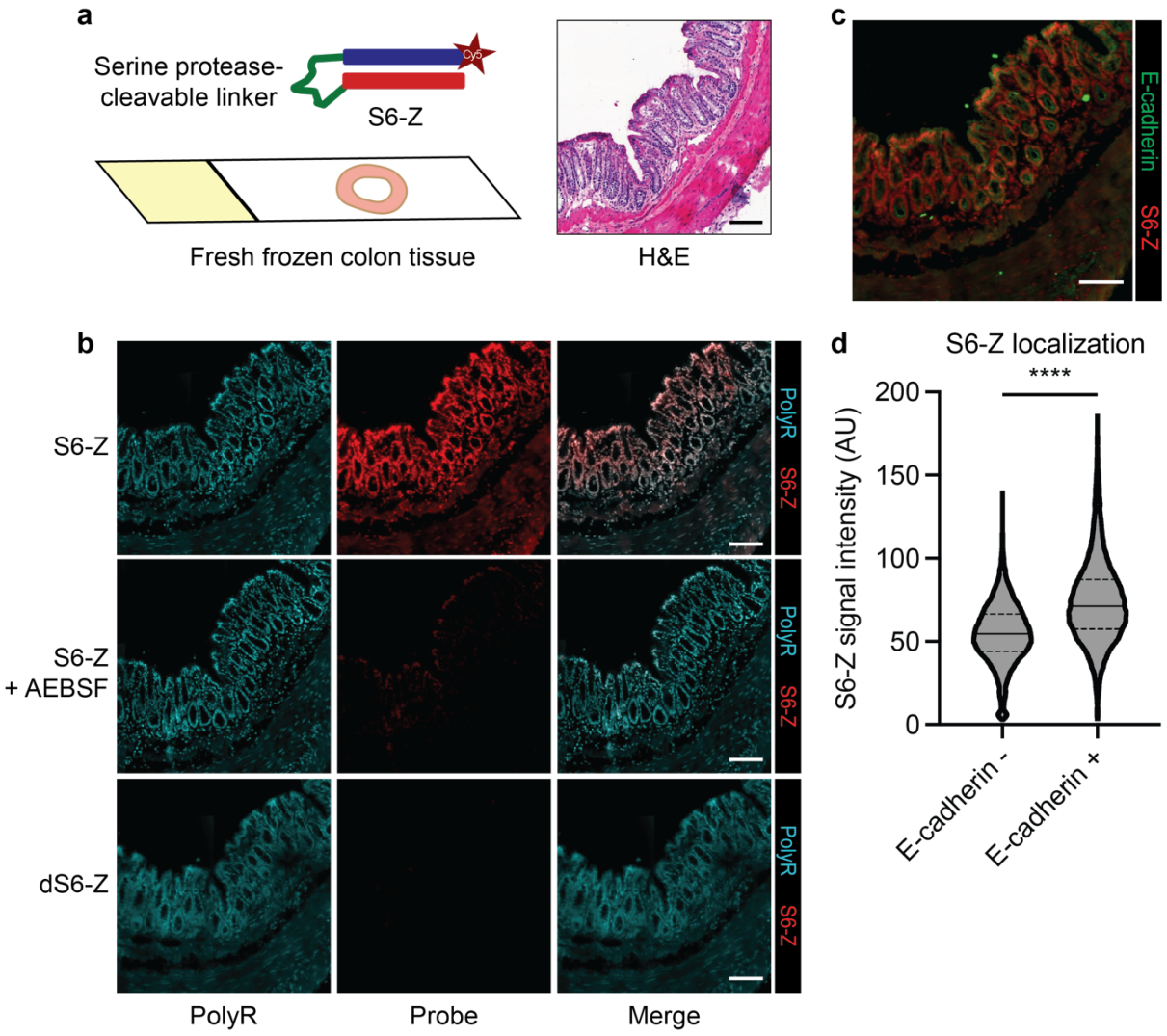

Figure 4.3. *In situ* localization of protease activity with AZPs. (a) The serine protease-responsive AZP, S6-Z, was applied to fresh frozen sections of healthy mouse colon (left). Hematoxylin and eosin (H&E) stain of a representative colon tissue region (right). (b) Staining of frozen colon sections with PolyR-Cy7 (left column, teal) and either uPA-activatable S6-Z-Cy5 (top and middle rows; S6-Z, red) or d-stereoisomer dS6-Z-Cy5 (bottom row; dS6-Z, red). Top and middle rows show staining of consecutive sections without (top) and with (bottom) the serine protease inhibitor AEBSF. (c) Region of colon tissue showing staining from activated S6-Z (red) with staining for the epithelial cell marker E-cadherin (green). (d) Quantification of nuclear S6-Z signal intensity from E-cadherin negative (n = 15864) and E-cadherin positive (n = 12207) cells (quantification over one representative colon section; center line represents median, dashed lines represent quartiles; two-tailed unpaired t-test, ****$P < 1 \times 10^{-15}$). All scale bars = 100 μm.

To validate the extent and specificity of this activity-dependent probe localization, we applied the activatable S6-Z to colon sections and co-stained for the epithelial cell marker E-cadherin. As the primary source of serine proteases in this tissue has been shown to be colon epithelial cells *(115, 116)*, our observation that E-cadherin+ cells exhibited brighter labeling by S6-Z than E-cadherin- cells ($P < 1 \times 10^{-15}$) was consistent with our hypothesis that AZPs enable proximal localization of cell type-specific protease activity *in situ* (Fig. 4.3c-d). Together, these results indicate that AZPs can directly measure peptide cleavage events *in situ* to spatially localize protease activity with low background binding.

Discovery of human PCa-responsive protease substrates

We next sought to validate the use of AZPs as a tool to identify disease-responsive peptides in human tissue. To this end, we designed a library of 19 AZPs based on a panel of peptides previously found by our group to be recognized by proteases dysregulated in PCa *(41)*. With the exception of the protease-cleavable linker and fluorophore, these AZPs were identical in design to the serine protease-responsive S6-Z. We first sought to verify that proteolysis was required for tissue binding across the entire AZP library. We found that AZP pre-cleavage by a cognate recombinant protease with specificity for the AZP linker (Fig. 4.2; MMP13 for MMP-responsive substrates; PRSS3, KLK14, or KLK2 for serine protease-responsive substrates) resulted in increased tissue binding for all 19 probes (Fig. 4.S5). The proteolysis-dependent tissue labeling observed across the probe library supports the modularity of the AZP platform.

Given that serine proteases are among those known to be dysregulated in human PCa *(41)*, we selected two serine protease-responsive AZPs (S10-Z and S2-Z) to evaluate against a fresh-frozen human tissue microarray (TMA) containing biopsies from normal prostates and PCa tumors across

a range of Gleason scores (Fig. 4.S6). Tissue binding of S10-Z (Fig. 4.4a-b) and S2-Z (Fig. 4.S7a-b) was abrogated by a broad-spectrum cocktail of protease inhibitors. We then investigated whether either of the tested AZPs preferentially labeled PCa tissue relative to normal prostate. Both serine protease-responsive AZPs, S10-Z (P = 0.0063, Fig. 4.4c) and S2-Z (P = 0.0284, Fig. 4.S7c), exhibited significantly increased labeling of PCa relative to normal prostate tissue, enabling strong classification of diseased tissue (S10-Z AUC = 0.948, Fig. 4.4d; S2-Z AUC = 0.917, Fig. 4.S7d). These findings demonstrate that serine protease activity is dysregulated in human PCa and suggest that AZPs may be used to discover peptide substrates responsive to human disease.

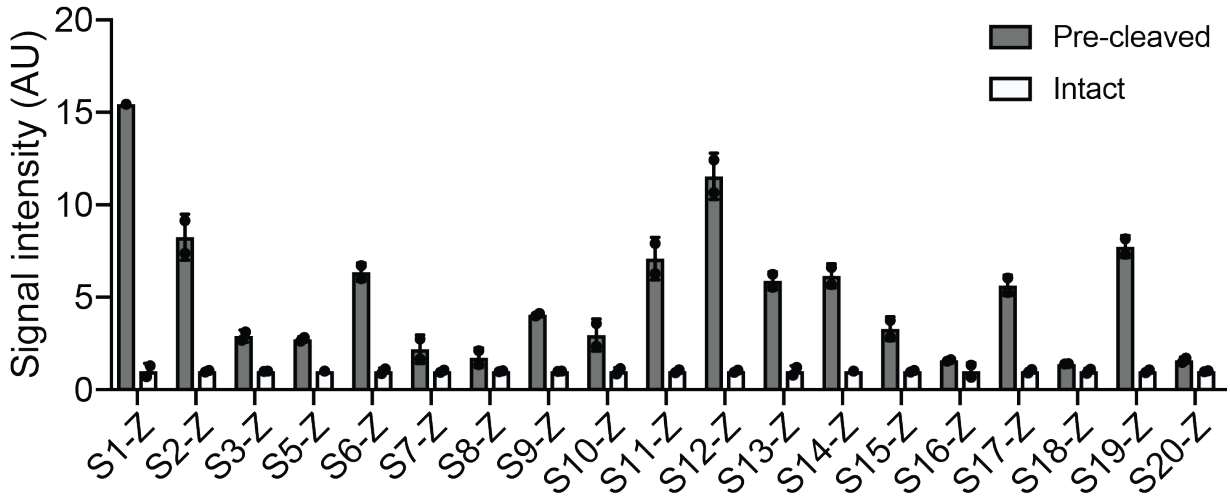

Figure 4.S5. AZP library characterization. AZPs, either intact or with linkers pre-cleaved by a cognate recombinant protease, were applied to fresh frozen colon tissue for 30 minutes, and fluorescent signal intensity of bound probes was quantified (n = 1-2 replicates per probe; mean ± s.d.).

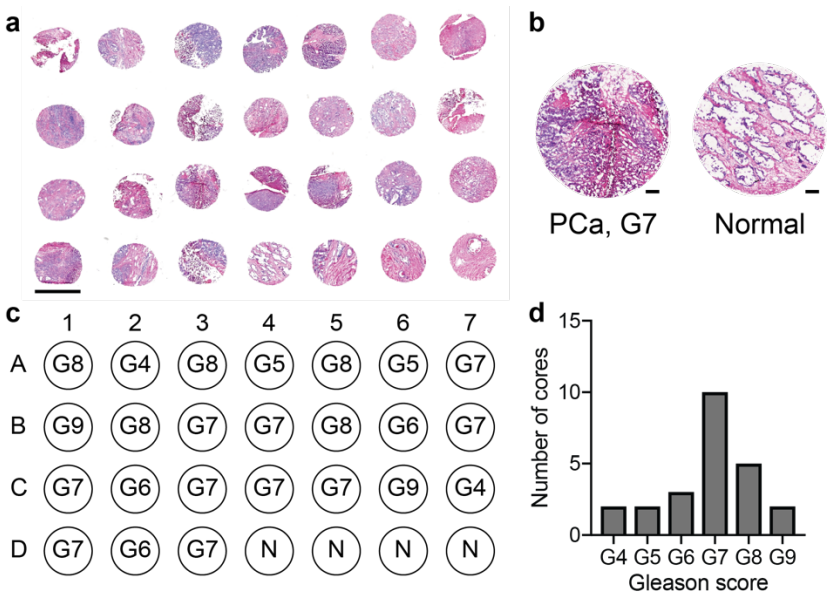

Figure 4.S6. Fresh frozen human prostate cancer tissue microarray (TMA). (a) H&E stain of human prostate cancer (PCa) TMA. Scale bar = 2 mm. (b) Hematoxylin and eosin stain of select biopsy cores from Gleason 7 PCa tumor (left) and normal prostate (right). Scale bars = 200 µm. (c) TMA map detailing the Gleason scores (i.e., G4-G10) for prostate cancer specimens. N = normal. (b) Distribution across Gleason scores for cores in the TMA.

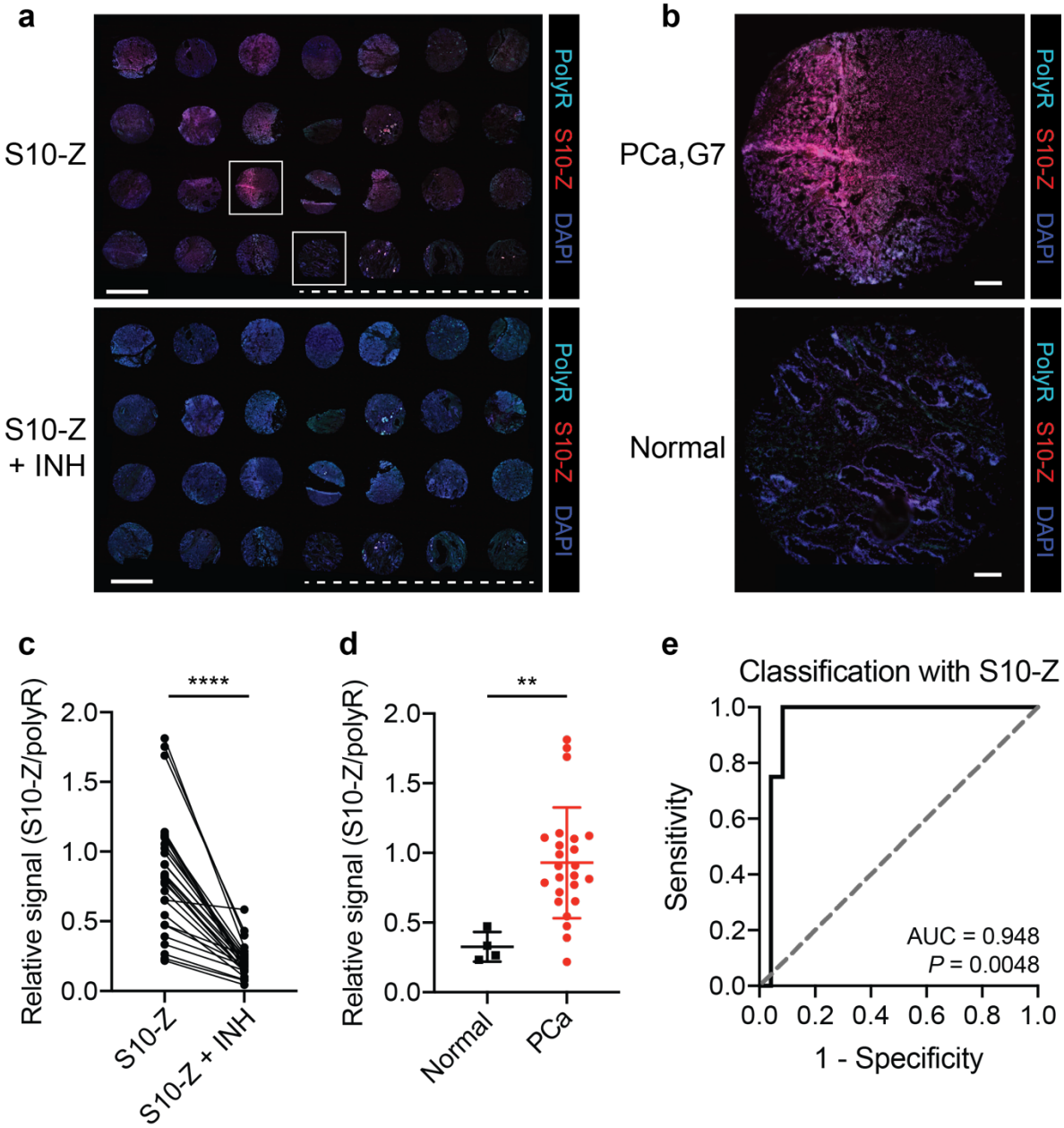

Figure 4.4. Discovery of a human PCa-responsive protease substrate. (a) Application of S10-Z AZP to a human PCa tissue microarray (TMA) consisting of 24 prostate adenocarcinoma samples and 4 normal prostate samples (S10-Z, top). A consecutive TMA was stained with S10-Z along with a cocktail of protease inhibitors (S10-Z + INH, bottom). Dotted lines are shown below normal prostate samples. Scale bars = 2 mm. (b) Higher-magnification images of boxed cores from (a) showing Gleason 7 PCa (top) and normal prostate (bottom). Scale bars = 200 µm. (c) Quantification of average S10-Z intensity relative to polyR (binding control) intensity across each TMA core (n = 28) for sections incubated with (S10-Z + INH) and without (S10-Z) protease inhibitors (two-tailed paired t-test, ****$P < 0.0001$). (d) Quantification of relative S10-Z intensity from normal (n = 4) and PCa tumor (n = 24) cores (mean ± s.d.; two-tailed unpaired t-test, **$P = 0.0063$). (e) Receiver-operating characteristic (ROC) curve showing performance of relative AZP signal (S10-Z/polyR) in discriminating normal from PCa tumor cores (AUC = 0.948, 95% confidence interval 0.8627-1.000; $P = 0.0048$ from random classifier shown in dashed line).

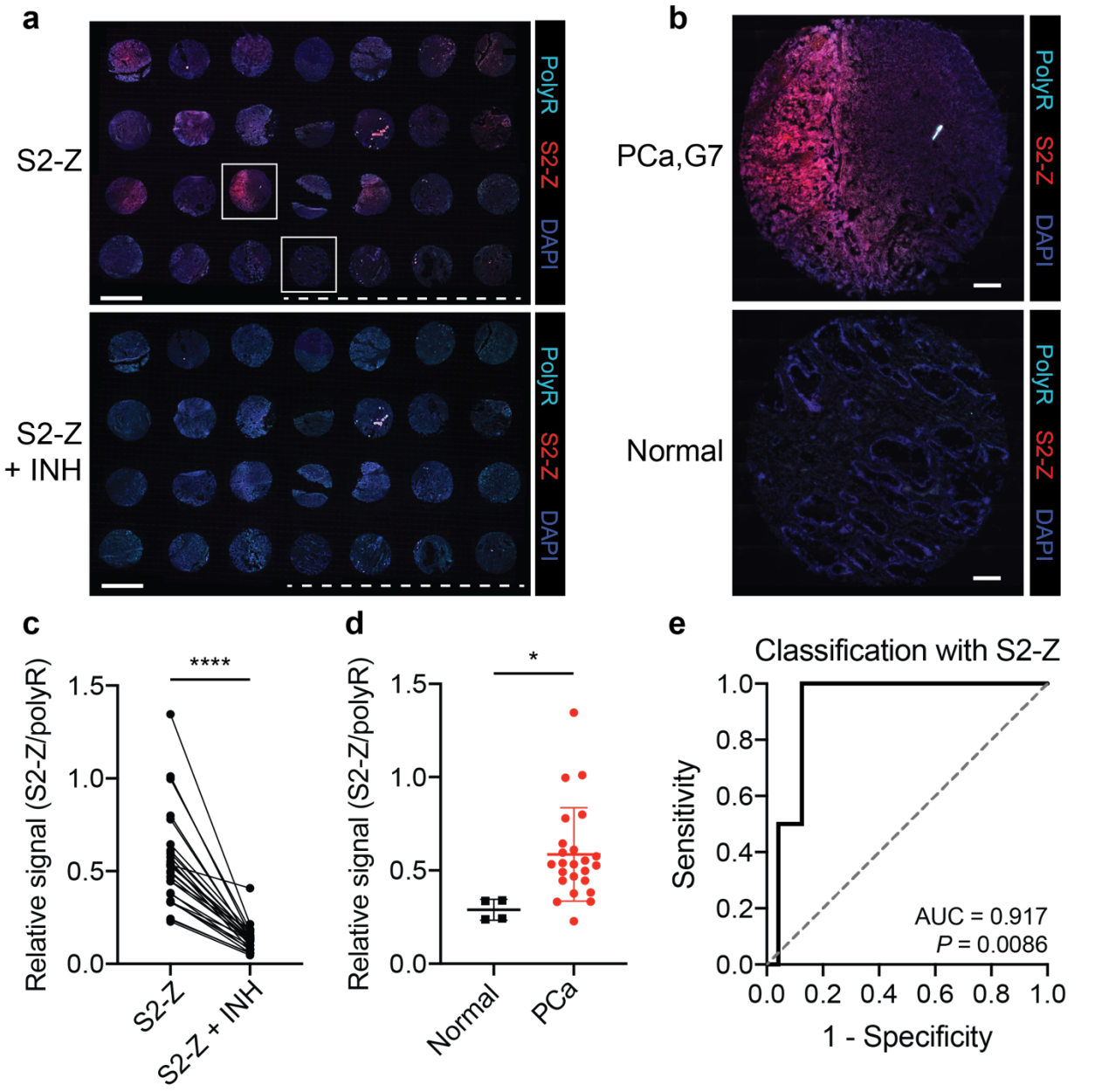

Figure 4.S7. S2-Z selectively labels human PCa tissue. (a) Application of S2-Z AZP to a human PCa tissue microarray (TMA) consisting of 24 prostate adenocarcinoma samples and 4 normal prostate samples (S2-Z, top). A consecutive TMA was stained with S2-Z along with a cocktail of protease inhibitors (S2-Z + INH, bottom). Dotted lines are shown below normal prostate samples. Scale bars = 2 mm. (b) Higher-magnification image of boxed cores from (a) showing Gleason 7 PCa (top) and normal prostate (bottom). Scale bars = 200 µm. Scale bars = 2 mm. (c) Quantification of average S2-Z intensity relative to polyR (binding control) intensity across each TMA core (n = 28) for sections incubated with (S2-Z + INH) and without (S2-Z) protease inhibitors (two-tailed paired t-test, ****$P < 0.0001$). (d) Quantification of relative S2-Z intensity from normal (n = 4) and PCa tumor (n = 24) cores (mean ± s.d.; two-tailed unpaired t-test, *$P = 0.0284$). (e) Receiver-operating characteristic (ROC) curve showing performance of relative AZP signal (S2-Z/polyR) in discriminating normal from PCa tumor cores (AUC = 0.917, 95% confidence interval 0.8103-1.000; $P = 0.0086$ from random classifier shown in dashed line).

Discovery and validation of a PCa-responsive peptide substrate in the Hi-Myc model

Having developed both a bulk, multiplexed cleavage assay and highly modular *in situ* activity probes, we next sought to leverage these tools to probe the biology of protease dysregulation in a clinically-relevant mouse model and, in so doing, rationally design a protease-activatable diagnostic or therapeutic from the bottom up. We therefore turned to the Hi-Myc GEMM, wherein *c-Myc* is overexpressed in the murine prostate, resulting in invasive PCa *(117)*. We screened homogenates of prostates from Hi-Myc mice and age-matched healthy controls against our multiplexed, mass-encoded bead library and found distinct cleavage patterns between diseased and healthy prostates (Fig. 4.S8a).

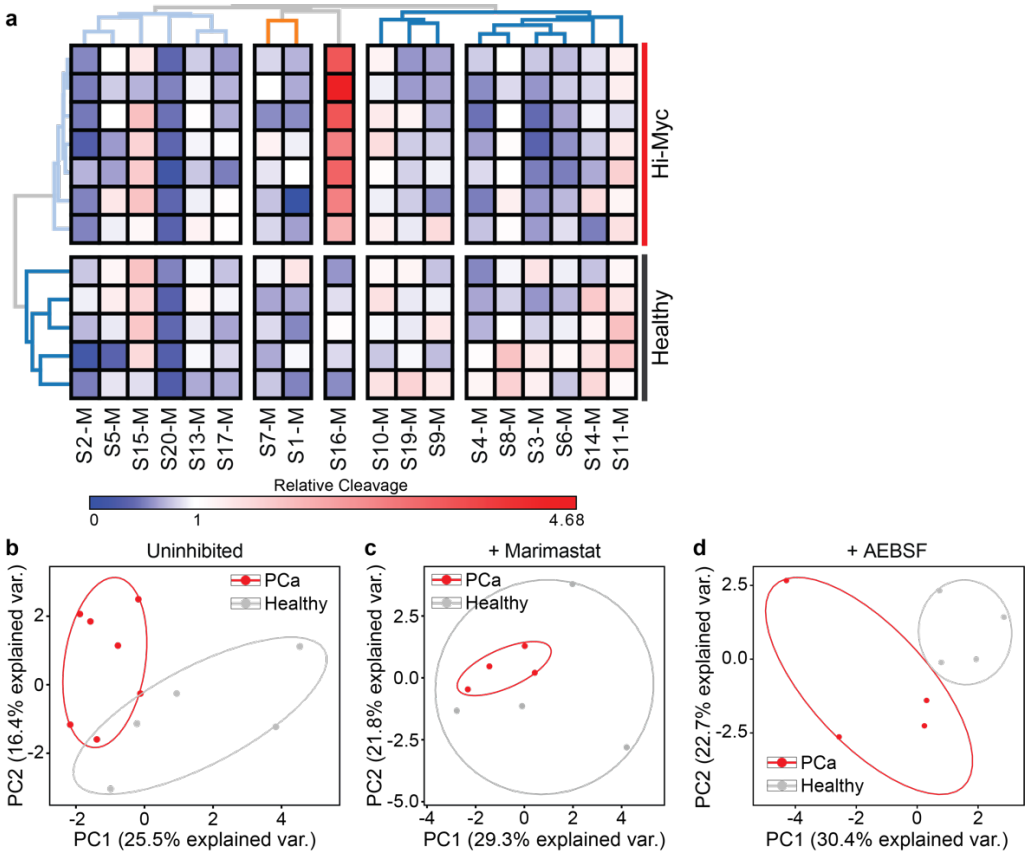

Figure 4.S8. Differential cleavage of peptide S16 is driven by MMP dysregulation and drives differentiation of Hi-Myc from healthy prostates. (a) Hierarchical clustering of cleavage data from multiplexed protease substrate screen of mass-encoded bead library against homogenates of prostates from healthy (gray, $n = 5$) and Hi-Myc (red, $n = 7$) mice. (b-d) PCA of cleavage data from homogenates incubated without inhibitor (b), with the metalloprotease inhibitor marimastat (c), or with the serine protease inhibitor AEBSF (d).

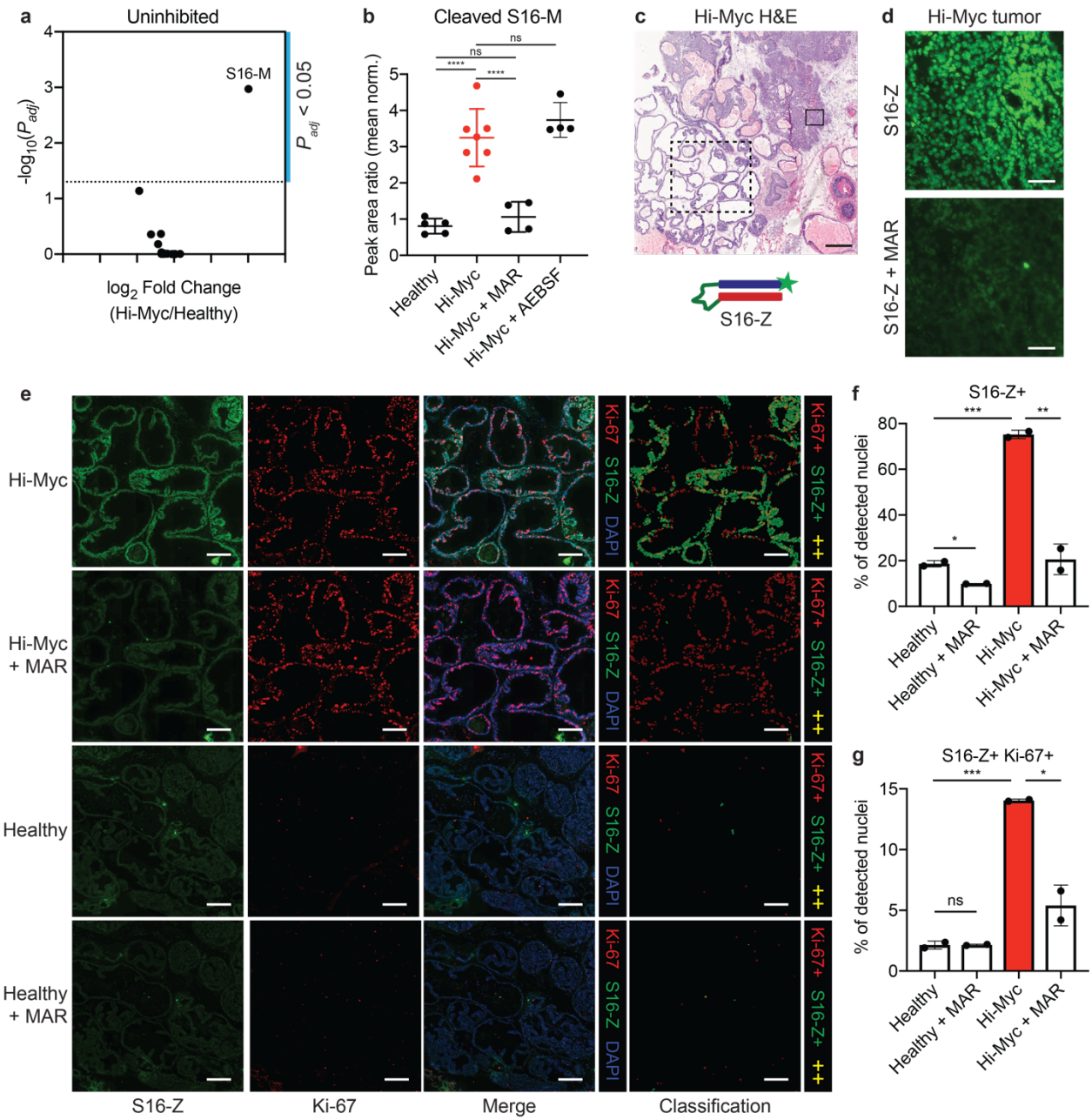

Figure 4.5. Identification and *in situ* localization of a PCa-responsive peptide substrate in the Hi-Myc model. (a) Volcano plot showing $\log_2$ fold change in mean normalized cleavage product concentrations between Hi-Myc (n = 7) and healthy (n = 5) prostate homogenates (x-axis) and $-\log_{10}(P_{adj})$ (y-axis). Significance was calculated by two-tailed t-test followed by adjustment for multiple hypotheses using the Holm-Sidak method. Dotted line is at $P_{adj} = 0.05$. (b) Quantification of S16-M cleavage for healthy prostate homogenates ($n = 5$) and Hi-Myc prostate homogenates, either uninhibited (Hi-Myc, $n = 7$), in the presence of the MMP inhibitor marimastat (Hi-Myc + MAR, $n = 4$), or in the presence of the serine protease inhibitor AEBSF (Hi-Myc + AEBSF, $n = 4$) (mean ± s.d.; one-way ANOVA with Tukey's correction for multiple comparisons, ****$P < 0.0001$, *ns* = not significant). (c) H&E staining of Hi-Myc prostate tissue, representative example shown. Solid and dashed boxes indicate tissue regions in (d) and (e), respectively. Scale bar = 500 µm. (d) Staining of boxed Hi-Myc tumor region from (c) with MMP-activatable S16-Z-FAM (S16-Z, top). A consecutive section was stained with S16-Z in the presence of marimastat (S16-Z + MAR, bottom). Scale bars = 50 µm. (e) Application of S16-Z (green), with or without MAR, to prostate

tissues from Hi-Myc and healthy mice with co-staining for the proliferation marker Ki-67 (red). Sections were counterstained with DAPI (blue). Detected cells were classified on the basis of S16-Z and Ki-67 staining intensities to produce cell classification maps (red: Ki-67+; green: S16-Z+; yellow: S16-Z+ and Ki-67+, ++). Images of Hi-Myc tissues show the glandular region boxed in (c). Scale bars = 200 μm. (f) Quantification of fraction of detected nuclei positive for S16-Z (n = 2 consecutive sections per group, >100,000 cells per replicate; mean ± s.d.; two-tailed unpaired t-test, *P = 0.0122, **P = 0.00794, ***P = 0.000803). (g) Quantification of fraction of detected nuclei positive for both S16-Z and Ki-67 in healthy, MMP-inhibited healthy (Healthy + MAR), Hi-Myc, and MMP-inhibited Hi-Myc (Hi-Myc + MAR) prostate tissue sections (n = 2 consecutive sections per group, >100,000 cells per replicate; mean ± s.d.; two-tailed unpaired t-test, ^{ns}P = 0.973, *P = 0.0185, ***P = 0.000429).

Intriguingly, this assay revealed that a single peptide sequence ("S16", or "S16-M" when coupled to mass barcode) was differentially cleaved by Hi-Myc prostate homogenates relative to samples from healthy control mice (Fig. 4.5a). Based on the results of the bead screen of peptide substrates against recombinant proteases (Fig. 4.2b), we predicted that the observed cleavage of the S16-M probe was likely mediated by MMP activity. Consistent with this hypothesis, we found that pre-treatment of the prostate homogenates with the MMP inhibitor marimastat (MAR) fully inhibited cleavage of S16-M by the Hi-Myc mouse-derived samples ($P < 0.0001$, Fig. 4.5b), whereas pre-treatment with the serine protease inhibitor AEBSF had no effect. Accordingly, unsupervised dimensionality reduction by PCA succeeded in separating the uninhibited homogenates (Fig. 4.S8b) and homogenates treated with AEBSF (Fig. 4.S8c), but this separation was abrogated by addition of marimastat (Fig. 4.S8d).

In order to localize cleavage of S16 *in situ*, we synthesized an AZP that incorporated this substrate (S16-Z), verified that tissue binding was dependent on linker degradation (Fig. 4.S9), and applied this probe to fresh-frozen sections of prostates from Hi-Myc mice (Fig. 4.5c). Fluorescence signal from S16-Z was observed in Hi-Myc tumors and was abrogated by the MMP inhibitor marimastat, suggesting that S16-Z measured *in situ* tumor-associated MMP activity in Hi-Myc prostates (Fig. 4.5d). In addition, we found that S16-Z labeled histologically normal glands

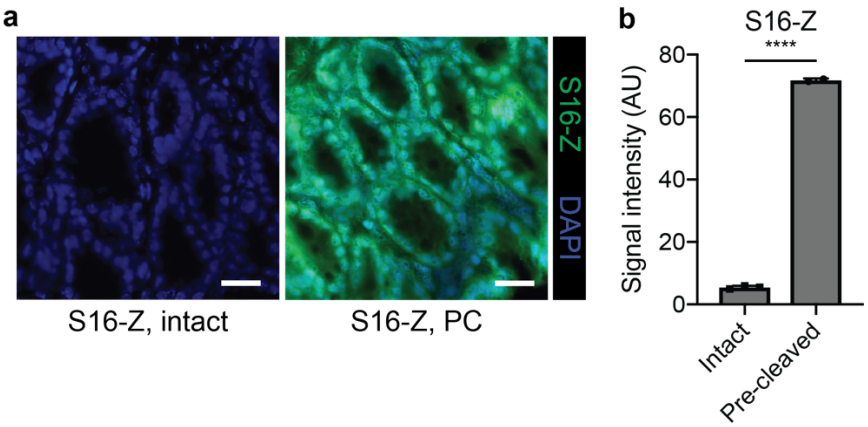

Figure 4.S9. S16-Z tissue binding depends on proteolytic cleavage. (a) Binding of intact or MMP12 pre-cleaved (PC) S16-Z to fresh frozen colon tissue following incubation at 4° C. Scale bars = 25 µm. (b) Quantification of S16-Z binding for intact probe or probe pre-cleaved by MMP12 (n = 2-3 replicates; mean ± s.d.; two-tailed unpaired t-test, ****$P < 0.0001$).

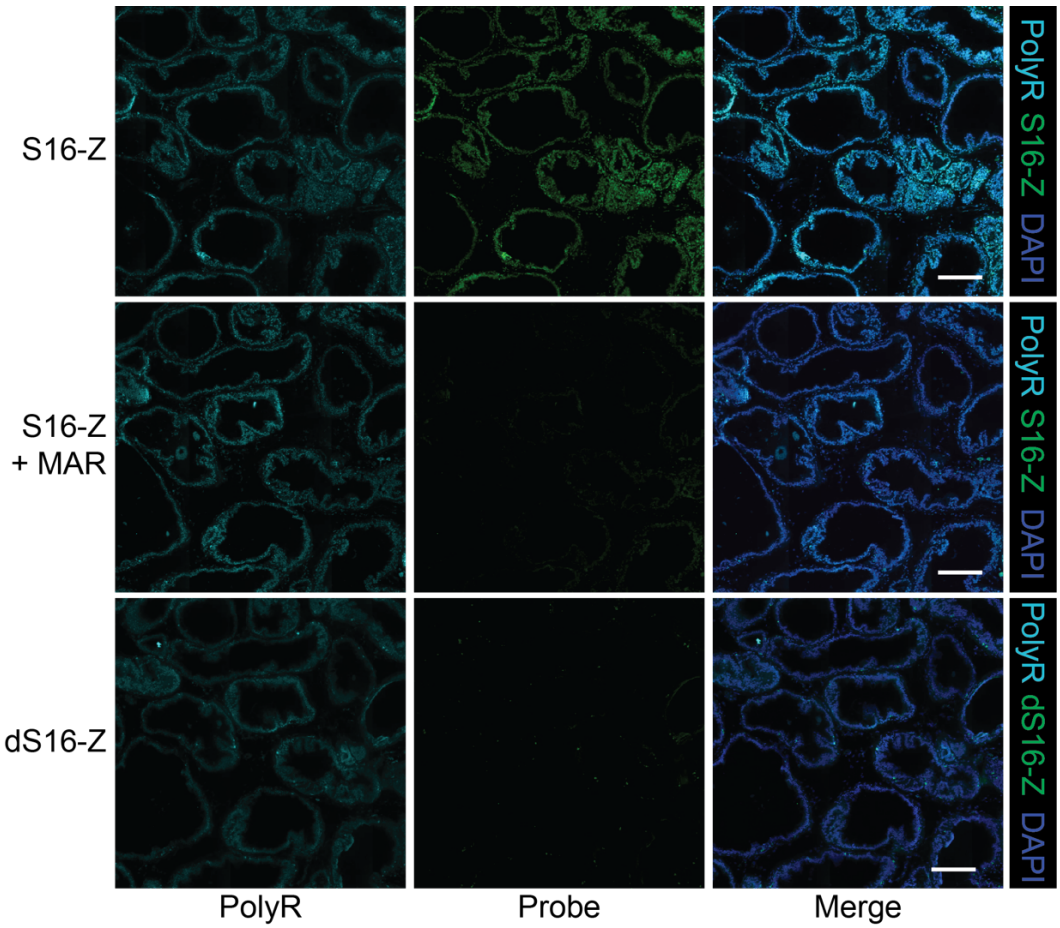

Figure 4.S10. S16-Z labeling of Hi-Myc tissue is dependent on *in situ* MMP activity. Staining of Hi-Myc tissue with PolyR-Cy7 (left column, teal) and either MMP-activatable S16-Z-FAM (top and middle rows; S16-Z, green) or *d*-stereoisomer dS16-Z-FAM (bottom row; dS16-Z, green). Top and middle rows show staining of consecutive sections without (top) and with (middle) the MMP inhibitor marimastat (MAR). Sections were counterstained with DAPI (blue). Scale bars = 200 µm.

of the Hi-Myc ventral lobe (Fig. 4.5c), and that this labeling was abrogated by marimastat (Fig. 4.S10). Furthermore, no tissue labeling was observed in sections treated with the non-cleavable probe dS16-Z, further validating that S16-Z tissue binding was proteolytically driven (Fig. 4.S10). Finally, a co-incubated positive control peptide (free polyR) exhibited consistent binding under all three (S16-Z, S16-Z+MAR, dS16-Z) conditions (Fig. 4.S10).

Though these glands appeared histologically normal, their positivity for the proposed tumor-specific activity probe, S16-Z, raised the possibility of local, underlying pro-tumorigenic activity in these regions. In an effort to undertake further biological characterization, we applied S16-Z to prostate tissue sections from Hi-Myc and age-matched healthy mice and co-stained for the proliferation marker Ki-67*(118)* (Fig. 4.S11). Strikingly, we observed robust Ki-67 staining in S16-Z-positive, but otherwise histologically normal, glands of the Hi-Myc prostate, but no Ki-67 staining and reduced S16-Z labeling in a histologically similar region of ventral prostate from healthy mice (Fig. 4.5e). Segmentation-based, cell-level classification indicated the presence of cells that stained positively for both S16-Z and Ki-67 within this glandular region of Hi-Myc tissue, but an absence of such double-positive cells in healthy prostatic glands (Fig. 4.5e). Similar analyses of a Hi-Myc tumor showed the presence of S16-Z-positive tumor cells that also stained positively for Ki-67 (Fig. 4.S12). Furthermore, S16-Z labeling across both glandular and tumor regions of Hi-Myc tissues was abrogated by marimastat, while MMP inhibition appeared to have a minimal effect on S16-Z staining in healthy tissues (Fig. 4.5e; Fig. 4.S12).

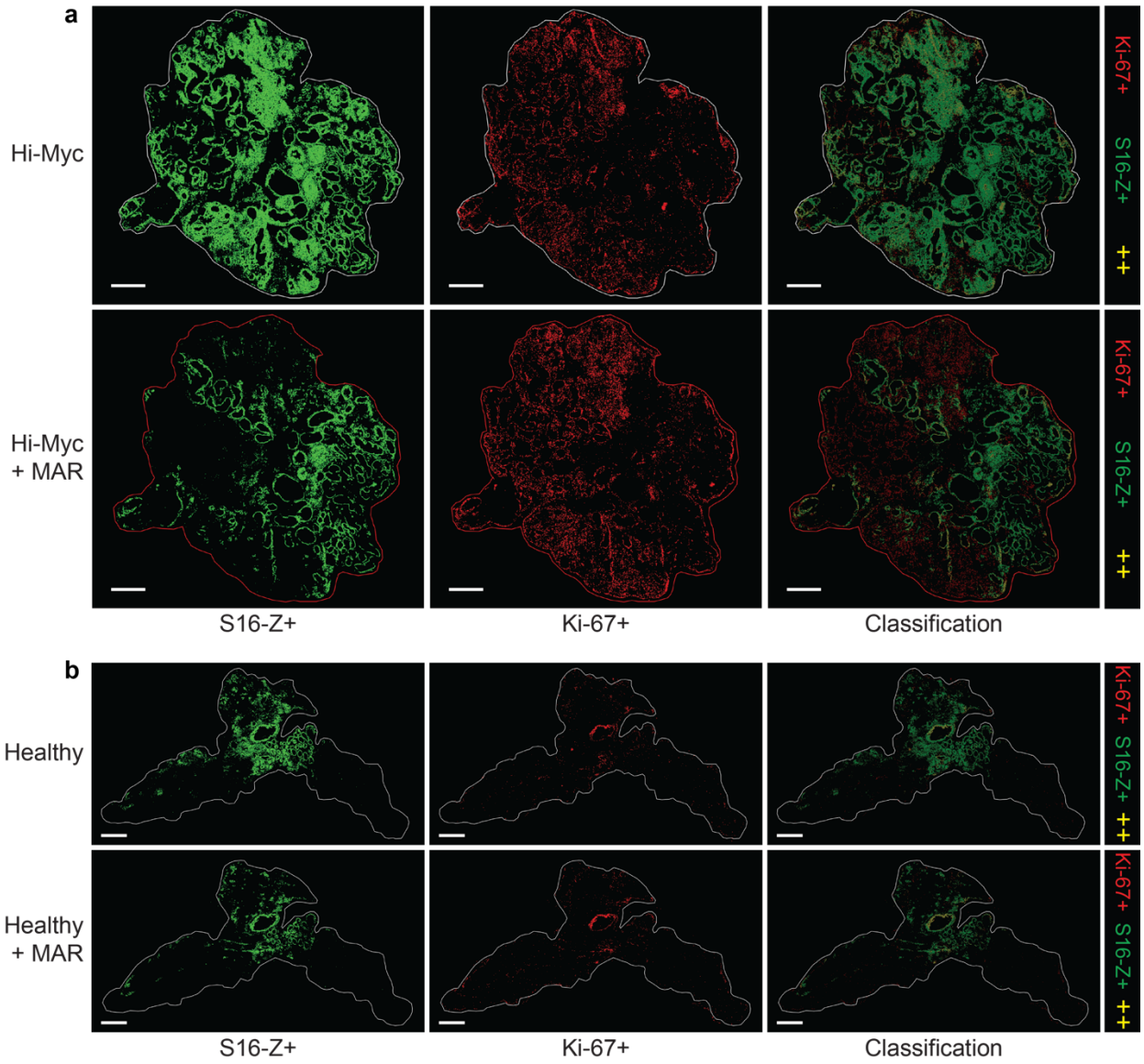

Figure 4.S11. S16-Z and Ki-67 staining of healthy and Hi-Myc prostate tissue sections. (a, b) S16-Z, with or without MAR, was applied to prostate tissues from Hi-Myc and healthy mice with co-staining for the proliferation marker Ki-67. Detected cells were classified on the basis of S16-Z and Ki-67 staining intensities to produce cellular classification maps (green: S16-Z+, red: Ki67+, yellow: S16-Z+ and Ki-67+). Scale bars = 1 mm.

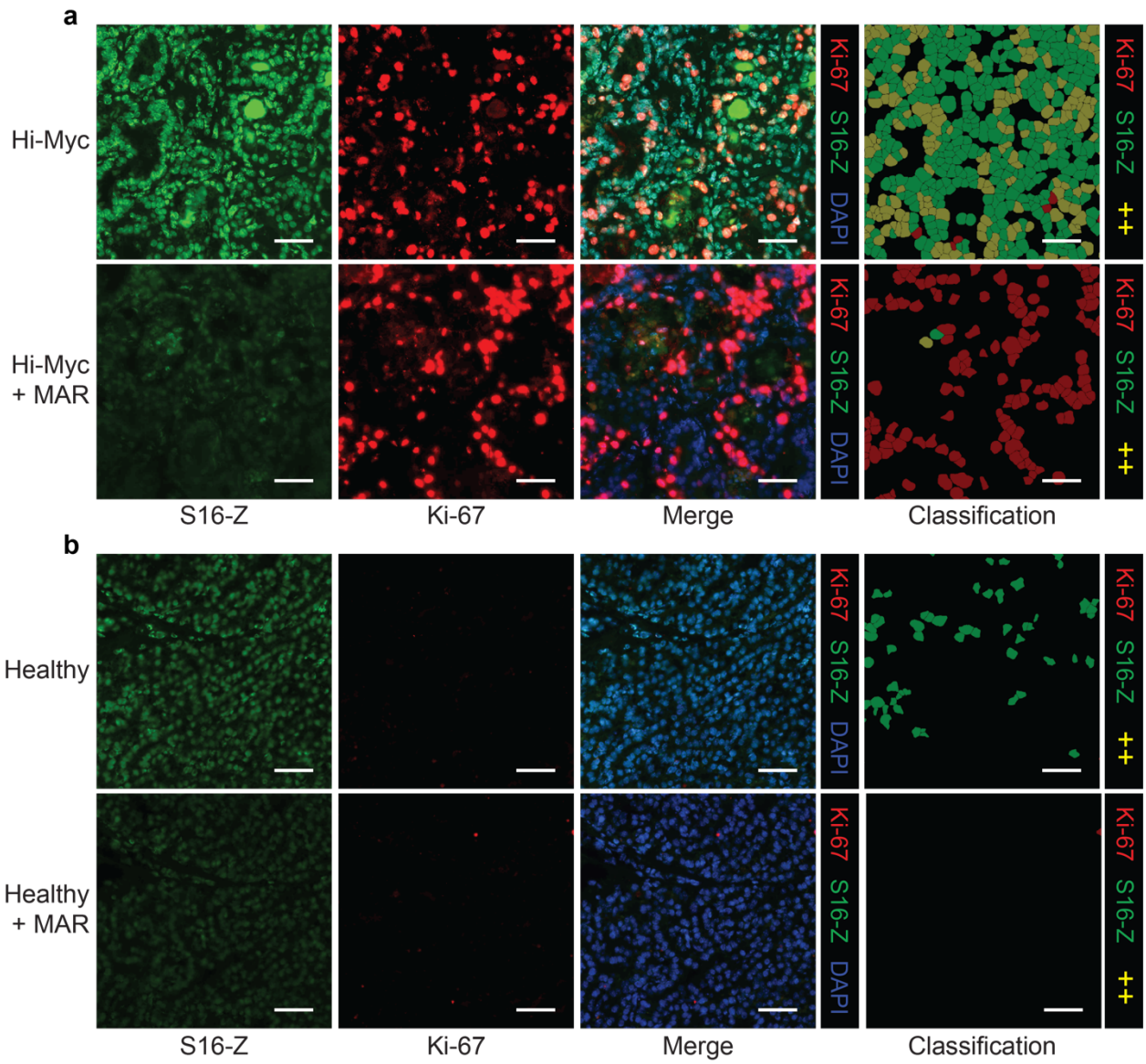

Figure 4.S12. MMP activity drives S16-Z labeling of proliferative tumor regions in Hi-Myc prostates. (a, b) Staining of Hi-Myc tumor region (a) and healthy prostate tissue (b) with S16-Z (green) with co-staining for the proliferation marker Ki-67 (red). Consecutive sections were stained with S16-Z and Ki-67 in the presence of marimastat (MAR). Sections were counterstained with DAPI (blue). Detected cells were classified on the basis of S16-Z and Ki-67 staining intensities to produce cellular classification maps (green: S16-Z+, red: Ki67+, yellow: S16-Z+ and Ki-67+). Scale bars = 50 μm.

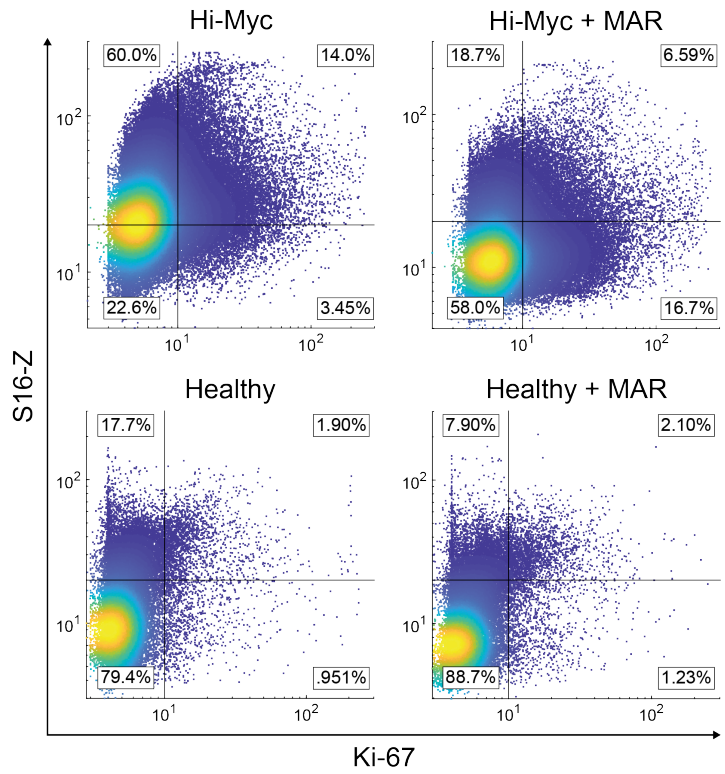

Figure 4.S13. Whole sample, cell-by-cell quantification of S16-Z and Ki-67 fluorescent staining. Cell-by-cell quantification of S16-Z and Ki-67 fluorescence intensity in detected nuclei from representative Hi-Myc and healthy prostate tissue sections incubated with or without the MMP inhibitor marimastat (MAR). Lines represent thresholds for positivity for each of the markers.

To quantify these differences, we performed cell-by-cell quantification of S16-Z and Ki-67 staining intensities across entire Hi-Myc and healthy prostate tissue sections (Fig. 4.S13). This analysis indicated that Hi-Myc tissue exhibited a significantly increased proportion of S16-Z-positive cells relative to healthy prostates ($P = 0.000803$, Fig. 4.5f). Furthermore, incubation with marimastat significantly reduced the number of S16-Z-positive cells in Hi-Myc prostates ($P = 0.00794$, 72.7% decrease; Fig. 4.5f), and, to a lesser extent, in healthy prostates ($P = 0.0122$, 46.9% decrease; Fig. 4.5f). In line with our qualitative observations, Hi-Myc tissues contained a significantly greater fraction of Ki-67-positive cells relative to healthy prostate tissue ($P = 0.000859$, Fig. 4.S14). Finally, as suggested by cell-based segmentation analysis, we observed a significantly greater fraction of S16-Z, Ki-67 double-positive cells in Hi-Myc prostate sections relative to healthy tissues ($P = 0.000429$, Fig. 4.5g), while the majority of detected cells in

healthy prostates were negative for both markers (Fig. 4.S14). Taken together, these *in situ* measurements and quantitative analyses revealed significant dysregulation of MMP activity and cell proliferation in both tumor-containing and histologically normal regions of Hi-Myc tissue that was absent in healthy prostates.

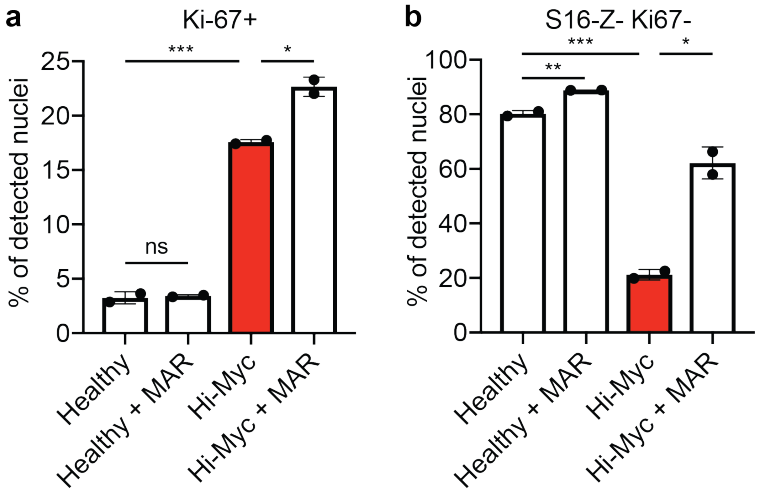

Figure 4.S14. Quantification of proliferation in healthy and Hi-Myc prostate tissue sections. (a) Quantification of fraction of detected nuclei positive for Ki-67 in healthy, MMP-inhibited healthy (Healthy + MAR), Hi-Myc, and MMP-inhibited Hi-Myc (Hi-Myc + MAR) prostate tissue sections ($n = 2$ consecutive sections per group, >100,000 cells per replicate; mean ± s.d.; two-tailed unpaired *t*-test, $^{ns}P = 0.707$, $^{*}P = 0.0158$, $^{***}P = 0.000859$). (d) Quantification of fraction of detected nuclei negative for both S16-Z and Ki-67 in healthy, MMP-inhibited healthy (Healthy + MAR), Hi-Myc, and MMP-inhibited Hi-Myc (Hi-Myc + MAR) prostate tissue sections ($n = 2$ consecutive sections per group, >100,000 cells per replicate; mean ± s.d.; two-tailed unpaired *t*-test, $^{*}P = 0.0113$, $^{**}P = 0.00900$, $^{***}P = 0.0004723$).

Motivated by these results, we next sought to identify the specific metalloprotease that was responsible for S16-M and S16-Z cleavage in the Hi-Myc model. We first screened a quenched fluorescent version of this substrate, S16-Q, against a panel of recombinant MMPs and found that this probe was broadly MMP-cleavable (Fig. 4.S15a-b). Next, we queried previously reported gene expression data from the Hi-Myc model *(117)* and found that the elastase MMP12, which efficiently cleaved S16-Q *in vitro*, was significantly upregulated at the gene expression level in Hi-Myc PCa relative to healthy prostate tissue (Fig. 4.S15c). We then validated this transcript at the protein level and found a significant increase in MMP12 in Hi-Myc prostates relative to age-matched healthy controls ($P = 0.0034$, Fig. 4.S15d). Additionally, Hi-

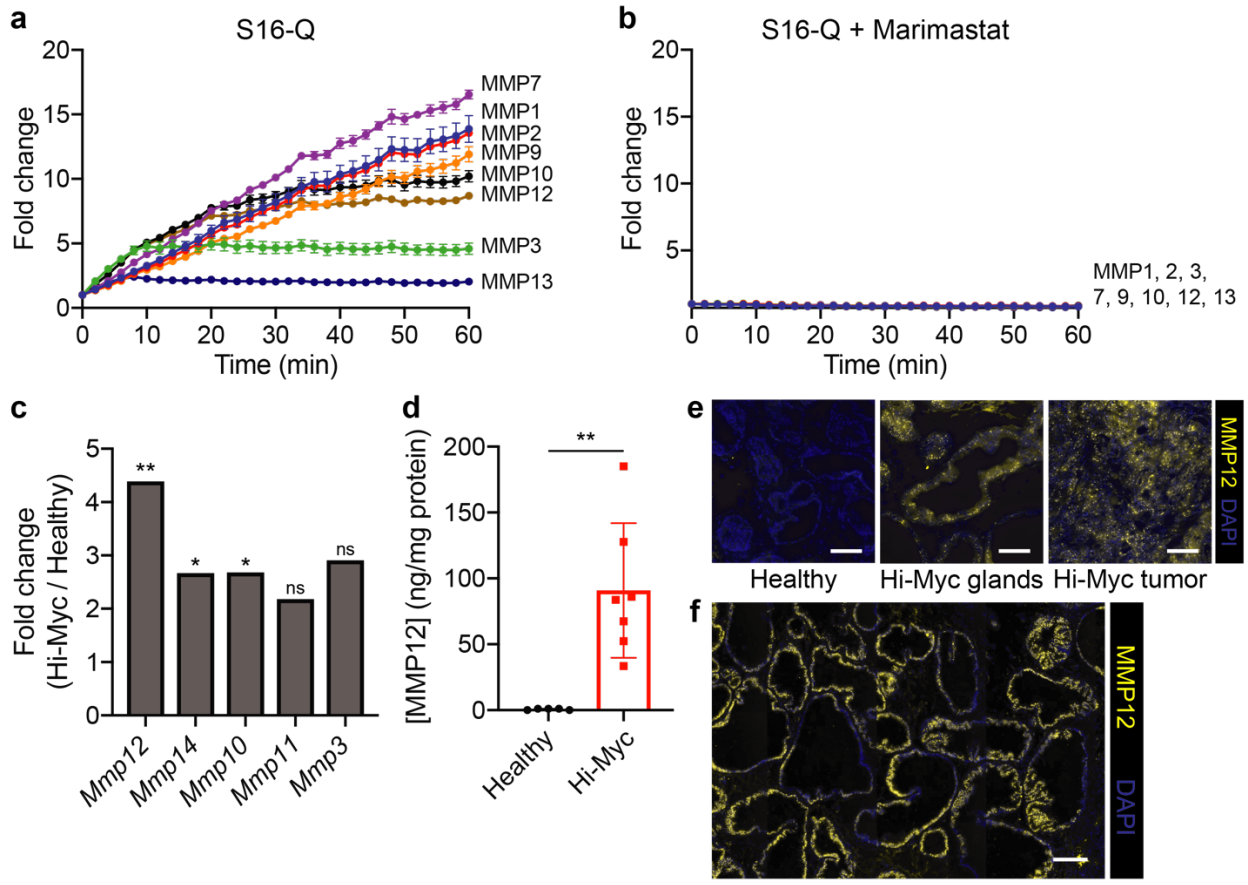

Figure 4.S15. Discovery of MMP12 dysregulation in Hi-Myc model. (a) Fluorescent dequenching measurements for panel of MMPs against fluorescent version (S16-Q) of Hi-Myc-responsive substrate S16. (b) Addition of MMP inhibitor marimastat (MAR) abrogated fluorescence increase for panel of MMPs against S16-Q. (c) Relative expression of the top 5 MMPs most significantly upregulated in Hi-Myc prostates relative to age-matched healthy controls, analyzed by Affymetrix microarray, adapted from Ellwood-Yen et al., *Cancer Cell* 2003 (two-tailed unpaired *t*-test; $^{**}P < 0.01$, $^{*}P < 0.05$, ns = not significant). (d) ELISA results comparing protein-level abundance of MMP12 in homogenates of Hi-Myc prostates relative to age-matched healthy controls ($n = 7$ Hi-Myc, $n = 5$ healthy; mean ± s.d.; Welch's *t*-test; $^{**}P = 0.0034$). (e) Immunofluorescence staining for MMP12 in fresh-frozen sections of healthy and Hi-Myc prostates, showing histologically similar regions of healthy and Hi-Myc prostates (Healthy, Hi-Myc glands) as well as a Hi-Myc tumor region (Hi-Myc tumor). Scale bars = 100 μm. (f) Immunofluorescence staining for MMP12 in histologically normal-appearing region of Hi-Myc tissue in Figure 4.5. Scale bar = 200 μm.

Myc prostates stained positively for MMP12 while healthy prostates did not (Fig. 4.S15e). Finally, *in situ* staining revealed that MMP12 localized to the histologically normal-appearing, S16-Z, Ki-67-positive region of Hi-Myc tissue (Fig. 4.5e; Fig. 4.S15f). Overall, these results suggest that

MMP12 may be responsible for S16 cleavage in Hi-Myc prostates, highlighting the power of AZPs to enable biological characterization of protease dysregulation in disease.

In vivo validation of a protease-activated probe in the Hi-Myc model

Having identified that S16 was preferentially cleaved *in situ* in proliferative glands of Hi-Myc prostates, we sought to validate the utility of this peptide sequence to drive tumor accumulation of molecular probes *in vivo*. We synthesized a quenched imaging probe, S16-QZ, that was similar in design to activatable cell-penetrating peptides *(27, 30)* and incorporated S16 as a protease-cleavable linker. In this design, degradation of the protease-cleavable linker liberates the fluorophore-tagged polyR, resulting in a positively-charged, tissue-binding particle with Cy5 fluorescence. Accordingly, *in vitro* incubation of S16-QZ with MMP12 resulted in fluorescence activation, whereas the uncleavable dS16-QZ remained quenched even after incubation with the protease (Fig. 4.6a). To verify that tissue binding was dependent on linker degradation, we pre-cleaved S16-QZ with recombinant MMP12, incubated the probe with tissue sections at 4º C to allow tissue binding in the absence of protease activity, and observed significantly enhanced tissue fluorescence relative to intact S16-QZ (Fig. 4.6b, c).

Having verified that proteolytic processing was required for both fluorescence activation and tissue binding of this PCa-targeted probe, we next sought to assess disease-dependent probe activation and accumulation *in vivo*. S16-QZ and the uncleavable control peptide, dS16-QZ, were PEGylated to improve solubility and increase circulation time *(27)* and were subsequently administered intravenously into Hi-Myc mice and age-matched healthy controls (Fig. 4.6d). Significantly increased Cy5 fluorescence was observed in explanted prostates of Hi-Myc mice injected with S16-QZ relative to the uncleavable dS16-QZ ($P < 0.0001$, Fig. 4.6e), whereas no such difference

between the probes was observed in healthy prostates ($P = 0.0990$, Fig. 4.6e). Furthermore, Cy5 fluorescence after S16-QZ injection was found to be significantly increased in Hi-Myc prostates relative to healthy prostates ($P < 0.0001$, Fig. 4.6e), enabling perfect discrimination of diseased and healthy mice ($AUC = 1.000$, Fig. 4.6f). These results suggest that peptide substrates nominated via *ex vivo* activity profiling can be directly incorporated into protease-activated agents for *in vivo* use.

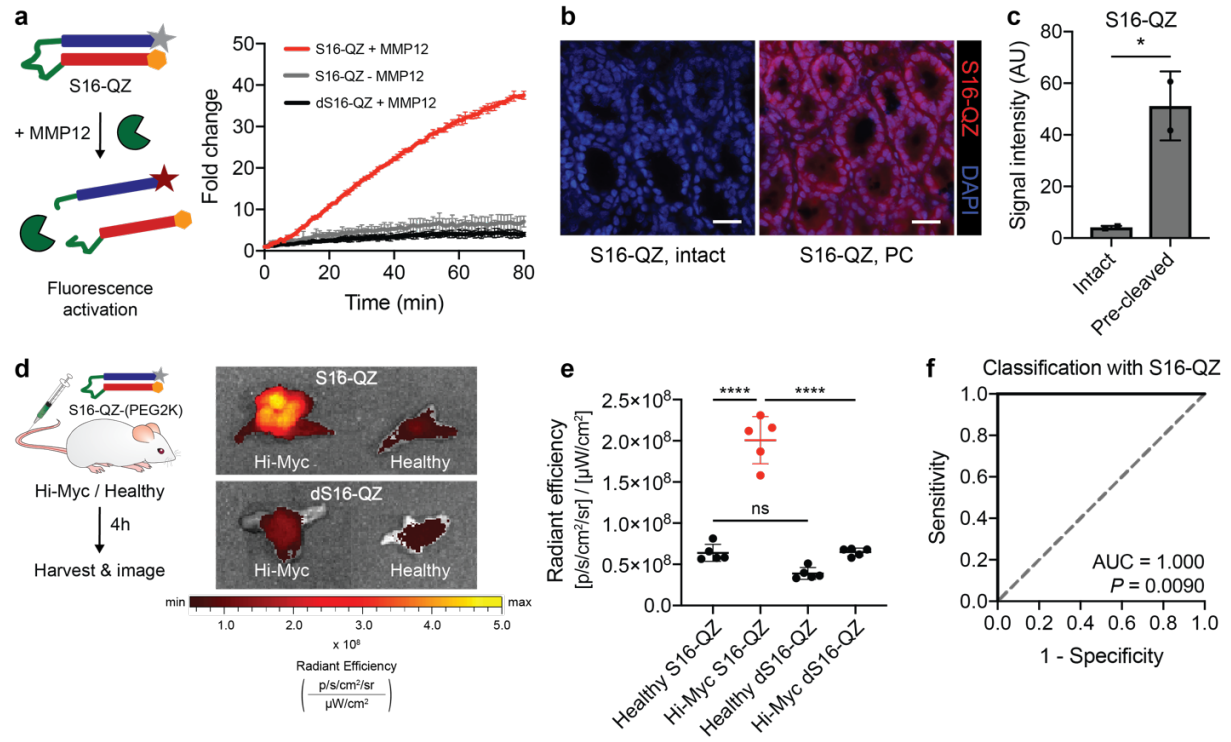

Figure 4.6. *In vivo* validation of an activatable imaging probe. (a) The quenched probe S16-QZ, consisting of a fluorophore-tagged polyR (grey star + blue rectangle) and quencher-tagged polyE (orange hexagon + red rectangle) linked via an MMP-cleavable linker (green), was incubated with recombinant MMP12, and fluorescence activation was monitored over time (left). Dequenching measurements for S16-QZ and d-stereoisomer dS16-QZ following incubation with recombinant MMP12 (right). (b) Binding of intact or MMP12 pre-cleaved (PC) S16-QZ to fresh frozen sections of healthy mouse colon tissue following incubation at 4° C. Scale bars = 25 µm. (c) Quantification of S16-QZ binding for intact probe or probe pre-cleaved by MMP12 ($n = 2$ replicates; mean ± s.d.; two-tailed unpaired *t*-test, $^{*}P = 0.0382$). (d) S16-QZ-(PEG2K) or uncleavable dS16-QZ-(PEG2K) was administered intravenously into age-matched Hi-Myc and healthy mice. 4 hours after injection, prostates were excised and imaged by IVIS ($n = 5$ per group). Representative prostates shown at right. (e) Quantification of epifluorescence radiant efficiency from experiment in (d) via IVIS imaging ($n = 5$ per group; mean ± s.d.; one-way ANOVA with Tukey's correction for multiple comparisons, $^{****}P < 0.0001$, $^{ns}P = 0.0990$). (f) Receiver-operating characteristic (ROC) curve showing performance of S16-QZ-(PEG2K) signal in discriminating healthy from Hi-Myc prostate explants (AUC = 1.000, 95% confidence interval 1.000-1.000; $P = 0.0090$ from random classifier shown in dashed line).

4.3 Discussion

In this work, we present an integrated set of *ex vivo* assays to discover and validate synthetic peptide substrates for use in activatable diagnostics and therapeutics. We first developed a multiplexed peptide cleavage assay that faithfully captured known substrate preferences of recombinant proteases. We then designed a modular *in situ* probe that enabled identification of two peptides that are preferentially cleaved by human PCa-associated proteases. Next, we demonstrated a bottom-up approach to the development of activatable diagnostics in the Hi-Myc model of PCa. We identified a peptide, S16, cleaved specifically by PCa-associated metalloproteinases, and found that its cleavage localized to proliferative, MMP12-positive glands in histologically normal regions of diseased prostates. Finally, we demonstrated that disease-responsive substrates identified via these *ex vivo* assays could be integrated into agents for *in vivo* protease-activated use.

Unlike isolated tools for multiplexed substrate profiling in bulk homogenates or for *in situ* zymography, our pipeline synergizes these two strategies to inform the rational design of protease-activated diagnostics and therapeutics. Each of these methods provides key advantages—multiplexed screening enables high-throughput discovery of candidate substrates, but *in situ* labeling is necessary to explore underlying biology and to validate the relevance of candidate substrates for specific applications. For example, an activatable therapeutic like a probody would ideally incorporate a peptide substrate that is cleaved broadly throughout the tumor, whereas an activatable imaging probe designed to monitor responses to immunotherapy might leverage a peptide that is strictly cleaved by proteases produced by tumor-infiltrating lymphocytes. Here, we demonstrate the power of our approach in the Hi-Myc model of PCa, identifying the disease-responsive peptide substrate S16 from a multiplexed screen and using *in situ* activity profiling with

AZPs, coupled with immunostaining and quantitative analysis, to find that S16 cleavage localized to both tumor cells and Ki-67-positive glands that had not yet progressed to adenocarcinoma. This ability to quantitatively co-localize protease activity signals with other markers may enable concurrent identification of both disease-specific peptide linkers and biological targets for rational design of protease-activated diagnostics and therapeutics. Last, we show that an *in vivo* imaging probe incorporating S16 exhibited enhanced signal in Hi-Myc prostate explants, and future work is warranted to determine whether this probe could enable *in vivo* visualization of early-stage tumorigenesis in this model. Multiplexed screening followed by *in situ* labeling is therefore a powerful approach to enable the rational design of activatable agents for *in vivo* use.

AZPs offer several advantages over existing methods of measuring and localizing protease activity *in situ*. While *in situ* activity profiling with fluorescently-tagged probodies has recently been shown to correlate with *in vivo* therapeutic efficacy, this approach requires target antigen expression for probe binding and is therefore limited in its generalizability *(119)*. AZPs address this limitation in that they provide a modular, antigen-independent means to directly measure substrate-specific protease activity. Activity-based probes, which covalently bind to protease active sites, consist of two components (a recognition sequence and a reactive functional group) that must be redesigned for each new protease target *(92)*. AZPs, in contrast, consist of two constant regions (polyR and polyE, Fig. 4.1b) and a single protease-cleavable linker that can be replaced with any sequence of interest. This modularity enabled us to synthesize a library of 19 AZPs, all of which were dependent on proteolysis for tissue labeling (Fig. 4.S5). Therefore, we expect that AZPs could readily be designed to incorporate any candidate peptide substrate identified in a multiplexed screen, a degree of modularity unmatched by existing *in situ* probes.

This work also establishes AZPs as a molecular tool to probe protease-mediated biological processes *in situ*. Many proteases, including MMPs, are synthesized as zymogens and require proteolytic processing for activation *(89)*. Furthermore, protease activity is dependent on environmental factors like post-translational processing and the abundance of endogenous protease inhibitors *(92)*. Because proteases exert their function through their activity, direct measurements of protease activity rather than abundance may enable new insights into the roles of enzymatic biology in health and disease. For example, though proteases are known to be expressed in the intestine and are critical to intestinal homeostasis, their precise functions have remained poorly understood, in part because of the lack of available tools to measure and localize protease activity *(115)*. The ability of AZPs to label serine protease activity in the colon may enable improved understanding of intestinal physiology and pathology. Furthermore, in this work, we uncovered an increase in metalloproteinase activity in both tumor regions and, unexpectedly, in histologically normal prostatic glands in the Hi-Myc PCa GEMM. This finding was powered by the identification of S16, a metalloproteinase-sensitive peptide cleaved by proteases in the Hi-Myc model, followed by *in situ* labeling with S16-Z. Additional investigation revealed that S16-Z-positive glands and tumor regions were also positive for the proliferation marker Ki-67 and overexpressed MMP12. Quantification of these *in situ* measurements verified robust and significant dysregulation of cell proliferation and metalloproteinase activity in Hi-Myc prostates. Metalloproteinase dysregulation may serve as a marker for early tumorigenesis in the Hi-Myc model and further investigation is warranted to elucidate its biological significance. This novel integration of *in situ* activity profiling, immunostaining, and quantitative image analysis could provide a powerful paradigm to dissect and understand protease biology.

Though the cleavage-based methods presented here offer several advantages over existing methodology, their primary limitation is specificity, as proteases of the same class exhibit substantial cross-cutting against short peptides (Fig. 4.2a). Multiplexed screens followed by *in situ* labeling with AZPs can be readily deployed as a pipeline to discover and validate peptide linkers for conditionally activated diagnostics or therapeutics, which must be selective for cancer relative to healthy tissue but need not be specific to any one protease *(96)*. In contrast, further optimization is needed before such cleavage-based methods can be reliably leveraged as a tool to dissect protease biology with single enzyme resolution. High throughput screens of peptides enriched with unnatural amino acids may yield protease substrates with dramatically improved specificities *(120, 121)*.

In summary, we have established a modular pipeline to discover and validate disease-responsive protease substrates. We present a bottom-up approach to the design of an activatable imaging probe in a PCa GEMM and also show that our methods can be used to directly probe protease activity in human tissue. We expect that our pipeline, which can be readily adapted to any tissue type or set of peptide substrates, will help elucidate the multifaceted roles of proteases in health and disease and accelerate the development of highly specific protease-activated diagnostics and therapeutics.

4.4 Materials and Methods

Peptide synthesis

All peptides were synthesized by CPC Scientific (Sunnyvale, CA) and reconstituted in dimethylformamide (DMF) unless otherwise specified.

Hi-Myc PCa model

All animal studies were approved by the Massachusetts Institute of Technology (MIT) committee on animal care (protocol 0417-025-20). Reporting complied with Animal Research: Reporting In Vivo Experiments (ARRIVE) guidelines. Hi-Myc mice (FVB-Tg(ARR2/Pbsn-MYC)7Key/Nci) were obtained from Jackson Labs. The Hi-Myc model was generated as previously described*(117)*. Age-matched healthy male FVB/NJ mice (Jackson Labs) were used as controls in all experiments.

Mouse dissections and tissue isolation

For prostate tissue, urogenital organs from Hi-Myc mice and age-matched healthy male FVB/NJ mice (Jackson Labs) were isolated, and prostates were microdissected. Adipose tissue surrounding the prostates was removed using forceps, and the entirety of the mouse prostate (ventral, dorsal, lateral, and anterior lobes) was separated from the urethra. For preparation for tissue homogenization, prostates were flash frozen in liquid nitrogen and stored at -80° C until use. For preparation for cryosectioning, prostates were immediately embedded in optimal-cutting-temperature (OCT) compound (Sakura), and frozen using isopentane chilled with dry ice. Colons were harvested from healthy C57BL/6J mice (Jackson Labs), rinsed with PBS to remove feces, filled with undiluted OCT using a blunt 20-gauge needle, embedded in OCT, and frozen using isopentane chilled with dry ice.

Classification of PCa xenografts with fluorogenic peptide substrates

PC3 (ATCC CRL-1435) and 22Rv1 (ATCC CRL-2505) cells were grown in F-12K (ATCC) or RPMI-1640 (ATCC) media, respectively, supplemented with 10% (v/v) FBS (Gibco) and 1% (v/v) penicillin-streptomycin (CellGro). Four- to six-week-old male NCr nude mice (Taconic) were injected bilaterally with 3.5 x 10^6 PCa cells per flank in a 1:1 ratio of OptiMEM (ATCC) and Matrigel (Corning). PC3 and 22Rv1 xenografts were explanted at an average volume of ~200 mm^3, flash frozen in liquid nitrogen, and stored at -80° C until use. Normal mouse prostates from healthy NCr nude mice (Taconic) were also harvested and flash frozen in liquid nitrogen. Immediately

prior to fluorogenic cleavage assay, tumors and prostates were placed in tubes with high-impact zirconium beads (Benchmark Scientific), and phosphate buffered saline (PBS) was added to achieve a concentration of 100 to 600 mg tissue per mL of PBS. Homogenization was performed using a BeadBeater homogenizer (BioSpec). Bradford assay (Bio-Rad) was performed, and all samples were prepared at the same final protein concentration (~1 mg/mL). Fluorogenic substrates (0.33 μM final concentration) were synthesized by CPC Scientific (Sunnyvale, CA) and incubated in 30 μL final volume with tissue homogenate for 20 minutes at 37° C. Proteolytic cleavage of substrates was quantified by increases in fluorescence over time as measured by fluorimeter (Tecan Infinite M200 Pro).

Proteome profiler proteomics analysis of proteases and protease inhibitors

To prepare samples for proteomic analysis, Protease Inhibitor Cocktail (100x, P8340, Sigma Aldrich) including EDTA (100x, Thermo Scientific) and Triton X-100 (1% v/v, Sigma Aldrich) was added to tissue homogenates of PC3 and 22Rv1 xenografts (homogenization method previously described). Protein concentration was measured via Bradford assay (Bio-Rad) and normalized across samples. Protease and protease inhibitor abundance was assayed using Proteome Profiler Human Protease/Protease Inhibitor Array kits (R&D Systems, ARY025) according to manufacturer's instructions. Signal intensity was quantified using ImageJ (NIH).

Synthesis of peptide-functionalized magnetic beads

For synthesis of peptide-functionalized magnetic beads, amine-functionalized magnetic beads (Dynabeads^{TM} M-270 Amine, Invitrogen) were washed and resuspended in PBS prior to coupling, per manufacturer's instructions. For conjugation of peptides to magnetic beads, the beads were first reacted with MAL-PEG(5k)-SVA (Laysan Bio) in PBS at room temperature for 30 minutes with gentle rotation to introduce sulfhydryl-reactive maleimide handles. Cysteine-terminated peptides (CPC Scientific) with mass-encoded barcodes were then reacted in PBS with up to 30%

DMF to the PEG-coated magnetic beads overnight at room temperature with gentle rotation. Following overnight incubation, any remaining sulfhydryl-reactive handles were quenched with L-cysteine (Sigma Aldrich) by reacting for at least 15 minutes at room temperature. Peptide-functionalized magnetic beads were then pooled, washed in bead wash buffer (0.5% (w/v) bovine serum albumin (BSA), 0.01% (v/v) Tween-20 in PBS) according to manufacturer's instructions, buffer exchanged into PBS, and then resuspended into PBS at the original bead concentration provided by the manufacturer. Peptide-functionalized magnetics beads were stored at 4° C until use. Relative substrate concentrations were quantified via LC-MS/MS analysis of stock bead cocktail solution.

LC-MS/MS reporter quantification

LC-MS/MS was performed by Syneos Health (Princeton, NJ) using a Sciex 6500 triple quadrupole mass spectrometer. Samples were treated with ultraviolet irradiation to photocleave the 3-amino-3-(2-nitro-phenyl)propionic acid (ANP) and liberate the barcoded reporter from residual peptide fragments. Samples were extracted by solid-phase extraction and analyzed by multiple reaction monitoring by LC-MS/MS to quantify concentrations of each barcoded mass variant. Analyte quantities were normalized to a spiked-in internal standard, and concentrations were calculated from a standard curve using peak area ratio (PAR) to the internal standard. Initial peptide concentrations were quantified via LC-MS/MS analysis of stock bead solution used in the cleavage reaction.

In vitro recombinant protease cleavage assays

For bead cleavage assays, magnetic beads functionalized with mass-barcoded peptide substrates were synthesized and prepared as described above. Recombinant proteases were purchased from Enzo Life Sciences, R&D Systems, and Haematologic Technologies. Assays for each recombinant protease were conducted in appropriate enzyme buffer according to manufacturer specifications,

with 12.5 nM recombinant enzyme. For each cleavage reaction, 1.2 x 10^8 beads, consisting of an isokinetic mixture of beads carrying unique substrate-reporter pairs and resuspended to a volume of 60 μL in appropriate enzyme buffer, were added to a PCR reaction tube, and 20 μL of recombinant protease was added and mixed with the bead solution to achieve a final enzyme concentration of 12.5 nM in 80 μL reaction volume. Reactions were incubated at 37° C with gentle rotation (to prevent bead settling) for 1 hour. Following incubation and proteolysis, two rounds of magnetic bead pull-down were used to isolate liberated reporters present in the supernatant. Samples were frozen at -80° C until analysis by LC-MS/MS as described above. Initial peptide concentrations were quantified via LC-MS/MS analysis of stock bead solution used in the cleavage reaction. To determine the relative concentrations of cleavage-liberated reporters, liberated reporter PAR values were normalized to stock reporter PAR values.

For fluorescence cleavage assays, intramolecularly quenched peptide substrates (S16-Q, S16-QZ, dS16-QZ) were reacted with recombinant proteases to characterize cleavage kinetics. Substrates were incubated with recombinant MMP12 (Enzo Life Sciences) at a final peptide concentration of 1 μM and a final enzyme concentration of 12.5 nM in a reaction volume of 30 μL in MMP-specific buffer (50 mM Tris, 300 mM NaCl, 10 mM $CaCl_2$, 2 μM $ZnCl_2$, 0.02% (v/v) Brij-35, 1% (w/v) BSA, pH 7.5) at 37° C. Proteolytic cleavage of substrates was quantified by increases in fluorescence over time as measured by fluorimeter (Tecan Infinite M200 Pro).

Bead cleavage assays with tissue homogenates

Prostates from Hi-Myc and age-matched healthy FVB/NJ male mice were harvested and fresh frozen as described above. Prior to fluorogenic cleavage assay, prostates were placed in tubes with high-impact zirconium beads (Benchmark Scientific), and PBS was added to achieve a concentration of 100 to 300 mg tissue per mL of PBS. Homogenization was performed using a BeadBeater homogenizer (BioSpec). Bradford assay (Bio-Rad) was performed, and all samples

were prepared to twice (~2 mg/mL) the desired final assay protein concentration (~1 mg/mL). For inhibited conditions, 1 mM AEBSF (Sigma Aldrich) or 2 mM marimastat (Sigma Aldrich) were pre-incubated with tissue homogenates for at least 30 minutes prior to cleavage assay.

Magnetic beads functionalized with mass-barcoded peptide substrates were synthesized and prepared as described above. For each cleavage reaction, 1.2 x 10^8 beads, comprised of a multiplexed cocktail of beads carrying unique substrate-reporter pairs and resuspended to a volume of 40 μL in PBS, were added to a PCR reaction tube, and 40 μL of tissue sample (2 mg/mL protein concentration) was added and mixed with the bead solution to achieve a final protein concentration of 1 mg/mL in 80 μL reaction volume. Reactions were incubated at 37° C with gentle rotation (to prevent bead settling) for 1 hour. Following incubation and proteolysis, two rounds of magnetic separation were used to isolate liberated reporters. Samples were frozen at -80° C until analysis by LC-MS/MS as described above. To determine the relative concentrations of cleavage-liberated reporters, mean normalization was performed on reporter PAR values to account for tissue-to-tissue differences in substrate and protein concentration.

In situ zymography with AZPs

Organs were extracted and immediately embedded and frozen in optimal-cutting-temperature (OCT) compound (Sakura). Cryosectioning was performed at the Koch Institute Histology Core. Prior to staining, slides were air dried and fixed in ice-cold acetone for 10 minutes. After hydration in PBS (3x5 minutes), tissue sections were blocked in protease assay buffer (S6-Z: 50 mM Tris, 0.01% (v/v) Tween 20, 1% (w/v) BSA, pH 7.4; S2-Z/S10-Z: 50 mM Tris, 150 mM NaCl, 10 mM $CaCl_2$, 0.05% (v/v) Brij-35, 1% (w/v) BSA, pH 7.5; S16-Z: 50 mM Tris, 300 mM NaCl, 10 mM $CaCl_2$, 2 μM $ZnCl_2$, 0.02% (v/v) Brij-35, 1% (w/v) BSA, pH 7.5) for 30 minutes at room temperature. Blocking buffer was aspirated, and solution containing fluorescently labeled AZP (1 μM) and a free poly-arginine control (polyR, 0.1 μM) diluted in the relevant assay buffer was

applied. Slides were incubated in a humidified chamber at 37° C for 4 hours. For inhibited controls, 400 μM AEBSF (Sigma Aldrich) or 1 mM marimastat (Sigma Aldrich) was added to the buffer at both the blocking and cleavage assay steps for S6-Z and S16-Z experiments, respectively. For co-staining experiments, primary antibodies (E-cadherin, AF648, R&D Systems, 20 μg/mL; Ki-67, ab15580, Abcam, 1 μg/mL) were included in the AZP solution. Following AZP incubation, slides were washed in PBS (3x5 minutes), stained with Hoechst (5 μg/mL, Invitrogen) and the appropriate secondary antibody if relevant (Invtirogen), washed in PBS (3x5 minutes), and mounted with ProLong Diamond Antifade Mountant (Invitrogen). Slides were scanned on a Pannoramic 250 Flash III whole slide scanner (3DHistech).

AZP library characterization

AZPs (10 μM final concentration) were incubated with recombinant protease (100 nM final concentration) in 60 μL final volume of appropriate enzyme buffer at 37° C for at least 2 hours to run cleavage reactions to completion. Recombinant proteases were selected on the basis of substrate characterization and cleavage specificity (Fig. 4.2). S1-Z, S3-Z, S7-Z, S14-Z, S15-Z, S16-Z, and S19-Z were incubated with recombinant MMP13 (Enzo Life Sciences); S2-Z, S6-Z, S9-Z, S11-Z, S12-Z, S13-Z, S17-Z, and S20-Z AZPs were incubated with recombinant PRSS3 (R&D Systems); S5-Z, S8-Z, and S18-Z were incubated with recombinant KLK14 (R&D Systems); and S10-Z was incubated with recombinant KLK2 (R&D Systems). Following pre-cleavage with recombinant enzymes, AZP solutions were diluted to a final peptide concentration of 1 μM in appropriate enzyme buffer. Cognate in-tact AZPs (1 μM in appropriate enzyme buffer) and pre-cleaved AZPs were applied to fresh frozen sections of normal mouse colon (slide preparation previously described) and incubated at 37° C for 30 minutes. Following AZP incubation, slides were washed, stained with Hoechst, mounted, and scanned as previously described. The MMP12-responsive probes incorporating the substrate S16, S16-Z and S16-QZ,

were additionally characterized using pre-cleavage by MMP12 (Enzo Life Sciences), followed by application to fresh frozen sections of normal mouse colon and incubation at 4° C for 30 minutes.

AZP analysis of human PCa tissue microarray (TMA)

Fresh frozen human PCa TMAs (BioChain Institute, Inc.; T6235201) were air dried and fixed in ice-cold acetone for 10 minutes. After hydration in PBS (as previously described), tissue sections were blocked in serine protease assay buffer (50 mM Tris, 150 mM NaCl, 10 mM $CaCl_2$, 0.05% (v/v) Brij-35, 1% (w/v) BSA, pH 7.5) for 30 minutes at room temperature. Blocking buffer was aspirated, and solution containing AZP (1 μM) and a free poly-arginine control (polyR, 0.1 μM) diluted in assay buffer was applied. Slides were incubated in a humidified chamber at 37° C for 4 hours. For inhibited controls, protease inhibitor cocktail (P8340, Sigma Aldrich) spiked with 400 μM AEBSF (Sigma Aldrich) and 1 mM marimastat (Sigma Aldrich) was added to the buffer at both the blocking and cleavage assay steps. Following AZP incubation, slides were washed, stained with Hoechst, mounted, and scanned as previously described.

ELISA for MMP12

Tissue levels of MMP12 in Hi-Myc and healthy FVB/NJ prostate homogenates were measured by ELISA according to manufacturer's protocol (ab246540, abcam). Prostate homogenates were prepared as previously described. Protein concentration was measured via Bradford assay (Bio-Rad) and normalized across samples.

Immunofluorescence staining for MMP12

Slides of fresh-frozen tissue sections were prepared as described above. Slides were blocked in serum-based blocking buffer and incubated with primary antibody against MMP12 (MA5024851, Invitrogen, 1:50, 20 μg/mL). Slides were washed in PBS (3x5 minutes), incubated with the appropriate secondary antibody (Invitrogen) and Hoechst (5 μg/mL, Invitrogen), and washed in PBS (3x5 minutes). Slides were mounted and scanned as previously described.

Quantification of AZP staining

AZP staining was quantified in QuPath*(122)* by using cell detection on the DAPI channel with a threshold of 1. For TMA analysis, nuclear AZP staining was calculated as a fold change of the AZP signal over the polyR signal. All nuclei were averaged across the entire tissue section or TMA core. Nuclei with a polyR intensity of less than 3 were excluded from analysis.

Synthesis of activatable probes for in vivo administration

The peptides S16-QZ and uncleavable control dS16-QZ were reconstituted to 1 mg/mL in water. Peptides were then reacted with mPEG-Maleimide, MW 2000 g/mol (Laysan Bio), for PEG coupling via maleimide-thiol chemistry. After completion of the reaction, the final compounds were purified using HPLC. All reactions were monitored using HPLC connected with mass spectrometry (LC/MS). Characterization of final compounds, S16-QZ-(PEG2K) and dS16-QZ-(PEG2K), using HPLC and MALDI-MS indicated that products were obtained with more than 90% purity and at the expected molecular weight.

In vivo administration of activatable probes and imaging of explanted prostate tissues

Male Hi-Myc mice (FVB-Tg(ARR2/Pbsn-MYC)7Key/Nci; 32-36 wks) and age-matched FVB/NJ healthy controls (Jackson Labs; 28-36 wks) were anesthetized using isoflurane inhalation (Zoetis). S16-QZ-(PEG2K) or dS16-QZ-(PEG2K) (4.5 nmoles in 0.9% NaCl) was administered intravenously via tail-vein injection. Four hours after probe injection, mice were euthanized by isoflurane overdose followed by cervical dislocation, and prostates were dissected as previously described. Explanted prostates were imaged on an *in vivo* imaging system (IVIS, PerkinElmer) by exciting Cy5 at 640 nm and measuring emission at 680 nm. Fluorescence signal intensity was quantified using the Living Image software (PerkinElmer).

Statistical analysis

PCA was performed in the R statistical environment (https://www.r-project.org/) using the prcomp function. Hierarchical clustering was performed using GENE-E (Broad Institute; https://software.broadinstitute.org/GENE-E/). All remaining statistical analyses were conducted in GraphPad 7.0 (Prism). All sample sizes and statistical tests are specified in figure legends.

4.5 Acknowledgements

We thank Dr. H. Fleming (MIT) for critical reading and editing of the manuscript; Dr. J. Zhao, Dr. P. Watson, and Dr. C. Sawyers (Memorial Sloan-Kettering) for valuable technical discussion and insight; M. Anahtar, C. Martin-Alonso, and R. Zhao (MIT) for technical assistance; Dr. P. Blainey (MIT and Broad Institute) and Dr. M. Vander Heiden (MIT) for helpful discussion; and K. Cormier and Dr. R. Bronson of the Koch Institute Histology Core (MIT). This study was supported in part by a Koch Institute Support Grant P30-CA14051 from the National Cancer Institute (Swanson Biotechnology Center), a Core Center Grant P30-ES002109 from the National Institute of Environmental Health Sciences, the Ludwig Fund for Cancer Research, Janssen Pharmaceuticals, and the Koch Institute Marble Center for Cancer Nanomedicine. A.P.S. acknowledges support from the NIH Molecular Biophysics Training Grant (NIH/NIGMS T32 GM008313) and the National Science Foundation Graduate Research Fellowship. J.D.K. acknowledges support from the Ludwig Center fellowships. J.S.D acknowledges support from the National Science Foundation Graduate Research Fellowship, the Ludwig Center for Molecular Oncology fellowship, and the Siebel Scholar Foundation. A.B. acknowledges support from the Early Postdoc Fellowship program (P2ELP2_178238) from Swiss National Science Foundation. S.N.B is a Howard Hughes Medical Institute Investigator.

4.6 Author contributions

Jesse D. Kirkpatrick (J.D.K.), Ava P. Soleimany (A.P.S.), Jaideep S. Dudani (J.S.D.), and Sangeeta N. Bhatia (S.N.B.) conceived and designed the research. A.P.S. and J.D.K. performed all experiments and analyzed the data; Susan Su (S.S.) assisted with AZP experiments; Qian Zhong (Q.Z.) performed HPLC purification and assisted with chemical synthesis; Ahmet Bekdemir (A.B.) assisted with bead synthesis and provided technical guidance. A.P.S., J.D.K., and S.N.B. wrote the manuscript with feedback from all authors. J.D.K. and A.P.S. contributed equally.

CHAPTER 5. PERSPECTIVE AND FUTURE DIRECTIONS

5.1 Advances in activity-based diagnostics for disease detection and monitoring

Accurate information about disease state is needed to guide clinical decision making at every stage. Diagnosis of disease is effective if it enables therapeutic intervention that alters the natural history of disease (i.e. reducing the risk of morbidity and mortality). This requires that the information is accurate (e.g. it can distinguish malignant from benign disease) and that it arrives early enough for effective treatment (e.g. surgical resection) to be administered. Once a disease is diagnosed and a treatment administered, effective treatment response monitoring is crucial to ensure that the patient is on the optimal therapy. Here, a rapid readout of disease activity that accurately predicts long-term outcomes is desired.

This thesis sought to validate the hypothesis that protease activity could be harnessed as an effective biomarker for pulmonary disease diagnosis and treatment response monitoring. Along the way, we have made discoveries and developed new technologies that stand to impact the field of activity-based diagnostics. We 1) leveraged direct intrapulmonary delivery to enhance sensitivity and specificity for pulmonary disease, 2) integrated multiplexed activity measurements with machine learning to enable reliable classification of multiple disease states, 3) provided a clear window into the dynamics of drug response, and 4) created new tools to explore the underlying biology of protease dysregulation and enable the rational design of protease-activated diagnostic probes.

Leveraging organ-specific delivery to enhance diagnostic sensitivity and specificity

Lung cancer causes more death than any other cancer *(45)*. Additionally, the lung plays host to a great many deadly diseases of infectious, fibrotic, and genetic etiologies, several of which are

mediated by dysregulated protease activity *(44)*. This thesis therefore aimed to optimize ABNs for detection and monitoring of pulmonary diseases.

Intuitively, one would expect that increasing the accumulation of ABNs at the site of disease and decreasing their exposure to background protease activity in the blood and healthy organs would increase the signal-to-noise ratio, enabling detection of smaller and smaller disease-associated signals. Previous computational modeling work by our group validated this hypothesis mathematically: increasing the delivery of ABNs to the tumor and decreasing their degradation in the blood was predicted to enable detection of 5-mm tumors in humans, a feat that the model found would be unattainable with current intravenous ABN formulations *(52)*. This finding motivated future iterations of the ABN technology, which incorporated integrin-targeted tumor penetrating peptides that enhanced tumor accumulation and enabled detection of locally advanced ovarian tumors totaling 36 mm^3 in mice *(38)*.

We reasoned that direct intrapulmonary delivery would provide a universal strategy for increasing the sensitivity and specificity of ABNs for pulmonary diseases. We first sought to test the hypothesis that intratracheal delivery would increase on-target (i.e. lung) delivery and decrease off-target (i.e. other organ) delivery. Whereas intravenous delivery of a fluorescent ABN variant resulted in only 0.16 times as much fluorescence in the lungs as in all other tested organs (heart, spleen, liver and kidneys) combined, this number was greater than 100 for intratracheally delivered particles, representing a 600-fold biodistribution improvement *(82)*. Accordingly, when we performed intratracheal instillation of our 14-plex sensor cocktail in an autochthonous mouse model of lung cancer, we found that we were able to detect disease when total tumor volume was, on average, just 2.8 mm^3. Organ-specific delivery therefore represents a promising strategy for improving the signal-to-noise ratio of activity-based diagnostics, enabling ultrasensitive disease detection.

Integrating multiplexed signals with machine learning

The power of the ABN platform lies in its ability to measure the activities of multiple disease-associated proteases simultaneously, overcoming the limitations of molecular imaging methods *(21, 33)*. In humans, the heterogeneity of cancer presents fundamental limitations for any single-plex diagnostic, as no single analyte is likely to be shared among all tumors. Furthermore, the multitude of benign diseases that involve protease dysregulation present a great risk of false positives. Multiplexing offers solutions on both fronts. By querying multiple proteases simultaneously, ABNs are better suited to capture the proteolytic diversity of cancer, reducing the risk of missed diagnoses (false negatives). Furthermore, multiplexing offers the opportunity to create disease-specific signatures, or classifiers, that can quantitatively identify subtle differences in the protease profiles of malignant and benign disease, enabling differential diagnosis and reducing the risk of false positives.

In this thesis, we leveraged machine learning to integrate 14-plex urinary ABN outputs into unbiased classifiers that could be prospectively applied. We first showed that we could train a single machine learning classifier to successfully diagnose mice with two distinct molecular subtypes of lung cancer (Fig. 2.6A-C). We then demonstrated that this same classifier could distinguish both mouse models of lung cancer from a mouse model of benign lung inflammation (Fig. 2.6D). These examples highlight the power of combining machine learning and multiplexing to both capture the heterogeneity of lung cancer and reduce the risk of false positives from benign lung disease. Had we attempted to use the ABN PP01, which most strongly differentiated Eml4-Alk mice from healthy controls, as a single plex in the KP model, it would have had no diagnostic power. Similarly, though several individual sensors were unable to distinguish between mice with lung cancer and benign lung inflammation (Fig. 2.S13A-B), our machine learning classifier, which

integrated the signals from all 14 sensors, enabled near-perfect discrimination of malignant and benign disease models (Fig. 2.6D).

Multiplexed ABNs, when combined with machine learning, can be applied to a wide range of classification problems. In this thesis, we also demonstrated that such a paradigm enabled detection of therapeutic response within days after initiation of rapamycin in a mouse model of LAM and alectinib in a mouse model of *Alk*-mutant lung adenocarcinoma. We further expect that this approach may be extensible to other clinically relevant applications, such as the differential diagnosis of bacterial and viral pneumonia, an area of active investigation in our group.

Interrogation of drug response in benign and malignant disease

Effective management of disease requires that response to treatment can be reliably assessed. Accurate and timely information about drug response can guide individual treatment plans, and can also accelerate the pace of the drug development and testing process *(10)*. In this thesis, we demonstrate that multiplexed ABNs can provide unprecedented insight into the dynamics of drug response in both benign and malignant disease. In both LAM and Eml4-Alk driven lung cancer, we found that multiple ABNs tracked with disease progression, and that treatment with small molecule inhibitors rapidly returned the signal from these sensors to baseline. The fact that the same cocktail of 14 sensors enabled response monitoring in two entirely distinct disease models raises the prospect of a single sensor panel that can be generally applied to any pulmonary disease that is characterized by protease dysregulation. Furthermore, the transient, treatment-induced increase in PP04, in both LAM and Eml4-Alk mice, could suggest shared mechanisms of drug response in these two disease models. However, at the time of this work, few methods existed to connect disease-associated biology to *in vivo* ABN cleavage. The final aim of this thesis sought to address this disconnect.

Closing the loop: ex vivo assays reveal biological insights and enable bottom-up design of protease-activated diagnostics

The first two aims of this thesis demonstrated the power of multiplexed ABNs for detection and drug response monitoring of pulmonary diseases. However, we were left with little insight into the biological underpinnings of the differential ABN cleavage observed in different disease states. We therefore sought to develop new tools to query the biology of protease dysregulation in disease. Our multiplexed assay using tissue homogenates allowed us to not only discover a peptide cleaved specifically by cancer-associated proteases, but also to perform inhibition studies that revealed the protease class, metalloproteases, responsible for its cleavage. Our *in situ* assay then led us to the surprising finding that this peptide was cleaved in histologically normal glands, which further investigation revealed to be positive for both MMP12 and Ki67. Finally, we closed the loop by incorporating this peptide into an *in vivo* diagnostic probe that demonstrated significantly enhanced signal in diseased tissue. Future efforts will be directed toward applying this paradigm in reverse, by converting key ABNs like the Eml4-Alk marker PP01 and the treatment response marker PP04 into *in situ* probes in order to query their biological relevance.

5.2 Future Directions

Immunotherapy response monitoring

The emergence of immunotherapy has dramatically altered cancer management. In non-small cell lung cancer, checkpoint blockade with antibodies targeting the PD-1/PD-L1 axis has been shown to improve progression free and overall survival in a wide range of settings, including in patients with treatment-naïve or heavily pre-treated metastatic disease and as a neoadjuvant in patients undergoing resection of local, early-stage tumors *(123)*. However, only a subset of patients exhibits

lasting responses to immunotherapy, and existing biomarkers (e.g. PD-L1 expression on tumor cells) fail to reliably predict which patients will respond. Furthermore, the utility of CT scanning is limited in assessing response to immunotherapy, as patients may present with stable disease or even an apparent increase in tumor burden (likely due to infiltrating immune cells) before eventually responding *(10, 124)*.

The work presented in this thesis provides a framework for developing ABNs for rapid, noninvasive assessment of immunotherapy response. Many elements of the immune response are orchestrated by proteases, including granzyme B and neutrophil elastase, and work from our group and others has demonstrated that measuring such proteases *in vivo* can enable detection of immune-associated processes like graft rejection and response to infection *(39, 125)*. Incorporating ABNs that can detect such proteases into our panel may enable early detection of treatment response in patients undergoing immunotherapy.

High dimensional in situ screening for disease-specific peptide substrates

The activatable zymography probes (AZPs) that we described in Chapter 4 enabled spatial profiling of protease activity in a tissue section. However, this approach relied on fluorescence imaging, which is inherently limited in its multiplexing capacity. Advances in DNA barcoding strategies have enabled the emergence of high dimensional methods to profile gene and protein expression *in situ (126–128)*. Such principles could also be applied to enzyme activity. DNA barcoding could be used to uniquely label hundreds of peptide substrates, which could then be tethered to a slide. Overlaying these slides with healthy or diseased tissue sections could then enable comprehensive mapping of the cleavage patterns of these peptides. Such methods could dramatically accelerate efforts to understand fundamental protease biology and to develop protease-activated diagnostics and therapeutics.

Protease-activated therapeutics

Many promising drug candidates suffer from dose-limiting toxicity. An emerging concept is to leverage disease-specific protease substrates to promote activation of such drugs specifically in the disease microenvironment *(22, 99, 101, 129)*. Such protease-activated therapeutics generally consist of a masking region that can be removed via proteolysis of a peptide linker. By leveraging our *ex vivo* assays, described in Chapter 4, to screen for peptides that are cleaved efficiently in diseased tissue but not in healthy tissues or in the blood, highly selective protease-activated therapeutics can be rationally designed. To realize the full potential of this strategy, it will also be important to design higher throughput substrate screening strategies that are compatible with tissue homogenates and other biospecimens.

5.3 Conclusions

In this work, we demonstrated the potential of activity-based nanosensors for noninvasive detection and treatment response monitoring in pulmonary disease. We further established a suite of assays to enable new insights into protease dysregulation in disease and to inform the rational design of the next generation of protease-activated diagnostics. We hope that these tools will help provide physicians with information to guide clinical decision making and ultimately improve outcomes for patients.

REFERENCES

1. S. H. Miles, Hippocrates and informed consent., *Lancet* **374**, 1322–1323 (2009).

2. J. M. Croswell, D. F. Ransohoff, B. S. Kramer, Principles of Cancer Screening: Lessons From History and Study Design Issues, *Semin. Oncol.* **37**, 202–215 (2010).

3. A. Morabia, F. F. Zhang, History of medical screening: From concepts to action, *Postgrad. Med. J.* **80**, 463–469 (2004).

4. J. R. Prensner, M. A. Rubin, J. T. Wei, A. M. Chinnaiyan, Beyond PSA: the next generation of prostate cancer biomarkers., *Sci. Transl. Med.* **4**, 127rv3 (2012).

5. L. T. Tanoue, N. T. Tanner, M. K. Gould, G. A. Silvestri, Lung cancer screening, *Am. J. Respir. Crit. Care Med.* **191**, 19–33 (2015).

6. National Lung Screening Trial Research Team, D. R. Aberle, A. M. Adams, C. D. Berg, W. C. Black, J. D. Clapp, R. M. Fagerstrom, I. F. Gareen, C. Gatsonis, P. M. Marcus, J. D. Sicks, Reduced lung-cancer mortality with low-dose computed tomographic screening., *N. Engl. J. Med.* **365**, 395–409 (2011).

7. P. B. Bach, J. N. Mirkin, T. K. Oliver, C. G. Azzoli, D. A. Berry, O. W. Brawley, T. Byers, G. A. Colditz, M. K. Gould, J. R. Jett, A. L. Sabichi, R. Smith-Bindman, D. E. Wood, A. Qaseem, F. C. Detterbeck, Benefits and Harms of CT Screening for Lung Cancer, *JAMA* **307**, 2418 (2012).

8. W. C. Black, I. F. Gareen, S. S. Soneji, J. D. Sicks, E. B. Keeler, D. R. Aberle, A. Naeim, T. R. Church, G. A. Silvestri, J. Gorelick, C. Gatsonis, Cost-Effectiveness of CT Screening in the National Lung Screening Trial, *N. Engl. J. Med.* **371**, 1793–1802 (2014).

9. M. Oudkerk, A. Devaraj, R. Vliegenthart, T. Henzler, H. Prosch, C. P. Heussel, G. Bastarrika, N. Sverzellati, M. Mascalchi, S. Delorme, D. R. Baldwin, M. E. Callister, N. Becker, M. A. Heuvelmans, W. Rzyman, M. V. Infante, U. Pastorino, J. H. Pedersen, E. Paci, S. W. Duffy, H. de Koning, J. K. Field, European position statement on lung cancer screening, *Lancet Oncol.* **18**, e754–e766 (2017).

10. J. W. Neal, J. F. Gainor, A. T. Shaw, Developing biomarker-specific end points in lung cancer clinical trials, *Nat. Rev. Clin. Oncol.* **12**, 135–146 (2015).

11. E. P. Henske, F. X. McCormack, Lymphangioleiomyomatosis - A wolf in sheep's clothing, *J. Clin. Invest.* **122**, 3807–3816 (2012).

12. L. R. Young, H. S. Lee, Y. Inoue, J. Moss, L. G. Singer, C. Strange, K. Nakata, A. F. Barker, J. T. Chapman, M. L. Brantly, J. M. Stocks, K. K. Brown, J. P. Lynch, H. J. Goldberg, G. P. Downey, J. J. Swigris, A. M. Taveira-DaSilva, J. P. Krischer, B. C. Trapnell, F. X. McCormack, Serum VEGF-D concentration as a biomarker of lymphangioleiomyomatosis severity and treatment response: A prospective analysis of the Multicenter International

Lymphangioleiomyomatosis Efficacy of Sirolimus (MILES) trial, *Lancet Respir. Med.* **1**, 445–452 (2013).

13. J. C. M. Wan, C. Massie, J. Garcia-Corbacho, F. Mouliere, J. D. Brenton, C. Caldas, S. Pacey, R. Baird, N. Rosenfeld, Liquid biopsies come of age: towards implementation of circulating tumour DNA, *Nat Rev Cancer* **17**, 223–238 (2017).

14. F. Diehl, K. Schmidt, M. A. Choti, K. Romans, S. Goodman, M. Li, K. Thornton, N. Agrawal, L. Sokoll, S. A. Szabo, K. W. Kinzler, B. Vogelstein, L. A. Diaz, Circulating mutant DNA to assess tumor dynamics, *Nat. Med.* **14**, 985–990 (2008).

15. H. J. Nielsen, V. Anagnostou, R. Fijneman, V. E. Velculescu, S. Speir, T. Ørntoft, C. Hruban, J. Phallen, A. Leal, E. Papp, V. Adleff, R. B. Scharpf, H. Husain, S. Cristiano, F. V. Mortensen, J. White, D. Riley, S. Angiuoli, S. Jones, C. Punt, N. van Grieken, C. L. Andersen, M. R. Madsen, M. Nesselbush, A. Georgiadis, J. Huiskens, N. Sengamalay, L. A. Diaz, M. Sausen, G. Meijer, D. Murphy, M.-B. W. Orntoft, S. Parpart-Li, J. Fiksel, Q. K. Li, T. Reinert, B. D. Woodward, Direct detection of early-stage cancers using circulating tumor DNA, *Sci. Transl. Med.* **9**, eaan2415 (2017).

16. J. D. Cohen, L. Li, Y. Wang, C. Thoburn, B. Afsari, L. Danilova, C. Douville, A. A. Javed, F. Wong, A. Mattox, R. H. Hruban, C. L. Wolfgang, M. G. Goggins, M. Dal Molin, T. L. Wang, R. Roden, A. P. Klein, J. Ptak, L. Dobbyn, J. Schaefer, N. Silliman, M. Popoli, J. T. Vogelstein, J. D. Browne, R. E. Schoen, R. E. Brand, J. Tie, P. Gibbs, H. L. Wong, A. S. Mansfield, J. Jen, S. M. Hanash, M. Falconi, P. J. Allen, S. Zhou, C. Bettegowda, L. A. Diaz, C. Tomasetti, K. W. Kinzler, B. Vogelstein, A. M. Lennon, N. Papadopoulos, Detection and localization of surgically resectable cancers with a multi-analyte blood test, *Science (80-.).* **359**, 926–930 (2018).

17. M. C. Liu, G. R. Oxnard, E. A. Klein, C. Swanton, M. V Seiden, Sensitive and specific multi-cancer detection and localization using methylation signatures in cell-free DNA, *Ann. Oncol.* **xxx** (2020), doi:10.1016/j.annonc.2020.02.011.

18. A. M. Lennon, A. M. Lennon, A. H. Buchanan, I. Kinde, A. Warren, A. Honushefsky, Feasibility of blood testing combined with PET-CT to screen for cancer and guide intervention, **9601** (2020).

19. C. Bettegowda, M. Sausen, R. J. Leary, I. Kinde, Y. Wang, N. Agrawal, B. R. Bartlett, H. Wang, B. Luber, R. M. Alani, E. S. Antonarakis, N. S. Azad, A. Bardelli, H. Brem, J. L. Cameron, C. C. Lee, L. A. Fecher, G. L. Gallia, P. Gibbs, D. Le, R. L. Giuntoli, M. Goggins, M. D. Hogarty, M. Holdhoff, S. M. Hong, Y. Jiao, H. H. Juhl, J. J. Kim, G. Siravegna, D. A. Laheru, C. Lauricella, M. Lim, E. J. Lipson, S. K. Marie, G. J. Netto, K. S. Oliner, A. Olivi, L. Olsson, G. J. Riggins, A. Sartore-Bianchi, K. Schmidt, lM Shih, S. M. Oba-Shinjo, S. Siena, D. Theodorescu, J. Tie, T. T. Harkins, S. Veronese, T. L. Wang, J. D. Weingart, C. L. Wolfgang, L. D. Wood, D. Xing, R. H. Hruban, J. Wu, P. J. Allen, C. M. Schmidt, M. A. Choti, V. E. Velculescu, K. W. Kinzler, B. Vogelstein, N. Papadopoulos, L. A. Diaz, Detection of circulating tumor DNA in early- and late-stage human malignancies, *Sci Transl Med* **6**, 224ra24 (2014).

20. I. S. Haque, O. Elemento, Challenges in Using ctDNA to Achieve Early Detection of Cancer, *bioRxiv* , 237578 (2017).

21. A. P. Soleimany, S. N. Bhatia, Activity-Based Diagnostics : An Emerging Paradigm for Disease Detection and Monitoring, *Trends Mol. Med.* , 1–19 (2020).

22. J. S. Dudani, A. D. Warren, S. N. Bhatia, Harnessing Protease Activity to Improve Cancer Care, *Annu. Rev. Cancer Biol.* **2**, 353–376 (2018).

23. V. Hernandez-Gea, S. L. Friedman, Pathogenesis of Liver Fibrosis, *Annu. Rev. Pathol. Mech. Dis.* **6**, 425–456 (2011).

24. R. Weissleder, C. H. Tung, U. Mahmood, a Bogdanov, In vivo imaging of tumors with protease-activated near-infrared fluorescent probes., *Nat. Biotechnol.* **17**, 375–378 (1999).

25. U. Mahmood, R. Weissleder, Near-infrared optical imaging of proteases in cancer, *Mol. Cancer Ther.* **2**, 489–496 (2003).

26. M. J. Whitley, D. M. Cardona, A. L. Lazarides, I. Spasojevic, J. M. Ferrer, J. Cahill, C.-L. Lee, M. Snuderl, D. G. Blazer, E. S. Hwang, R. A. Greenup, P. J. Mosca, J. K. Mito, K. C. Cuneo, N. A. Larrier, E. K. O'Reilly, R. F. Riedel, W. C. Eward, D. B. Strasfeld, D. Fukumura, R. K. Jain, W. D. Lee, L. G. Griffith, M. G. Bawendi, D. G. Kirsch, B. E. Brigman, A mouse-human phase 1 co-clinical trial of a protease-activated fluorescent probe for imaging cancer., *Sci. Transl. Med.* **8**, 320ra4 (2016).

27. T. Jiang, E. S. Olson, Q. T. Nguyen, M. Roy, P. a Jennings, R. Y. Tsien, Tumor imaging by means of proteolytic activation of cell-penetrating peptides., *Proc. Natl. Acad. Sci. U. S. A.* **101**, 17867–72 (2004).

28. E. N. Savariar, C. N. Felsen, N. Nashi, T. Jiang, L. G. Ellies, P. Steinbach, R. Y. Tsien, Q. T. Nguyen, Real-time in Vivo molecular detection of primary tumors and metastases with ratiometric activatable cell-penetrating peptides, *Cancer Res.* **73**, 855–864 (2013).

29. E. S. Olson, T. Jiang, T. a Aguilera, Q. T. Nguyen, L. G. Ellies, M. Scadeng, R. Y. Tsien, Activatable cell penetrating peptides linked to nanoparticles as dual probes for in vivo fluorescence and MR imaging of proteases., *Proc. Natl. Acad. Sci. U. S. A.* **107**, 4311–4316 (2010).

30. Q. T. Nguyen, E. S. Olson, T. A. Aguilera, T. Jiang, M. Scadeng, L. G. Ellies, R. Y. Tsien, Surgery with molecular fluorescence imaging using activatable cell-penetrating peptides decreases residual cancer and improves survival., *Proc. Natl. Acad. Sci. U. S. A.* **107**, 4317–22 (2010).

31. L. E. Sanman, M. Bogyo, Activity-based profiling of proteases., *Annu. Rev. Biochem.* **83**, 249–73 (2014).

32. M. Verdoes, L. E. Edgington, F. A. Scheeren, M. Leyva, G. Blum, K. Weiskopf, M. H. Bachmann, J. A. Ellman, M. Bogyo, A nonpeptidic cathepsin s activity-based probe for noninvasive optical imaging of tumor-associated macrophages, *Chem. Biol.* **19**, 619–628 (2012).

33. M. L. James, S. S. Gambhir, A molecular imaging primer: Modalities, imaging agents, and

applications, *Physiol. Rev.* **92**, 897–965 (2012).

34. G. Hong, A. L. Antaris, H. Dai, Near-infrared fluorophores for biomedical imaging, (2017), doi:10.1038/s41551-016-0010.

35. G. A. Kwong, G. von Maltzahn, G. Murugappan, O. Abudayyeh, S. Mo, I. A. Papayannopoulos, D. Y. Sverdlov, S. B. Liu, A. D. Warren, Y. Popov, D. Schuppan, S. N. Bhatia, Mass-encoded synthetic biomarkers for multiplexed urinary monitoring of disease., *Nat. Biotechnol.* **31**, 63–70 (2013).

36. A. D. Warren, G. a Kwong, D. K. Wood, K. Y. Lin, S. N. Bhatia, Point-of-care diagnostics for noncommunicable diseases using synthetic urinary biomarkers and paper microfluidics., *Proc. Natl. Acad. Sci. U. S. A.* **111**, 3671–6 (2014).

37. A. D. Warren, S. T. Gaylord, K. C. Ngan, M. D. Milutinovic, G. A. Kwong, S. N. Bhatia, D. R. Walt, Disease Detection by Ultrasensitive Quantification of Microdosed Synthetic Urinary Biomarkers, (2014).

38. E. J. Kwon, J. S. Dudani, S. N. Bhatia, Ultrasensitive tumour-penetrating nanosensors of protease activity, *Nat. Biomed. Eng.* **1** (2017), doi:10.1038/s41551-017-0054.

39. C. G. Buss, J. S. Dudani, R. T. K. Akana, H. E. Fleming, S. N. Bhatia, Protease activity sensors noninvasively classify bacterial infections and antibiotic responses, *EBioMedicine* (2018), doi:10.1016/j.ebiom.2018.11.031.

40. C. N. Loynachan, A. P. Soleimany, J. S. Dudani, Y. Lin, A. Najer, A. Bekdemir, Q. Chen, S. N. Bhatia, M. M. Stevens, Renal clearable catalytic gold nanoclusters for in vivo disease monitoring, *Nat. Nanotechnol.* **14**, 883–890 (2019).

41. J. S. Dudani, M. Ibrahim, J. Kirkpatrick, A. D. Warren, S. N. Bhatia, Classification of prostate cancer using a protease activity nanosensor library, *Proc. Natl. Acad. Sci.* **115**, 201805337 (2018).

42. K. Y. Lin, G. a Kwong, A. D. Warren, D. K. Wood, S. N. Bhatia, Nanoparticles That Sense Thrombin Activity As Synthetic Urinary Biomarkers of Thrombosis, *ACS Nano* **7**, 9001–9009 (2013).

43. J. S. Dudani, C. G. Buss, R. T. K. Akana, G. A. Kwong, S. N. Bhatia, Sustained-Release Synthetic Biomarkers for Monitoring Thrombosis and Inflammation Using Point-of-Care Compatible Readouts, *Adv. Funct. Mater.* **26**, 2919–2928 (2016).

44. European Respiratory Society, *The Global Impact of Respiratory Disease- Second Edition* (2017).

45. N. Howlader, A. Noone, M. Krapcho, D. Miller, A. Brest, M. Yu, J. Ruhl, Z. Tatalovich, A. Mariotto, D. Lewis, H. Chen, E. Feuer, K. Cronin, *SEER Cancer Statistics Review, 1975-2016* (Bethesda, MD, 2018; https://seer.cancer.gov/csr/1975_2016/).

46. P. B. Bach, J. N. Mirkin, T. K. Oliver, C. G. Azzoli, D. A. Berry, O. W. Brawley, T. Byers, G. A. Colditz, M. K. Gould, J. R. Jett, A. L. Sabichi, R. Smith-Bindman, D. E. Wood, A. Qaseem, F. C. Detterbeck, Benefits and harms of CT screening for lung cancer: A systematic review, *JAMA - J. Am. Med. Assoc.* **307**, 2418–2429 (2012).

47. R. S. Wiener, D. C. Wiener, M. K. Gould, Risks of Transthoracic Needle Biopsy: How High?, *Clin Pulm Med* **20**, 29–35 (2013).

48. A. M. Newman, S. V Bratman, J. To, J. F. Wynne, N. C. Eclov, L. A. Modlin, C. L. Liu, J. W. Neal, H. A. Wakelee, R. E. Merritt, J. B. Shrager, B. W. Loo, A. A. Alizadeh, M. Diehn, An ultrasensitive method for quantitating circulating tumor DNA with broad patient coverage, *Nat Med* **20**, 548–554 (2014).

49. I. S. Haque, O. Elemento, Challenges in Using ctDNA to Achieve Early Detection of Cancer, *bioRxiv* (2017), doi:10.1101/237578.

50. G. A. Silvestri, A. Vachani, D. Whitney, M. Elashoff, K. Porta Smith, J. S. Ferguson, E. Parsons, N. Mitra, J. Brody, M. E. Lenburg, A. Spira, A Bronchial Genomic Classifier for the Diagnostic Evaluation of Lung Cancer, *N. Engl. J. Med.* **373**, 243–251 (2015).

51. D. Hanahan, R. A. Weinberg, Hallmarks of cancer: The next generation, *Cell* **144**, 646–674 (2011).

52. G. A. Kwong, J. S. Dudani, E. Carrodeguas, E. V Mazumdar, S. M. Zekavat, S. N. Bhatia, Mathematical framework for activity-based cancer biomarkers, *Proc. Natl. Acad. Sci.* **112**, 1–6 (2015).

53. R. S. Herbst, J. V Heymach, S. M. Lippman, Lung cancer., *N. Engl. J. Med.* **359**, 1367–80 (2008).

54. M. DuPage, A. L. Dooley, T. Jacks, Conditional mouse lung cancer models using adenoviral or lentiviral delivery of Cre recombinase, *Nat. Protoc.* **4**, 1064–1072 (2009).

55. C. Chuang, P. G. Greenside, Z. N. Rogers, J. J. Brady, D. Yang, R. K. Ma, D. R. Caswell, S. Chiou, A. F. Winters, B. M. Grüner, G. Ramaswami, A. L. Spencley, K. E. Kopecky, L. C. Sayles, E. A. Sweet-cordero, J. B. Li, A. Kundaje, M. M. Winslow, Molecular definition of a metastatic lung cancer state reveals a targetable CD109 – Janus kinase – Stat axis, *Nat. Med.* **23**, 291–300 10 (2017).

56. A. Sweet-Cordero, S. Mukherjee, A. Subramanian, H. You, J. J. Roix, C. Ladd-Acosta, J. Mesirov, T. R. Golub, T. Jacks, An oncogenic KRAS2 expression signature identified by cross-species gene-expression analysis, *Nat. Genet.* **37**, 48–55 (2005).

57. V. G. Tusher, R. Tibshirani, G. Chu, Significance analysis of microarrays applied to the ionizing radiation response, *Proc Natl Acad Sci U S A* **98**, 5116–5121 (2001).

58. The Cancer Genome Atlas Research Network, Comprehensive molecular profiling of lung adenocarcinoma, *Nature* **511**, 543–550 (2014).

59. M. I. Love, W. Huber, S. Anders, Moderated estimation of fold change and dispersion for RNA-seq data with DESeq2, *Genome Biol* **15**, 550 (2014).

60. V. K. Mootha, C. M. Lindgren, K.-F. Eriksson, A. Subramanian, S. Sihag, J. Lehar, P. Puigserver, E. Carlsson, M. Ridderstråle, E. Laurila, N. Houstis, M. J. Daly, N. Patterson, J. P. Mesirov, T. R. Golub, P. Tamayo, B. Spiegelman, E. S. Lander, J. N. Hirschhorn, D. Altshuler, L. C. Groop, PGC-1α-responsive genes involved in oxidative phosphorylation are coordinately downregulated in human diabetes, *Nat. Genet.* **34**, 267–273 (2003).

61. R. L. Kusko, J. F. Brothers, J. Tedrow, K. Pandit, L. Huleihel, C. Perdomo, G. Liu, B. Juan-Guardela, D. Kass, S. Zhang, M. Lenburg, F. Martinez, J. Quackenbush, F. Sciurba, A. Limper, M. Geraci, I. Yang, D. A. Schwartz, J. Beane, A. Spira, N. Kaminski, Integrated Genomics Reveals Convergent Transcriptomic Networks Underlying Chronic Obstructive Pulmonary Disease and Idiopathic Pulmonary Fibrosis, *Am J Respir Crit Care Med* **194**, 948–960 (2016).

62. T. Ueno, S. Linder, G. Elmberger, Aspartic proteinase napsin is a useful marker for diagnosis of primary lung adenocarcinoma, *Br J Cancer* **88**, 1229–1233 (2003).

63. P. Thomas, R. Khokha, F. A. Shepherd, R. Feld, M. S. Tsao, Differential expression of matrix metalloproteinases and their inhibitors in non-small cell lung cancer, *J. Pathol.* **190**, 150–156 (2000).

64. D. Maddalo, E. Manchado, C. P. Concepcion, C. Bonetti, J. A. Vidigal, Y. C. Han, P. Ogrodowski, A. Crippa, N. Rekhtman, E. De Stanchina, S. W. Lowe, A. Ventura, In vivo engineering of oncogenic chromosomal rearrangements with the CRISPR/Cas9 system, *Nature* **516**, 423–428 (2014).

65. V. Poroyko, F. Meng, A. Meliton, T. Afonyushkin, A. Ulanov, E. Semenyuk, O. Latif, V. Tesic, A. A. Birukova, K. G. Birukov, Alterations of lung microbiota in a mouse model of LPS-induced lung injury, *Am. J. Physiol. Cell. Mol. Physiol.* **309**, L76–L83 (2015).

66. L. Breiman, Random Forests, *Mach. Learn.* **45**, 5–32 (2001).

67. C. T. N. Pham, Neutrophil serine proteases: Specific regulators of inflammation, *Nat. Rev. Immunol.* **6**, 541–550 (2006).

68. S. E. Busch, M. L. Hanke, J. Kargl, H. E. Metz, D. MacPherson, A. M. Houghton, Lung Cancer Subtypes Generate Unique Immune Responses, *J. Immunol.* **197**, 4493–4503 (2016).

69. A. Aalipour, H. Y. Chuang, S. Murty, A. L. D'Souza, S. min Park, G. S. Gulati, C. B. Patel, C. Beinat, F. Simonetta, I. Martinić, G. Gowrishankar, E. R. Robinson, E. Aalipour, Z. Zhian, S. S. Gambhir, Engineered immune cells as highly sensitive cancer diagnostics, *Nat. Biotechnol.* **37**, 531–539 (2019).

70. C. P. Rakhit, R. M. Trigg, J. Le Quesne, M. Kelly, J. A. Shaw, C. Pritchard, L. M. Martins, Early detection of pre-malignant lesions in a KRAS G12D -driven mouse lung cancer model by monitoring circulating free DNA , *Dis. Model. Mech.* **12**, dmm036863 (2019).

71. K. Kersten, K. E. Visser, M. H. Miltenburg, J. Jonkers, Genetically engineered mouse models in oncology research and cancer medicine, *EMBO Mol. Med.* **9**, 137–153 (2017).

72. M. Kuhn, caret: Classification and Regression Training. (2017) (available at https://cran.r-project.org/package=caret).

73. R. C. Team, R: A Language and Environment for Statistical Computing (2017) (available at https://www.r-project.org).

74. M. Reich, T. Liefeld, J. Gould, J. Lerner, P. Tamayo, J. P. Mesirov, GenePattern 2.0, *Nat Genet* **38**, 500–501 (2006).

75. J. Schindelin, I. Arganda-Carreras, E. Frise, V. Kaynig, M. Longair, T. Pietzsch, S. Preibisch, C. Rueden, S. Saalfeld, B. Schmid, J. Y. Tinevez, D. J. White, V. Hartenstein, K. Eliceiri, P. Tomancak, A. Cardona, Fiji: an open-source platform for biological-image analysis, *Nat Methods* **9**, 676–682 (2012).

76. J. J. Bissler, F. X. McCormack, L. R. Young, J. M. Elwing, G. Chuck, J. M. Leonard, V. J. Schmithorst, T. Laor, A. S. Brody, J. Bean, S. Salisbury, D. N. Franz, Sirolimus for Angiomyolipoma in Tuberous Sclerosis Complex or Lymphangioleiomyomatosis, *N. Engl. J. Med.* **358**, 140–151 (2008).

77. F. X. McCormack, Y. Inoue, J. Moss, L. G. Singer, C. Strange, K. Nakata, A. F. Barker, J. T. Chapman, M. L. Brantly, J. M. Stocks, K. K. Brown, J. P. Lynch 3rd, H. J. Goldberg, L. R. Young, B. W. Kinder, G. P. Downey, E. J. Sullivan, T. V Colby, R. T. McKay, M. M. Cohen, L. Korbee, A. M. Taveira-DaSilva, H. S. Lee, J. P. Krischer, B. C. Trapnell, C. National Institutes of Health Rare Lung Diseases, M. T. Group, Efficacy and safety of sirolimus in lymphangioleiomyomatosis, *N Engl J Med* **364**, 1595–1606 (2011).

78. F. X. McCormack, N. Gupta, G. R. Finlay, L. R. Young, A. M. Taveira-Da Silva, C. G. Glasgow, W. K. Steagall, S. R. Johnson, S. A. Sahn, J. H. Ryu, C. Strange, K. Seyama, E. J. Sullivan, R. M. Kotloff, G. P. Downey, J. T. Chapman, M. K. Han, J. M. D'Armiento, Y. Inoue, E. P. Henske, J. J. Bissler, T. V. Colby, B. W. Kinder, K. A. Wikenheiser-Brokamp, K. K. Brown, J. F. Cordier, C. Meyer, V. Cottin, J. L. Brozek, K. Smith, K. C. Wilson, J. Moss, Official American thoracic society/Japanese respiratory society clinical practice guidelines: Lymphangioleiomyomatosis diagnosis and management, *Am. J. Respir. Crit. Care Med.* **194**, 748–761 (2016).

79. S. R. Johnson, J. F. Cordier, R. Lazor, V. Cottin, U. Costabel, S. Harari, M. Reynaud-Gaubert, A. Boehler, M. Brauner, H. Popper, F. Bonetti, C. Kingswood, C. Albera, J. Bissler, D. Bouros, P. Corris, S. Donnelly, C. Durand, J. Egan, J. C. Grutters, U. Hodgson, G. Hollis, M. Korzeniewska-Kosela, J. Kus, J. Lacronique, J. W. Lammers, F. McCormack, A. C. Mendes, J. Moss, A. Naalsund, W. Pohl, E. Radzikowska, C. Robalo-Cordeiro, O. Rouvière, J. Ryu, M. Schiavina, A. E. Tattersfield, W. Travis, P. Tukiainen, T. Urban, D. Valeyre, G. M. Verleden, European Respiratory Society guidelines for the diagnosis and management of lymphangioleiomyomatosis, *Eur. Respir. J.* **35**, 14–26 (2010).

80. A. M. Lamattina, A. Taveira-Dasilva, H. J. Goldberg, S. Bagwe, Y. Cui, I. O. Rosas, J. Moss,

E. P. Henske, S. El-Chemaly, Circulating Biomarkers From the Phase 1 Trial of Sirolimus and Autophagy Inhibition for Patients With Lymphangioleiomyomatosis, *Chest* **154**, 1070–1082 (2018).

81. J. Yao, A. M. Taveira-DaSilva, A. M. Jones, P. Julien-Williams, M. Stylianou, J. Moss, Sustained effects of sirolimus on lung function and cystic lung lesions in lymphangioleiomyomatosis, *Am. J. Respir. Crit. Care Med.* **190**, 1273–1282 (2014).

82. J. D. Kirkpatrick, A. D. Warren, A. P. Soleimany, P. M. K. Westcott, J. C. Voog, C. Martin-Alonso, H. E. Fleming, T. Tammela, T. Jacks, S. N. Bhatia, Urinary detection of lung cancer in mice via noninvasive pulmonary protease profiling, *Sci. Transl. Med* **12**, 262 (2020).

83. X. Li, Y. Pritykin, C. P. Concepcion, Y. Lu, G. La Rocca, M. Zhang, P. J. Cook, Y. W. Au, O. Popow, J. A. Paulo, H. G. Otis, C. Mastroleo, P. Ogrodowski, R. Schreiner, K. M. Haigis, D. Betel, C. S. Leslie, A. Ventura, High-resolution in vivo identification of miRNA targets by Halo-Enhanced Ago2 Pulldown, *bioRxiv* , 820548 (2019).

84. T. Kodama, T. Tsukaguchi, Y. Satoh, M. Yoshida, Y. Watanabe, O. Kondoh, H. Sakamoto, Alectinib shows potent antitumor activity against RET-rearranged non-small cell lung cancer, *Mol. Cancer Ther.* **13**, 2910–2918 (2014).

85. H. Sakamoto, T. Tsukaguchi, S. Hiroshima, T. Kodama, T. Kobayashi, T. A. Fukami, N. Oikawa, T. Tsukuda, N. Ishii, Y. Aoki, CH5424802, a Selective ALK Inhibitor Capable of Blocking the Resistant Gatekeeper Mutant, *Cancer Cell* **19**, 679–690 (2011).

86. V. Gopalakrishnan, J. Yao, W. K. Steagall, N. A. Avila, A. M. Taveira-DaSilva, M. Stylianou, M. Y. Chen, J. Moss, Use of CT Imaging to Quantify Progression and Response to Treatment in Lymphangioleiomyomatosis, *Chest* **155**, 962–971 (2019).

87. A. Dongre, D. Clements, A. J. Fisher, S. R. Johnson, LAM Cell-Fibroblast Interactions Enhance Protease Activity by Extracellular Acidification, *Am. J. Pathol.* **187**, 1750–1762 (2017).

88. E. a. Goncharova, D. a. Goncharov, M. Fehrenbach, I. Khavin, B. Ducka, O. Hino, T. V. Colby, M. J. Merrilees, a. Haczku, S. M. Albelda, V. P. Krymskaya, Prevention of Alveolar Destruction and Airspace Enlargement in a Mouse Model of Pulmonary Lymphangioleiomyomatosis (LAM), *Sci. Transl. Med.* **4**, 154ra134-154ra134 (2012).

89. K. Kessenbrock, V. Plaks, Z. Werb, Matrix Metalloproteinases: Regulators of the Tumor Microenvironment, *Cell* **141**, 52–67 (2010).

90. A. P. Soleimany, S. N. Bhatia, Activity-Based Diagnostics: An Emerging Paradigm for Disease Detection and Monitoring, *Trends Mol. Med.* , 1–19 (2020).

91. R. Weissleder, C.-H. Tung, U. Mahmood, A. Bogdanov, In vivo imaging of tumors with protease-activated near-infrared fluorescent probes, *Nat. Biotechnol.* (1999), doi:10.1038/7933.

92. L. E. Sanman, M. Bogyo, Activity-Based Profiling of Proteases, *Annu. Rev. Biochem.* **83**, 249–273 (2014).

93. G. Blum, G. von Degenfeld, M. J. Merchant, H. M. Blau, M. Bogyo, Noninvasive optical imaging of cysteine protease activity using fluorescently quenched activity-based probes, *Nat. Chem. Biol.* **3**, 668–677 (2007).

94. G. A. Kwong, G. von Maltzahn, G. Murugappan, O. Abudayyeh, S. Mo, I. A. Papayannopoulos, D. Y. Sverdlov, S. B. Liu, A. D. Warren, Y. Popov, D. Schuppan, S. N. Bhatia, Mass-encoded synthetic biomarkers for multiplexed urinary monitoring of disease, *Nat. Biotechnol.* **31** (2012), doi:10.1038/nbt.2464.

95. E. J. Kwon, J. S. Dudani, S. N. Bhatia, Ultrasensitive tumour-penetrating nanosensors of protease activity, *Nat. Biomed. Eng.* **1** (2017), doi:10.1038/s41551-017-0054.

96. L. R. Desnoyers, O. Vasiljeva, J. H. Richardson, A. Yang, E. E. M. Menendez, T. W. Liang, C. Wong, P. H. Bessette, K. Kamath, S. J. Moore, J. G. Sagert, D. R. Hostetter, F. Han, J. Gee, J. Flandez, K. Markham, M. Nguyen, M. Krimm, K. R. Wong, S. Liu, P. S. Daugherty, J. W. West, H. B. Lowman, Tumor-specific activation of an EGFR-targeting probody enhances therapeutic index, *Sci. Transl. Med.* **5** (2013), doi:10.1126/scitranslmed.3006682.

97. K. R. Polu, H. B. Lowman, Probody therapeutics for targeting antibodies to diseased tissue, *Expert Opin. Biol. Ther.* **14**, 1049–1053 (2014).

98. I. J. Chen, C. H. Chuang, Y. C. Hsieh, Y. C. Lu, W. W. Lin, C. C. Huang, T. C. Cheng, Y. A. Cheng, K. W. Cheng, Y. T. Wang, F. M. Chen, T. L. Cheng, S. C. Tzou, Selective antibody activation through protease-activated pro-antibodies that mask binding sites with inhibitory domains, *Sci. Rep.* **7**, 1–12 (2017).

99. V. H. Trang, X. Zhang, R. C. Yumul, W. Zeng, I. J. Stone, S. W. Wo, M. M. Dominguez, J. H. Cochran, J. K. Simmons, M. C. Ryan, R. P. Lyon, P. D. Senter, M. R. Levengood, A coiled-coil masking domain for selective activation of therapeutic antibodies, *Nat. Biotechnol.* **37**, 761–765 (2019).

100. D. Wang, T. Wang, H. Yu, B. Feng, L. Zhou, F. Zhou, B. Hou, H. Zhang, M. Luo, Y. Li, Engineering nanoparticles to locally activate T cells in the tumor microenvironment, *Sci. Immunol.* **4**, eaau6584 (2019).

101. D. G. Millar, R. R. Ramjiawan, K. Kawaguchi, N. Gupta, J. Chen, S. Zhang, T. Nojiri, W. W. Ho, S. Aoki, K. Jung, I. Chen, F. Shi, J. M. Heather, K. Shigeta, L. T. Morton, S. Sepulveda, L. Wan, R. Joseph, E. Minogue, A. Khatri, A. Bardia, L. W. Ellisen, R. B. Corcoran, A. N. Hata, S. I. Pai, R. K. Jain, D. Fukumura, D. G. Duda, M. Cobbold, Antibody-mediated delivery of viral epitopes to tumors harnesses CMV-specific T cells for cancer therapy, *Nat. Biotechnol.* (2020), doi:10.1038/s41587-019-0404-8.

102. N. P. Withana, X. Ma, H. M. Mcguire, M. Verdoes, W. A. Van Der Linden, L. O. Ofori, R. Zhang, H. Li, L. E. Sanman, K. Wei, S. Yao, P. Wu, F. Li, H. Huang, Z. Xu, P. J. Wolters, G. D. Rosen, H. R. Collard, Z. Zhu, Z. Cheng, M. Bogyo, Non-invasive Imaging of Idiopathic Pulmonary Fibrosis Using Cathepsin Protease Probes, (2015), doi:10.1038/srep19755.

103. M. J. Whitley, D. M. Cardona, A. L. Lazarides, I. Spasojevic, J. M. Ferrer, J. Cahill, C. L.

Lee, M. Snuderl, D. G. Blazer, E. S. Hwang, R. A. Greenup, P. J. Mosca, J. K. Mito, K. C. Cuneo, N. A. Larrier, E. K. O'Reilly, R. F. Riedel, W. C. Eward, D. B. Strasfeld, D. Fukumura, R. K. Jain, W. D. Lee, L. G. Griffith, M. G. Bawendi, D. G. Kirsch, B. E. Brigman, A mouse-human phase 1 co-clinical trial of a protease-activated fluorescent probe for imaging cancer, *Sci. Transl. Med.* **8** (2016), doi:10.1126/scitranslmed.aad0293.

104. J. S. Dudani, A. D. Warren, S. N. Bhatia, Harnessing Protease Activity to Improve Cancer Care, *Annu. Rev. Cancer Biol.* **2**, 353–376 (2018).

105. S. K. Lyman, J. Gordon, A. Dupage, P. Pramanik, B. Howng, I. A. Zein, M. B. Winter, I. K. Popova, O. Vasiljeva, J. Jones, K. Wong, V. Singson, J. Richardson, B. Zheng, M. Stroh, L. Carman, V. Huels, K. Autio, V. Boni, D. Cho, J. Garcia-corbacho, I. V. Ruiz, O. Hamid, N. Uboha, E. De Vries, A. El-khoueiry, A. Spira, R. E. Sanborn, F. Thistlethwaite, H. Arkenau, J. Bendell, P. A. Ott, N. Rizvi, M. Will, W. M. Kavanaugh, A. Naing, L. R. Desnoyers, in *Society for Immunotherapy of Cancer 33rd Annual Meeting & Pre-Conference Programs*, (2018).

106. S. Mahrus, J. C. Trinidad, D. T. Barkan, A. Sali, A. L. Burlingame, J. A. Wells, Global sequencing of proteolytic cleavage sites in apoptosis by specific labeling of protein N termini, *Cell* **134**, 866–876 (2008).

107. O. Kleifeld, A. Doucet, U. Auf Dem Keller, A. Prudova, O. Schilling, R. K. Kainthan, A. E. Starr, L. J. Foster, J. N. Kizhakkedathu, C. M. Overall, Isotopic labeling of terminal amines in complex samples identifies protein N-termini and protease cleavage products, *Nat. Biotechnol.* **28**, 281–288 (2010).

108. N. J. Agard, S. Mahrus, J. C. Trinidad, A. Lynn, A. L. Burlingame, J. A. Wells, Global kinetic analysis of proteolysis via quantitative targeted proteomics, *Proc. Natl. Acad. Sci. U. S. A.* **109**, 1913–1918 (2012).

109. J. Villanueva, D. R. Shaffer, J. Philip, C. A. Chaparro, H. Erdjument-Bromage, A. B. Olshen, M. Fleisher, H. Lilja, E. Brogi, J. Boyd, M. Sanchez-Carbayo, E. C. Holland, C. Cordon-Cardo, H. I. Scher, P. Tempst, Differential exoprotease activities confer tumor-specific serum peptidome patterns, *J. Clin. Invest.* **116**, 271–284 (2006).

110. C. H. Chen, M. A. Miller, A. Sarkar, M. T. Beste, K. B. Isaacson, D. A. Lauffenburger, L. G. Griffith, J. Han, Multiplexed protease activity assay for low-volume clinical samples using droplet-based microfluidics and its application to endometriosis, *J. Am. Chem. Soc.* **135**, 1645–1648 (2013).

111. A. J. O'donoghue, A. A. Eroy-Reveles, G. M. Knudsen, J. Ingram, M. Zhou, J. B. Statnekov, A. L. Greninger, D. R. Hostetter, G. Qu, D. A. Maltby, M. O. Anderson, J. L. DeRisi, J. H. McKerrow, A. L. Burlingame, C. S. Craik, Global identification of peptidase specificity by multiplex substrate profiling, *Nat. Methods* **9**, 1095–1100 (2012).

112. S. L. Ivry, J. M. Sharib, D. A. Dominguez, N. Roy, S. E. Hatcher, M. T. Yip-Schneider, C. M. Schmidt, R. E. Brand, W. G. Park, M. Hebrok, G. E. Kim, A. J. O'Donoghue, K. S. Kirkwood, C. S. Craik, Global protease activity profiling provides differential diagnosis of pancreatic cysts, *Clin. Cancer Res.* **23**, 4865–4874 (2017).

113. J. Vandooren, N. Geurts, E. Martens, P. E. Van Den Steen, G. Opdenakker, Zymography methods for visualizing hydrolytic enzymes, *Nat. Methods* **10**, 211–220 (2013).

114. N. P. Withana, M. Garland, M. Verdoes, L. O. Ofori, E. Segal, M. Bogyo, Labeling of active proteases in fresh-frozen tissues by topical application of quenched activity-based probes, *Nat. Protoc.* (2015), doi:10.1038/nprot.2016.004.

115. N. Vergnolle, Protease inhibition as new therapeutic strategy for GI diseases, *Gut* **65**, 1215–1224 (2016).

116. M. Uhlén, L. Fagerberg, B. M. Hallström, C. Lindskog, P. Oksvold, A. Mardinoglu, Å. Sivertsson, C. Kampf, E. Sjöstedt, A. Asplund, I. M. Olsson, K. Edlund, E. Lundberg, S. Navani, C. A. K. Szigyarto, J. Odeberg, D. Djureinovic, J. O. Takanen, S. Hober, T. Alm, P. H. Edqvist, H. Berling, H. Tegel, J. Mulder, J. Rockberg, P. Nilsson, J. M. Schwenk, M. Hamsten, K. Von Feilitzen, M. Forsberg, L. Persson, F. Johansson, M. Zwahlen, G. Von Heijne, J. Nielsen, F. Pontén, Tissue-based map of the human proteome, *Science (80-.).* **347** (2015), doi:10.1126/science.1260419.

117. K. Ellwood-Yen, T. G. Graeber, J. Wongvipat, M. L. Iruela-Arispe, J. Zhang, R. Matusik, G. V. Thomas, C. L. Sawyers, Myc-driven murine prostate cancer shares molecular features with human prostate tumors, *Cancer Cell* **4**, 223–238 (2003).

118. T. Scholzen, J. Gerdes, The Ki-67 protein: From the known and the unknown, *J. Cell. Physiol.* **182**, 311–322 (2000).

119. O. Vasiljeva, E. Menendez, M. Nguyen, C. S. Craik, W. Michael Kavanaugh, Monitoring protease activity in biological tissues using antibody prodrugs as sensing probes, *Sci. Rep.* **10**, 1–10 (2020).

120. P. Kasperkiewicz, M. Poreba, S. J. Snipas, H. Parker, C. C. Winterbourn, G. S. Salvesen, M. Drag, Design of ultrasensitive probes for human neutrophil elastase through hybrid combinatorial substrate library profiling, *Proc. Natl. Acad. Sci. U. S. A.* **111**, 2518–2523 (2014).

121. M. Poreba, G. S. Salvesen, M. Drag, Synthesis of a HyCoSuL peptide substrate library to dissect protease substrate specificity, *Nat. Protoc.* **12**, 2189–2214 (2017).

122. P. Bankhead, M. B. Loughrey, J. A. Fernández, Y. Dombrowski, D. G. McArt, P. D. Dunne, S. McQuaid, R. T. Gray, L. J. Murray, H. G. Coleman, J. A. James, M. Salto-Tellez, P. W. Hamilton, QuPath: Open source software for digital pathology image analysis, *Sci. Rep.* **7**, 1–7 (2017).

123. D. B. Doroshow, M. F. Sanmamed, K. Hastings, K. Politi, D. L. Rimm, L. Chen, I. Melero, K. A. Schalper, R. S. Herbst, Immunotherapy in non-small cell lung cancer: Facts and hopes, *Clin. Cancer Res.* **25**, 4592–4602 (2019).

124. J. D. Wolchok, A. Hoos, S. O'Day, J. S. Weber, O. Hamid, C. Lebbé, M. Maio, M. Binder, O. Bohnsack, G. Nichol, R. Humphrey, F. S. Hodi, Guidelines for the evaluation of immune therapy activity in solid tumors: Immune-related response criteria, *Clin. Cancer Res.* **15**, 7412–

7420 (2009).

125. Q. D. Mac, D. V. Mathews, J. A. Kahla, C. M. Stoffers, O. M. Delmas, B. A. Holt, A. B. Adams, G. A. Kwong, Non-invasive early detection of acute transplant rejection via nanosensors of granzyme B activity, *Nat. Biomed. Eng.* **3**, 281–291 (2019).

126. Y. Goltsev, N. Samusik, J. Kennedy-Darling, G. Vazquez, S. Black, G. P. N. Correspondence, S. Bhate, M. Hale, G. P. Nolan, Deep Profiling of Mouse Splenic Architecture with CODEX Multiplexed Imaging In Brief A DNA barcoding-based imaging technique uses multiplexed tissue antigen staining to enable the characterization of cell types and dynamics in a model of autoimmune diseas, *Cell* **174**, 1–14 (2018).

127. S. G. Rodriques, R. R. Stickels, A. Goeva, C. A. Martin, E. Murray, C. R. Vanderburg, J. Welch, L. M. Chen, F. Chen, E. Z. Macosko, Slide-seq: A scalable technology for measuring genome-wide expression at high spatial resolution, *Science (80-.).* **363**, 1463–1467 (2019).

128. P. L. Ståhl, F. Salmén, S. Vickovic, A. Lundmark, J. F. Navarro, J. Magnusson, S. Giacomello, M. Asp, J. O. Westholm, M. Huss, A. Mollbrink, S. Linnarsson, S. Codeluppi, Å. Borg, F. Pontén, P. I. Costea, P. Sahlén, J. Mulder, O. Bergmann, J. Lundeberg, J. Frisén, et al Stahl, PL, Visualization and analysis of gene expression in tissue sections by spatial transcriptomics, *Science (80-.).* **353**, 78 (2016).

129. L. R. Desnoyers, O. Vasiljeva, J. H. Richardson, A. Yang, E. E. M. Menendez, T. W. Liang, C. Wong, P. H. Bessette, K. Kamath, S. J. Moore, J. G. Sagert, D. R. Hostetter, F. Han, J. Gee, J. Flandez, K. Markham, M. Nguyen, M. Krimm, K. R. Wong, S. Liu, P. S. Daugherty, J. W. West, H. B. Lowman, Tumor-specific activation of an EGFR-targeting probody enhances therapeutic index., *Sci. Transl. Med.* **5**, 207ra144 (2013).